Sensor Fault Detection and Fault-Tolerant Estimation of Vehicle States

by

Reza Zarringhalam

A thesis

presented to the University of Waterloo

in fulfillment of the

thesis requirement for the degree of

Doctor of Philosophy

in

Mechanical and Mechatronics Engineering

Waterloo, Ontario, Canada, 2023

Examining Committee Membership

The following served on the Examining Committee for this thesis. The decision of the Examining Committee is by majority vote.

External Examiner:	Dr. Homayoun Najjaran Professor, Dept. of Mechanical Engineering University of Victoria
Internal-External Member:	Dr. Eihab Abdel-Rahman Professor, Dept. of System Design Engineering University of Waterloo
Internal Member:	Dr. Steven Waslander Professor, Dept. of Mechanical and Mechatronics Engineering University of Waterloo
Internal Member:	Dr. Baris Fidan Professor, Dept. of Mechanical and Mechatronics Engineering University of Waterloo
Supervisor:	Dr. Amir Khajepour Professor, Dept. of Mechanical and Mechatronics Engineering University of Waterloo
Supervisor:	Dr. William Melek Professor, Dept. of Mechanical and Mechatronics Engineering University of Waterloo

Author's Declaration

I hereby declare that I am the sole author of this thesis. This is a true copy of the thesis, including any required final revisions, as accepted by my examiners.

I understand that my thesis may be made electronically available to the public.

Abstract

Manufacturing smarter and more reliable vehicles is a progressing trend in the automotive industry. Many of today's vehicles are equipped with driver assistant, automated driving and advanced stability control systems. These systems rely on measured or estimated information to accomplish their tasks. Evidently, reliability of the sensory measurements and the estimate information is essential for desirable operation of advanced vehicle subsystems.

This thesis proposes a novel methodology to detect vehicle sensor faults, reconstruct the faulty sensory signals and deliver fault-tolerant estimation of vehicle states. The proposed method can detect failures of the longitudinal, lateral and vertical acceleration sensors, roll rate, yaw rate and pitch rate sensors, steering angle sensor, suspension height sensors, and motor torque sensors. The proposed structure can deliver fault-tolerant estimations of the vehicle states including the longitudinal, lateral and vertical tire forces, longitudinal and lateral velocities, roll angle, and pitch angle. Road grade and bank angles are also estimated in this method even in presence of sensor faults.

The unified structure in this thesis is realized by fusion of analytical redundancy relations, fault detection observers and adaptive state estimation algorithms. The proposed method can isolate the faults for vehicle stability and control systems and deliver accurate estimation of vehicle states required by such systems despite sensor failures.

The methods developed in this thesis are validated through experiments and can operate reliably in various driving scenarios.

Acknowledgements

Foremost, I would like to thank my supervisors Prof. Amir Khajepour and Prof. William Malek for their encouragement, guidance, knowledge, patience, and genuine kindness during my research. They will always be my role models.

I also would like to acknowledge the financial support of the Automotive Partnership Canada, Ontario Research Fund and General Motors. Special thanks to Dr. Bakhtiar Litkouhi, Dr. Shih-Ken Chen and GM Research and Development teams for their support and considerations on evaluating the proposed methods.

I am also grateful for supports of my colleagues in the Mechatronic Vehicle Systems laboratory, in particular Kevin Cochran and Jeff Graansma, for their assistance during the experimental verification of this research.

I would also like to express my gratitude to my friends Ayyoub Rezaeian, Saber Fallah and Ehsan Hashemi for their technical assistance and valuable discussions throughout this project.

Most importantly, this work would not have been possible without the love and support of my wife, Dr. Elahe Marandi, and my family to whom this thesis is dedicated.

Dedication

To my brilliant and lovely wife, Elahe, and to my dear mother Shahnaz, my amazing sister and brother, Hanieh and Ehsan, and to my dear father Hamid whose memory will always be with me.

Table of Contents

List of Figures

List of Tables

Chapter 1
Introduction

1.1 Motivation

Reliability of sensory measurements and estimated vehicle states is a paramount objective in automotive applications. Many advanced vehicle systems such as stability controllers, automated driving systems and x-by-wire mechanisms rely on information measured by on-board sensors and estimated vehicle states for their operation. Consequently, there is an increasing demand to ensure reliable operation of such systems even in case of sensor failures.

For vehicle control systems, the following information is usually measured directly by sensors:

- Vehicle accelerations (longitudinal, lateral, and vertical):

These accelerations are typically measured by an inertial measurement unit (IMU) and are required in electronic stability control systems (ESC) [1], adaptive cruise control systems (ACC) [2], autonomous driving systems [3], etc.

- Vehicle angular rates (yaw, roll and pitch rates):

Many commercial vehicles are equipped with a 3-axis IMU that measures the yaw rate. Some higher-end vehicles are equipped with a 6-axis IMU that measures yaw, pitch and roll rates. The angular rates are mainly used in ESC systems [4], rollover prevention systems [5] and active suspension systems [6].

- Steering angle:

Usually, an incremental encoder is used to measure the steering angle. The steering angle measurement is necessary for implementation of steer-by-wire systems [7], active steering stability systems [8], driver assistant systems [9] and autonomous driving systems [10].

- Wheel torques:

Wheel torques are measurable in electric vehicles equipped with independent wheel motors and are directly used in torque vectoring applications [11]. Although these measurements are not available in conventional vehicles, approximate or estimated values of the wheel torques can be obtained by using the engine torque and a model of the transmission system. Wheel torques are increasingly being used in modern traction control and stability systems [12].

- Wheel angular velocities:

Encoders are widely used to measure wheel angular velocities and provide this information to different vehicle control subsystems such as anti-lock braking system (ABS) [13] and traction control systems (TCS) [14]. For electric vehicles, wheel angular velocities are available from both the ABS system and the electric motor resolvers. Detection of wheel angular velocity faults is not studied in this thesis since the redundant sensors are commonly available.

- Suspension heights:

Suspension height sensors are mainly employed in active suspension and roll control systems [15]. Linear transducers are the main type of suspension height sensors in automotive applications [16].

In addition to direct use of the sensory signals by control systems, such signals are essential sources of information for estimating immeasurable or costly to measure vehicle states. The most important examples of such states include:

- Tire forces:

It is important to monitor the longitudinal, lateral and vertical tire forces due to their substantial effects on the vehicle dynamics [17]. Many advanced vehicle stability and control applications require information about the tire forces for their operation [18]. Tire forces can be measured by wheel force/moment sensors [19], but this is not a preferred option for commercial vehicles due to cost and mounting challenges. Therefore, estimation is the method of choice to calculate the magnitude of tire forces [20]. Such estimations rely on the vehicle sensors (e.g. steering angle, accelerations, angular rates, wheel angular velocities, etc.) to calculate the tire forces using linear or nonlinear observers [21].

- Vehicle velocity:

Longitudinal and lateral velocities are used by vehicle control systems and tire models to calculate vehicle and tire slips. These slips are important indicators of vehicle stability/instability [22]. Estimation techniques are the most common means to calculate these velocities and slips [23]. Such methods rely on sensory information, e.g. accelerations, angular rates and steering angle, to estimate the velocities and calculate the longitudinal and lateral slips in the tires [24].

- Vehicle roll and pitch angles:

Vehicle roll and pitch angle are required in advanced control systems due to their effects on the vertical tire forces and sprung mass dynamics [25]. These angles are not usually measured in commercial vehicles. Estimation methods are the main tools to provide the roll and pitch angle information for such control systems [26].

- Road grade and bank angles:

Road grade and bank angles considerably affect the vehicle dynamics. Such disturbances also affect vehicle stability, e.g. in terms of rollover and lateral stability [27]. Accurate measurement of these angles in real-time is not practical since cost-effective sensors to deliver such measurements are not available. Therefore, estimation of these angles is the main practical solution considered by many recent studies [28].

In summary, whether obtained directly through measurements or indirectly through estimations, vehicle dynamic states are required for a wide variety of vehicle stability and control applications. Noticeably, malfunction of the sensors and/or inaccuracy of the estimated states may result in unreliable performance of vehicle systems. Hence, such malfunctions must be properly mitigated if encountered. Installation of redundant sensors may help to achieve a desirable performance even with sensor failures. However, the number and type of sensors for estimation or control purposes are important in the vehicle manufacturing due to unit cost. Therefore, achieving reliable measurements and accurate estimation of states using a minimal vehicle sensor set are among the most important objectives for the automotive suppliers and OEMs.

Any practical fault diagnosis solution for automotive applications should comply with the relevant safety and reliability requirements. In terms of safety, vehicle control systems are usually designed to be robust against certain levels of sensor measurement errors. Sensor anomalies beyond such robustness levels shall be detected with a minimal rate of false negatives (i.e. minimum number of undetected sensor faults during the vehicle operation). In terms of reliability, false positives should also be minimized since incorrect diagnosis of a healthy sensor can impact the availability of vehicle features, cause customer dissatisfaction and impose warranty costs.

1.2 Objectives

The main objective of this thesis is to develop a comprehensive methodology for detection of sensor faults, reconstruction of the faulty sensory signals, and accurate estimation of vehicle dynamic states

despite sensor failures. Figure 1.1 shows how the proposed method in this thesis communicates with a closed loop vehicle control system. The objective of the proposed methodology is to guarantee that the vehicle control systems receive fault-free sensory information and a reliable set of estimated vehicle states, even when a fault occurs.

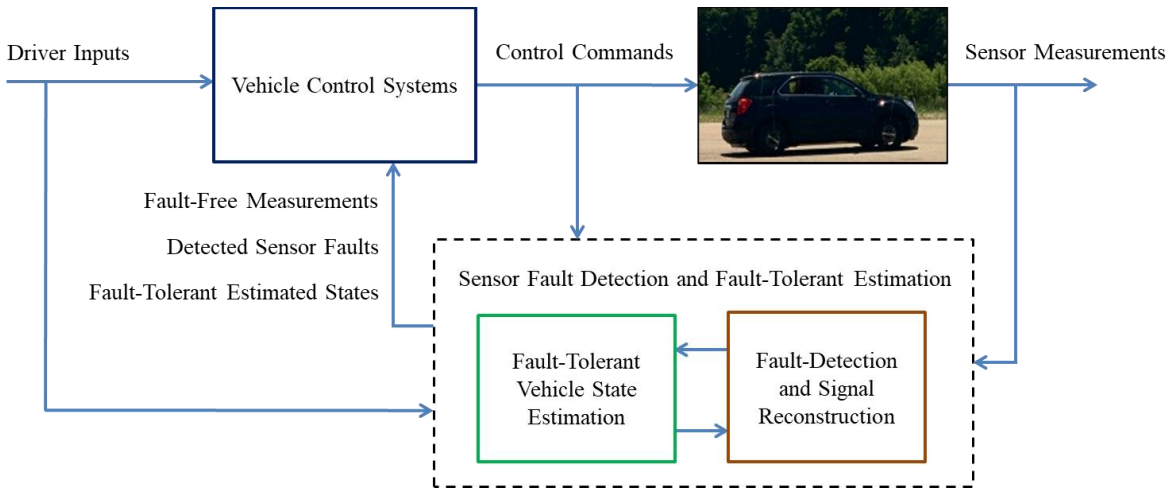

Figure 1.1. A closed-loop vehicle control system including the proposed method

Considering the main goal of this work, the following are detailed objectives of this thesis:

The first objective is to detect failure of sensors that are commonly used in vehicle control systems including steering angle sensor, longitudinal, lateral and vertical acceleration sensors, roll rate, yaw rate and pitch rate sensors, suspension height sensors and motor torque sensors. The fault detection performance needs to be timely (to prevent undesirable operation of vehicle systems), accurate (in terms of correctly detecting and localizing the fault), and reliable (in terms of avoiding false positives).

The second objective of this thesis is to reconstruct the faulty sensory signal when any of the abovementioned sensors fails. The reconstructed signal shall be precise in terms of reporting the actual state of the vehicle even during demanding maneuvers.

The third objective is to deliver the fault-tolerant estimation of vehicle states despite the sensor faults. These states include the longitudinal, lateral, and vertical tire forces, longitudinal and lateral velocities, body roll and pitch angles, and road angles.

Additionally, this thesis intends to accomplish the above objectives using a common sensor set available in commercial vehicles, and does not presume availability of additional information such as

prior knowledge of the road friction coefficient, road grade/bank angles, fault patterns, etc. Therefore, methods developed in this thesis can operate in real-world driving scenarios.

1.3 Thesis Outline

In the second chapter of this thesis, the background of sensor fault detection, fault isolation and fault-tolerant estimation is studied. Various techniques for detection of sensor faults and reconstruction of faulty signals are explored, and the concepts of fault detectability and isolability are discussed. Subsequently, the literature of sensor fault diagnosis is reviewed with emphasis on detection of vehicle sensor faults and fault-tolerant estimation of states for vehicle dynamic control applications.

In the third chapter, a structure is proposed for detection of sensor faults and reconstruction of faulty signals for sensors that are commonly used in rollover prevention and active suspension systems including roll rate, pitch rate and suspension height sensors. This structure combines vehicle's roll dynamics, pitch dynamics, and sprung mass kinematics with unknown input observers and a sensor fault detection module. Kinematic interactions between the road angles and the vehicle states are considered in the proposed method. Next, detectability and isolability of the faults is discussed and an approach for reconstruction of faulty signals is presented. Effectiveness of the proposed method in fault detection and signal reconstruction is demonstrated through experimental results.

Chapter four focuses on detection of sensor faults and reconstruction of faulty signals for sensors that are mainly used in the vehicle handling and stability control systems including the steering angle, yaw rate and acceleration sensors. A structure is presented which generates a set of virtual sensor measurements using vehicle models and estimated vehicle states. The virtual sensors are then compared with the actual sensor measurements in a fault detection module to detect and localize the faults. Reconstruction of the faulty sensory signals is achieved by processing the virtual sensor signals in an observer. Several experiment results are provided to demonstrate effectiveness of the proposed approach in various driving scenarios.

Chapter five presents a unified structure for fault-tolerant estimation of vehicle states including the tire forces and vehicle velocity. First, a set of disturbance observers combined with a fault detection and signal reconstruction module are designed to detect/reconstruct the motor torque sensor faults. This method enables fault-tolerant estimation of longitudinal tire forces. Next, estimation of vertical tire forces is discussed where the load transfer equations combined with the reconstructed acceleration signals and the estimated roll/pitch angles provide the fault-tolerant estimations. For lateral tire forces,

an adaptive unscented Kalman filter is designed in which effects of sensor faults are mitigated by leveraging the reconstructed input signals and adapting the measurement equations. For longitudinal and lateral velocities, fault-tolerance is realized by feeding the reconstructed input signals into kinematic estimators. Next, the unified structure that connects the abovementioned fault detection, signal reconstruction and fault-tolerant estimation modules is discussed, and the comprehensive fault tolerance strategy is summarized. Several experimental case studies are presented at the end to evaluate performance of the proposed method in a variety of driving conditions with different sensor failure scenarios.

Chapter six presents the conclusions and contributions of this thesis and mentions opportunities of future work in this domain.

Chapter 2
Literature Review and Background

This Chapter reviews the literature on sensor fault detection and fault-tolerant estimation of states. Various methods for detection of sensor faults are investigated and concepts of fault detectability and isolability are studied. The recent literature on implementation of these concepts for automotive applications is reviewed, limitations of the prior art is discussed and opportunities to develop more practical and robust solutions in this domain is presented.

2.1 Sensor Fault Detection and Isolation

Fundamentally, all fault detection approaches rely on comparisons between redundant information [29]. Such redundancies are either physical (sensor redundancy) or mathematical. Satellites and aircrafts are normally equipped with multiple redundant sensors to ensure a reliable operation [30]. Even some modern vehicles use redundant sensors for diagnosis purposes. The main issue with the physical redundancy is the associated costs and complexity of packaging redundant sensors in the system. Therefore, mathematical methods for detection and mitigation of faults are the preferred and cost-effective approach for a wide variety of applications.

There are three main steps in developing a fault-tolerant system [31].

- Fault detection: detecting occurrence of faults that result in unreliable behavior of the system.
- Fault isolation: locating the failed sensor in the system.
- Fault management: taking actions to mitigate the undesirable consequences of the faults.

A comprehensive overview of the recent sensor fault detection, isolation and mitigation techniques is available in the trilogy [32], [33], [34] and more recently in [35]. The most common fault detection approaches from the literature are discussed in the next sections.

2.1.1 Analytical Redundancy Relations for Sensor Fault Detection

Analytical redundancies are mathematical compatibility conditions between the inputs (U), sensory measurements (Y), and parameters of the system (P) [36]. These relations are often expressed by a set of constraint equations at each time step (t):

$$\{f(u(t), y(t), p(t)) = 0 \quad | \quad u(t) \in U,\ y(t) \in Y,\ p(t) \in P\} \tag{2-1}$$

Deviations from the constraint model when a fault occurs are called residuals (R):

$$R(t) = f(u(t), y(t), p(t)) \tag{2-2}$$

The residuals are zero or upper-bounded by a certain threshold for normal operational conditions. Therefore, if the analytical redundancy relations are designed properly, residuals of larger magnitudes can indicate the fault in the system.

As an example, analytical redundancy relations are used in [37] to identify the optimal placement of sensors such that all the possible redundancy constraints can be extracted for detecting the faults in a laboratory-scale coupled tank systems.

Speed, simplicity, low computational complexity, and feasibility of real-time implementation are among the key advantages of the analytical redundancy approach [36]. However, such relations cannot be easily identified when the system is highly nonlinear or has high-order and cross-coupled dynamics.

2.1.2 Parity Relations for Sensor Fault Detection

Parity relations approach is a more systematic method to extract the analytical redundancies [38]. In this approach, the residuals are generated as differences between the model and the sensor outputs. Consider a linear-time-invariant (LTI) system such as:

$$\dot{X}(t) = AX(t) + BU(t) + N\mathcal{F}(t) \tag{2-3}$$

$$Y(t) = CX(t) + M\mathcal{F}(t) \tag{2-4}$$

where A is the state matrix, B is the input matrix, C is the output matrix, $\mathcal{F}$ is the fault vector, M is the senor fault matrix and N is the actuator fault matrix. For this system, the redundancy equation can be obtained by taking derivatives of (2-4) up to the order of $q \leq n$ where n indicates order of the system. These derivatives are then combined to create an augmented system [39]:

$$\bar{Y}(t) = \bar{T}X(t) + \bar{G}\bar{U}(t) + \bar{Q}\bar{\mathcal{F}}(t) \tag{2-5}$$

$$\bar{Y}(t) = \begin{bmatrix} Y(t) \\ \dot{Y}(t) \\ \vdots \\ Y^{(q)}(t) \end{bmatrix},\ \bar{U}(t) = \begin{bmatrix} U(t) \\ \dot{U}(t) \\ \vdots \\ U^{(q)}(t) \end{bmatrix},\ \bar{\mathcal{F}}(t) = \begin{bmatrix} \mathcal{F}(t) \\ \dot{\mathcal{F}}(t) \\ \vdots \\ \mathcal{F}^{(q)}(t) \end{bmatrix},\ \bar{T}(t) = \begin{bmatrix} C \\ CA \\ \vdots \\ CA^q \end{bmatrix},$$

$$\bar{G}(t) = \begin{bmatrix} 0 & 0 & 0 & \cdots & 0 \\ CB & 0 & 0 & \cdots & 0 \\ CAB & CB & 0 & \cdots & 0 \\ \vdots & \vdots & & \ddots & 0 \\ CA^{q-1}B & CA^{q-2}B & \dots & CB & 0 \end{bmatrix}, \ \bar{Q}(t) = \begin{bmatrix} M & 0 & 0 & \cdots & 0 \\ CN & M & 0 & \cdots & 0 \\ CAN & CN & M & \cdots & 0 \\ \vdots & \vdots & & \ddots & 0 \\ CA^{q-1}N & CA^{q-2}N & \dots & CN & M \end{bmatrix}$$

To eliminate the unknown state vector $X(t)$, both sides of (2-5) can be multiplied by a vector w^T, where w^T is designed to satisfy the conditions in (2-7):

$$w^T\bar{Y}(t) = w^T\bar{T}X(t) + w^T\bar{G}\bar{U}(t) + w^T\bar{Q}\bar{\mathcal{F}}(t) \tag{2-6}$$

$$w^T\bar{T} = 0 \text{ and } w^T\bar{Q} = 0 \tag{2-7}$$

Subsequently, the residual vector is obtained as a function of the augmented inputs and outputs:

$$R(t) = w^T\bar{Y}(t) - w^T\bar{G}\bar{U}(t) \tag{2-8}$$

Since these residuals indicate the difference between the model and the sensor measurements, a fault can be detected if the residuals exceed a predefined threshold.

More details on the parity approach and processing of the residuals are available in [31]. An accurate knowledge of the model is crucial in this method. The parity approach can be extended to nonlinear systems and can be combined with optimization techniques to generate more robust residuals [40].

2.1.3 Observe-Based Sensor Fault Detection

In the observer-based fault detection approach, occurrence of a fault is detected via comparison of the measured signals and their estimated counterparts provided by an observer [41], [42]. The observed signals are usually constructed using the estimated states and a model of the system [43]. For systems with multiple sensors, the observer-based approach usually requires a bank of observers to cover all potential failures [44].

As an example, a bank of observers is designed in [45] for detection of sensor faults in an autonomous helicopter. The number of observers in the bank is equal to the number of helicopter sensors. Each observer is designed to reconstruct one sensor output. Therefore, a sensor fault can be detected by comparing the estimated and the measured outputs. Despite nonlinearity of the actual helicopter system, linear observers are used due to the limited onboard computing resources. The computational complexity issue for the bank of observers approach is also discussed in [46].

2.1.4 Kalman Filters for Fault Detection and Fault-Tolerant State Estimation

The general idea of using Kalman filters for fault detection was first proposed in [47]. Considering a liner discrete time system with a process noise $w[k]$ and a sensor noise $v[k]$ at each sample time k:

$$X[k+1] = AX[k] + BU[k] + w[k] \tag{2-9}$$

$$Y[k+1] = CX[k] + v[k] \tag{2-10}$$

a Kalman filter can be designed to estimate the state vector $X[k]$ provided that the noise vectors are Gaussian, uncorrelated, and white random signals with zero means. Covariances of these noises also needs to be known a-priori. The difference between the measured outputs Y and the estimated outputs $\hat{Y}$ in the Kalman filter approach is called the innovation vector $\gamma[k]$:

$$\gamma[k] = Y[k] - \hat{Y}[k] = Y[k] - C\hat{x}[k|k-1] \tag{2-11}$$

This innovation vector is expected to have a zero mean and a known covariance when there is no fault. Therefore, detection of faults can be achieved by monitoring statistical properties of the innovation vector. Several extensions of this concept for fault detection are presented in the recent literature [48].

For fault detection in nonlinear systems, the Extended Kalman Filter (EKF) can be employed to handle the nonlinear dynamics. A bank of EKFs is designed in [49] to detect the faults in a marine gas turbine process. In addition to the main EKF which uses a nonlinear model of the system, additional EKFs are designed such that each filter uses a model that represents a specific faulty operational condition. When a fault occurs, the EKF that produces a better matching residual among the bank indicates location of the fault.

The Unscented Kalman Filter (UKF) approach is also widely used for fault detection and fault-tolerant state estimation. In [50], a federated bank of UKFs is developed for fault-tolerant estimation of satellite attitude states. The bank contains a set of local UKFs and a master estimator. Each local UKF estimates the states using a local sensor. The locally estimated states are then fused in the master estimator and a sensitivity factor is defined based on the error covariance matrices of the UKFs. Upon occurrence of a fault, the sensitivity factor exceeds a normal threshold and localizes the fault. The faulty sensor is then excluded from the estimation process and the master estimator relies on the remaining healthy sensors to deliver the fault-free estimations.

An adaptive UKF for attitude estimation of a satellite is proposed in [51]. Theoretical error (i.e., the error between the actual system and the model) and the real error (i.e., the error between the estimated and measured signals) are compared to adaptively reconfigure the estimation structure. When the real error exceeds the theoretical error, the measurement equation is updated to assign a smaller Kalman gain to the failed sensor. Therefore, the estimator relies on the model of the system more than the measurements. Consequently, the sensor fault less severely impacts the estimation results.

More details about the UKF method will be presented in the next chapters of this thesis.

2.2 Common Types of Sensor Faults

Sensor faults may occur due to various reasons including wear and tear, long-term usage, physical changes in the sensor, environmental variations such as temperature changes, miscalibration, issues in the communication channels, etc. When a fault occurs, the output signal from the sensor may exhibit a specific pattern. The most common types of these fault patterns can be categorized as follows [52]:

- Bias: a constant offset from the nominal state that the sensor is measuring.
- Drift: a time varying offset from the nominal state. Such drifts can be linear or nonlinear.
- Scaling (or gain fault): an output from the sensor which a scaled factor of the nominal state. The scaling factor may be constant or time varying.
- Stuck-output: a constant output from the sensor where the reported measurement is stuck at a certain value.
- Excessive noise: a random time series output from the sensor in which the noise magnitude is considerably larger than the noise level during normal operation of the sensor.
- Intermittency: deviations from the nominal state, where the deviation intermittently appears and disappears.
- Loss of signal: a loss of communication between the receiving module and the sensor. Most commonly, a loss of signal results in receiving a constant zero signal from the sensor.

Some studies in the literature propose methods to detect specific subsets of these fault types. In such studies, the fault pattern is assumed to be known a-priori. Evidently, designing more comprehensive

fault-tolerant systems which ensure detectability and isolability of all the above failures without such restrictions is a preferred solution [53].

2.3 Fault Detectability and Isolability

In all of the aforementioned fault detection methods, a major objective is to design the algorithm such that ideally all faults can be detected and their location in the system can be identified. Such objectives are investigated under the topic of fault detectability and isolability.

Fault detectability focuses on making a binary decision on the absence of all faults ($\mathcal{F}(t) = 0$) or presence of any fault in the system ($\mathcal{F}(t) \neq 0$). For a linear system such as the one described by (2-3)-(2-4), it can be shown that all faults $f_i(t) \in \mathcal{F}(t)$ are detectable if and only if:

$$C(sI - A)^{-1}N_i + M_i \neq 0 \tag{2-12}$$

where N_i and M_i are the i-th column of matrices N and M, respectively [54]. If (2-12) holds, then a set of residuals $R(t)$ can be designed to detect presence of a fault in the system. Such residuals can be constructed using any of the fault detection methods introduced in the previous sections.

For nonlinear systems, a generic measure of detectability is not available except for certain classes [55]. Detectability for such systems is usually analyzed by creating a set of residuals and investigating whether the residuals can generate sufficient indications to detect the faults. In other words, given a set of residuals $R(t)$ in a nonlinear system, the fault vector $\mathcal{F}(t)$ is detectable if and only if there exists a non-zero residual $r_i(t) \in R(t)$ when a fault $f_i(t) \in \mathcal{F}(t)$ is non-zero.

Fault isolability is a stronger condition than fault detectability. The objective in fault isolation is to identify the location of each fault in the system. For the linear system described by (2-3)-(2-4), all faults $f_i(t) \in \mathcal{F}(t)$, $i = 1, \dots, l$ are isolable if and only if

$$rank[C(sI - A)^{-1}N_1 + M_1 \ \dots \ C(sI - A)^{-1}N_l + M_l] = l \tag{2-13}$$

where l is the number of faults in the fault vector $\mathcal{F}(t)$ [54]. In other words, for the faults to be isolable, the transfer function between each fault and outputs of the system needs to be unique.

Similar to detectability, a generic fault isolability metric is not available for nonlinear systems. To investigate isolability in such systems, usually several subsets of the residual vector are grouped together and are called fault signatures S, where $S \subset R(t)$. If two distinct signatures S_i and S_j can be

constructed for faults i and j, then the two faults can be distinguished from each other. For complete fault isolability, distinct signatures need to be identified for all the faults in the system, if possible.

2.4 Sensor Fault Detection in Automotive Applications

Fault detection and mitigation strategies for automotive applications have been increasingly investigated in the literature. Many studies have focused on detection of faults in specific vehicle subsystems:

- Steering system sensors [56][57][58][59]
- Suspension system sensors [60][61][62]
- Drivetrain sensors [63][64][65]
- Braking system sensors [66][67][68]

The main drawback in subsystem-based sensor fault detection is the associated complexity. Real-time fault detection using separate modules for each vehicle subsystem also poses challenges in terms of synchronization and a coordinated system-level response to failures. A few of more generic approaches available in the literature are discussed in this section.

Fault-tolerant control of an electric vehicle subject to the steering angle sensor faults is presented in [69]. A model-based estimation of the steering angle is obtained using a planar vehicle dynamics model with linear tires combined with a model of the steering actuator. Measurements of the yaw rate, lateral acceleration and the steering motor current are fed to an EKF to estimate the front steering angle and generate the residuals.

Fault detection for sensors used in lateral and vertical dynamic control systems is discussed in [70]. Analytical redundancy relations are derived in this paper by modeling the kinematic relations between the measured variables. Comparison of these redundancies and the measured signals generates the residuals, and a fuzzy decision-making system is proposed for diagnosis of the faults. This paper separates the lateral and vertical dynamics of the vehicle.

Observer-based diagnosis of the roll rate sensor is investigated in [71]. A linear observer estimates the roll rate of the vehicle using a bicycle model, roll dynamics, and acceleration measurements. This approach requires some assumptions such as a small rate of change for the road bank profile. Moreover, to overcome the drawbacks caused by the simplified kinematic model, this approach only operates

when certain model validity conditions are satisfied and therefore cannot continuously monitor the roll rate sensor.

Roll rate fault detection for heavy vehicles with active anti-roll-bars and active suspensions is discussed in [72] and [73]. In these papers, kinematic relations between the roll state, lateral acceleration, yaw state, and anti-roll-bar moments are employed to design multiple observers for monitoring the roll rate sensor. The dynamic interaction between the lateral acceleration and the roll angle is modeled as a simple lag filter and effects of road bank and grade angles are assumed negligible.

Detection of height sensor faults for an electric air suspension system is investigated in [74]. Roll and pitch dynamics are combined with the kinematics of the sprung mass to detect the sensor faults. However, effects of road grade and bank angle are neglected in this paper and a fixed fault threshold is used which may cause false positives. A similar approach is employed in [15] to design a fault-tolerant controller for a suspension system. Roll and pitch angles are assumed to be small in this study.

An example of a more general solution, detection of sensor and actuator faults in a scaled autonomous electric vehicle is investigated in the series [75], [76], [77]. A sliding mode bank of observers together with model-based analytical redundancies and parity relations are designed in these papers to detect the sensor faults. The experimental results demonstrate successful detection of faults in wheel encoders, GPS position and velocity sensors. However, the steering wheel angle is assumed to be small and suspension dynamics is neglected in these papers. Moreover, accurate GPS position and velocity measurements are essential in this approach, while such data is often not available in commercial vehicles.

Another more complete layout to detect vehicle sensor faults using a residual generator together with a residual processor is presented in [78]. To improve the fault detection performance, history of the residuals and the known fault patterns are embedded in the residual processor unit. Therefore, a fault can be more accurately detected if it matches a known fault pattern. This approach is implemented on a test vehicle and its performance is verified through experiments. Fault patterns should be known a-priori in this approach.

2.5 Fault-Tolerant Estimation of Vehicle States

There are several studies in the literature that focus on estimation of vehicle states, e.g. tire forces [19], [21], and vehicle velocity [23], [24]. The general approach in such studies is to design an estimation

algorithm which uses the sensory information to estimate the states [79]. Many of these structures are designed to be robust against modeling disturbances and measurement noises [80]. However, sensor faults can dramatically affect the performance of such systems. There are a few papers in the literature that investigate this issue for automotive applications.

A model-based fault-tolerant roll angle estimation structure for a roll stability control system is presented in [5]. This approach considers fusion of an eigenstructure assignment technique with a set of analytical redundancy relations. A steady-state estimator for the vehicle roll angle provides the benchmark to detect the fault and reconstruct the roll rate sensor data. To reduce the effects of the consequent inaccuracies in transient conditions, a dynamic factor based on the understeer coefficient is incorporated into the design. This approach is limited to certain operational regions and switching between the steady-state and transient conditions might cause practical problems associated with stability.

Robust estimation of the sideslip angle subject to a lateral acceleration sensor bias is presented in [81]. A hybrid model is developed which combines vehicle kinematics, dynamics, and road bank angle disturbances. The hybrid model is then used in an adaptive EKF which relies on the kinematic model augmented with the road bank model. The EKF can deliver real time estimations of the tire cornering stiffnesses and overcome the lateral acceleration bias.

Effects of partial loss of sensor data on the estimation of vehicle longitudinal velocity and sideslip angle are investigated in [82]. An adaptive fault-tolerant EKF estimator is designed to comprehend the randomness of data loss intervals. The estimator uses a fading factor to improve the state and parameter evolutions and reduce the influence of the sensor loss on the estimated states.

A more general approach for fault-tolerant estimation of lateral velocity, road grade and road bank angle is presented in [83]. This study considers failures of lateral acceleration, yaw rate and steering angle sensors. It is assumed that the vehicle is equipped with different stability control subsystems such as active front steering (AFS), vehicle dynamic control (VDC) and roll stability systems (ROS), each equipped with their dedicated set of sensors. Consequently, independent and redundant lateral acceleration and yaw rate sensors are assumed available. With these assumptions, a general guideline for using these sensors to manage the faults is presented.

There are other similar studies in the literature that consider reconstruction of sensor faults for estimation of certain vehicle states [84][85]. Although combining some of these approaches may help

to estimate a larger subset of the required vehicle states, such a combination will not be efficient in terms of computational complexity. Moreover, many of the available approaches rely on redundant [83] or uncommon [86] sensors that may not be available in commercial vehicles.

2.6 Summary

This chapter reviewed the recent literature on sensor fault detection, fault isolation and fault-tolerant estimation techniques. A review of the relevant literature focusing on automotive applications of these methods was also presented.

Many of the available studies in the literature developed separate modules for detection of certain vehicle sensor faults. Considering the number of sensors used by vehicle control systems, this approach is inefficient in terms of computational complexity, synchronization challenges and a system-level response to failures.

Some of the available fault detection studies in the literature are sensitive to changes in vehicle dynamic conditions such as wheel slips. Many of these methods use predefined fixed criteria to detect sensor faults and are therefore prone to false positives which negatively impacts their reliability when the operational conditions change.

Using redundant or uncommon sensors that are not available in commercial vehicles is another drawback that prevents practical application of some of the available approaches.

Although several studies have focused on fault-tolerant estimation and control systems, to the best of the authors' knowledge, fault-tolerant estimation of tire forces has not yet been discussed in the literature.

To address the above issues, this thesis proposes a unified fault-tolerant estimation method that can deliver three main functionalities:

- Reliable detection of sensor faults
- Accurate isolation and reconstruction of faulty sensory signals
- Precise estimation of vehicle states despite the sensor failures

This structure is realized through fusion of unknown input observers, disturbance observers, adaptive estimation structures, analytical redundancy relations and a set of fault detection and signal reconstruction modules.

The approach in this thesis is a more comprehensive solution compared to the available literature in terms of covering a wider range of vehicle sensors and vehicle dynamic states. Additionally, the proposed method uses a sensor set that is commonly available in commercial vehicles and does not presume availability of additional information such as prior knowledge of the road friction coefficient, road grade/bank angles, fault patterns, etc.

Effectiveness of the proposed approach is verified through experimental case studies. The experiments are performed in a variety of driving maneuvers, road conditions and sensor failure scenarios.

The proposed approach and the experiment results are presented in the next three chapters of this thesis.

Chapter 3

Fault Detection and Signal Reconstruction for Roll Rate, Pitch Rate and Suspension Height Sensors

This chapter presents a novel structure to detect and mitigate failures of the roll rate, pitch rate and suspension height sensors. This structure combines the vehicle roll dynamics, pitch dynamics, sprung mass kinematics, unknown input observers, and a sensor fault detection and signal reconstruction module. The result is a structure that can estimate the states and reconstruct the faulty signals. Unknown road bank and road grade angles, which are not practically measurable using conventional vehicle sensors, are also estimated in this approach. Detectability and isolability of the sensor faults using this structure is analytically verified in this chapter. Effectiveness of the proposed method in detection of faults and reconstruction of faulty signals is demonstrated through several vehicle road tests.

3.1 Introduction

General structure of the proposed method is illustrated in Figure 3.1.

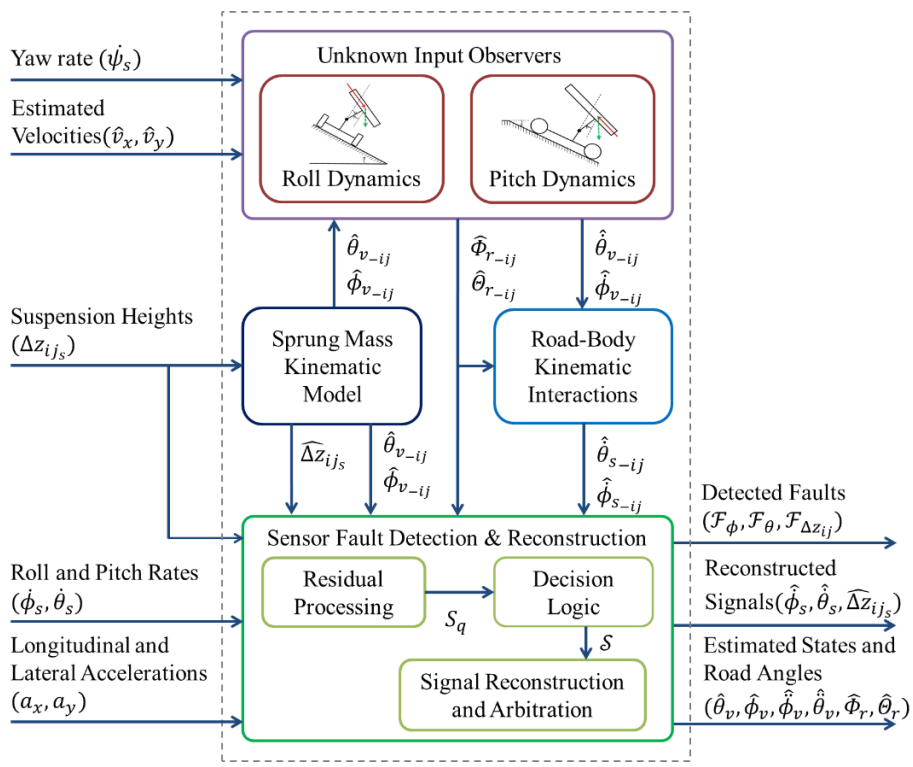

Figure 3.1. Structure of the proposed fault detection and signal reconstruction method

In this structure, analytical redundancy relations and unknown input observers are designed to estimate the variables that are supposed to be measured by the vehicle sensors. Comparing these estimations with values reported by the roll rate, pitch rate and suspension height sensors is the main idea in cross-checking the sensors' health and detecting the faults. When there is no fault in the system, the estimated outputs and actual sensors should deliver similar measurements assuming that the models, analytical redundancy relations and the observers are sufficiently accurate. Therefore, the differences between the estimated outputs and the sensor measurements fall below certain thresholds. The residual processor monitors these differences and reports a fault state to the decision logic if any residual exceeds its threshold. The decision logic monitors the fault states and detects/isolates the fault using the residual patterns. If a sensor fault is detected, the signal reconstruction module reconstructs the faulty signal using the observer estimations, arbitrates between the faulty and reconstructed signals, and delivers the fault-tolerant signals to the other vehicle systems. Dynamic interactions between the road angles and vehicle states are also considered in this approach. A detailed description of the proposed method is discussed in the next sections.

3.2 Analytical Redundancy Relations for Suspension Height Sensors

A schematic of the sprung mass kinematics is illustrated in Figure 3.2 [87]. This model helps to estimate the suspension height at each corner (Δz_{ij}) using the measurements from the sensors installed on the other three corners. Roll angle (ϕ_v) and pitch angle (θ_v) of the vehicle body relative to the vehicle frame are also estimated using suspension height sensors at each corner. These multiple estimations will be used in the following sections to extract the analytical redundancy relations and detect/reconstruct the sensor faults.

The frame coordinate system (x_F, y_F, z_F) is attached to the vehicle frame. Sensor position vectors (ρ_{ij}) in this frame are described by:

$$\rho_{fl} = [L_f \quad d/2 \quad \Delta z_{fl}]^T \tag{3-1}$$

$$\rho_{fr} = [L_f \quad -d/2 \quad \Delta z_{fr}]^T \tag{3-2}$$

$$\rho_{rl} = [-L_r \quad d/2 \quad \Delta z_{rl}]^T \tag{3-3}$$

$$\rho_{rr} = [-L_r \quad -d/2 \quad \Delta z_{rr}]^T \tag{3-4}$$

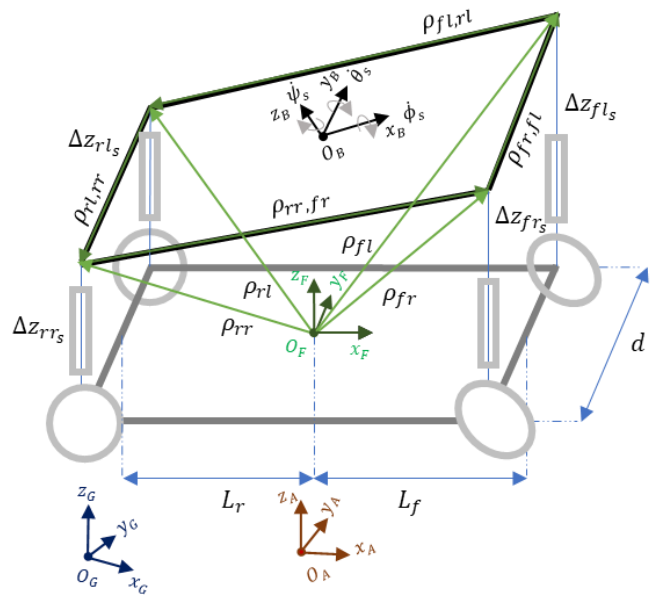

Figure 3.2. Suspension kinematics and sensor locations

where L_f and L_r are the longitudinal distances between the origin O_F and the front and rear axles, respectively, and d is the track width. The subscript $ij \in \{fl, fr, rll, rr\}$ indicates the front-left (fl), front-right (fr), rear-left (rl) and rear-right (rr) corners.

Relative position between any two corners ij and mn is denoted by the vector $\rho_{ij,mn}$:

$$\rho_{ij,mn} = \rho_{mn} - \rho_{ij} \qquad ij, mn \in \{fl, fr, rll, rr\} \tag{3-5}$$

The cross product of two non-parallel relative position vectors yields the normal vector of the body plane $(\mathcal{N})$:

$$\mathcal{N} = \rho_{ij,mn} \times \rho_{ij,pq} \qquad \forall\, ij, mn, pq \in \{fl, fr, rl, rr\} \tag{3-6}$$

Therefore, by using any three suspension height sensor data, the corresponding normal vectors can be written as:

$$\mathcal{N}_{-fl} = \rho_{rl,rr} \times \rho_{rr,fr} \tag{3-7}$$

$$\mathcal{N}_{-fr} = \rho_{fl,rl} \times \rho_{rl,rr} \tag{3-8}$$

$$\mathcal{N}_{-rl} = \rho_{rr,fr} \times \rho_{fr,fl} \tag{3-9}$$

$$\mathcal{N}_{-rr} = \rho_{fl,rl} \times \rho_{fl,fr} \tag{3-10}$$

where the subscript $-ij$ represents the case in which the suspension height from the corner ij is not used in calculation of the normal vector. Subsequently, components $\mathcal{N}_{ij}^{x}, \mathcal{N}_{ij}^{y}, \mathcal{N}_{ij}^{z}$ of the normal vectors (3-7)-(3-10) and sensor position vector components $\rho_{ij}^{x}, \rho_{ij}^{y}, \rho_{ij}^{z}$ in (3-1)-(3-4) are used to estimate the suspension heights ($\widehat{\Delta z}_{ij_s}$) for each corner using the sensors installed at the other three corners:

$$\widehat{\Delta z}_{fl_s} = -\left(\mathcal{N}_{-fl}^{x}\,\rho_{fl}^{x} + \mathcal{N}_{-fl}^{y}\rho_{fl}^{y} + \mathcal{M}_{-fl}\right)/\mathcal{N}_{-fl}^{z} \tag{3-11}$$

$$\widehat{\Delta z}_{fr_s} = -\left(\mathcal{N}_{-fr}^{x}\,\rho_{fr}^{x} + \mathcal{N}_{-fr}^{y}\rho_{fr}^{y} + \mathcal{M}_{-fr}\right)/\mathcal{N}_{-fr}^{z} \tag{3-12}$$

$$\widehat{\Delta z}_{rl_s} = -\left(\mathcal{N}_{-rl}^{x}\,\rho_{rl}^{x} + \mathcal{N}_{-rl}^{y}\rho_{rl}^{y} + \mathcal{M}_{-rl}\right)/\mathcal{N}_{-rl}^{z} \tag{3-13}$$

$$\widehat{\Delta z}_{rr_s} = -\left(\mathcal{N}_{-rr}^{x}\,\rho_{rr}^{x} + \mathcal{N}_{-rr}^{y}\rho_{rr}^{y} + \mathcal{M}_{-rr}\right)/\mathcal{N}_{-rr}^{z} \tag{3-14}$$

where the terms $\mathcal{M}_{-ij}$ are calculated as:

$$\mathcal{M}_{-fl} = -\mathcal{N}_{-fl}^{x}\rho_{fr}^{x} - \mathcal{N}_{-fl}^{y}\rho_{fr}^{y} - \mathcal{N}_{-fl}^{z}\rho_{fr}^{z} \tag{3-15}$$

$$\mathcal{M}_{-fr} = -\mathcal{N}_{-fr}^{x}\rho_{rl}^{x} - \mathcal{N}_{-fr}^{y}\rho_{rl}^{y} - \mathcal{N}_{-fr}^{z}\rho_{rl}^{z} \tag{3-16}$$

$$\mathcal{M}_{-rl} = -\mathcal{N}_{-rl}^{x}\rho_{rr}^{x} - \mathcal{N}_{-rl}^{y}\rho_{rr}^{y} - \mathcal{N}_{-rl}^{z}\rho_{rr}^{z} \tag{3-17}$$

$$\mathcal{M}_{-rr} = -\mathcal{N}_{-rr}^{x}\rho_{fl}^{x} - \mathcal{N}_{-rr}^{y}\rho_{fl}^{y} - \mathcal{N}_{-rr}^{z}\rho_{fl}^{z} \tag{3-18}$$

The four estimated suspension heights ($\widehat{\Delta z}_{ij_s}$) can be used as analytical redundancy relations.

Body roll angle $\hat{\theta}_{v_{-ij}}$ and pitch angle $\hat{\phi}_{v_{-ij}}$, in the scenario that the suspension height sensor ij is not used, can be calculated by projecting the corresponding body normal vector ($\mathcal{N}_{-ij}$) on the frame plane. Consequently, four analytical redundancy relations can be obtained for the body roll angle:

$$\hat{\phi}_{v_{-fl}} = cos^{-1}\frac{\mathcal{N}_{-fl}^{y}}{\|\mathcal{N}_{-fl}\|} \tag{3-19}$$

$$\hat{\phi}_{v_{-fr}} = cos^{-1}\frac{\mathcal{N}_{-fr}^{y}}{\|\mathcal{N}_{-fr}\|} \tag{3-20}$$

$$\hat{\phi}_{v_{-rl}} = cos^{-1}\frac{\mathcal{N}_{-rl}^{y}}{\|\mathcal{N}_{-rr}\|} \tag{3-21}$$

$$\hat{\phi}_{v_{-rr}} = cos^{-1}\frac{\mathcal{N}_{-rr}^{y}}{\|\mathcal{N}_{-rr}\|} \tag{3-22}$$

Similarly, four analytical redundancy relations are obtained for the pitch angle:

$$\hat{\theta}_{v-fl} = cos^{-1}\frac{\mathcal{N}^{x}_{-fl}}{\|\mathcal{N}_{-fl}\|} \tag{3-23}$$

$$\hat{\theta}_{v-fr} = cos^{-1}\frac{\mathcal{N}^{x}_{-fr}}{\|\mathcal{N}_{-fr}\|} \tag{3-24}$$

$$\hat{\theta}_{v-rl} = cos^{-1}\frac{\mathcal{N}^{x}_{-rl}}{\|\mathcal{N}_{-rl}\|} \tag{3-25}$$

$$\hat{\theta}_{v-rr} = cos^{-1}\frac{\mathcal{N}^{x}_{-rr}}{\|\mathcal{N}_{-rr}\|} \tag{3-26}$$

The set of twelve analytical redundancy relations that were derived in this section will be used in the following sections to detect the sensor faults.

3.3 Roll and Pitch Dynamics

In this section, two observers are designed to estimate the vehicle body's roll and pitch angular rates as well as the road grade and bank disturbances. These estimations will be used to cross-check the roll rate and the pitch rate sensor measurements and detect any respective faults. The observers are designed using the roll and pitch dynamic models shown in Figure 3.3.

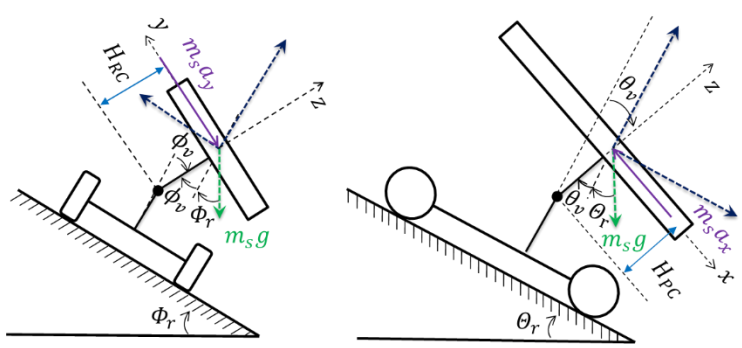

Figure 3.3. Roll and pitch dynamics on roads with grade and bank angles

The roll and pitch dynamics are formulated in (3-27) and (3-28), respectively:

$$\begin{bmatrix}\dot{\phi}_v\\ \ddot{\phi}_v\end{bmatrix} = \begin{bmatrix}0 & 1\\ \frac{-K_\phi}{I_x+m_s H_{RC}^2} & \frac{-C_\phi}{I_x+m_s H_{RC}^2}\end{bmatrix}\begin{bmatrix}\phi_v\\ \dot{\phi}_v\end{bmatrix} + \begin{bmatrix}0\\ \frac{m_s H_{RC}}{I_x+m_s H_{RC}^2}\end{bmatrix}[\dot{v}_y + v_x\dot{\psi} + gsin(\phi_v + \Phi_r)] \tag{3-27}$$

$$\begin{bmatrix}\dot{\theta}_v\\ \ddot{\theta}_v\end{bmatrix} = \begin{bmatrix}0 & 1\\ \frac{-K_\theta}{I_y+m_s H_{PC}^2} & \frac{-C_\theta}{I_y+m_s H_{PC}^2}\end{bmatrix}\begin{bmatrix}\theta_v\\ \dot{\theta}_v\end{bmatrix} + \begin{bmatrix}0\\ \frac{m_s H_{PC}}{I_y+m_s H_{PC}^2}\end{bmatrix}[-\dot{v}_x + v_y\dot{\psi} + gsin(\theta_v + \Theta_r)] \tag{3-28}$$

where $\dot{\theta}_v$ and $\dot{\phi}_v$ are the body pitch and roll rates, respectively, Θ_r is the road grade angle and Φ_r is the road bank angle. The vehicle longitudinal and lateral velocities (v_x and v_y) and the yaw rate ($\dot{\psi}$) are the inputs to the observers. I_x and I_y represent the moments of inertia about the x and y axes of the body coordinate frame, respectively, m_s is the sprung mass, g is the gravitational acceleration, C_θ and K_θ are pitch damping and stiffness coefficients, respectively and C_ϕ and K_ϕ are roll damping and stiffness coefficients, respectively. H_{PC} represents the distance between the pitch center (PC) and the center of gravity (CG) and H_{RC} is the distance between the roll center (RC) and CG.

For implementation on a vehicle, the model is discretized with a sample time of 0.005 seconds using the method described in [88]. The sample time is set to 0.005 seconds. Consider the discretized version of the roll dynamics:

$$x_\phi[k+1] = A_\phi x_\phi[k] + B_\phi u_\phi[k] \tag{3-29}$$

$$y_\phi[k] = C_\phi x_\phi[k] + D_\phi u_\phi[k] \tag{3-30}$$

where $x_\phi \in \mathbb{R}^2$ is the state vector, $y_\phi \in \mathbb{R}^1$ is the output and $u_\phi \in \mathbb{R}^1$ is the input. Since the road bank angle is not measurable using onboard vehicle sensors, the input term $\left(u_\phi[k] = \dot{v}_y + v_x\dot{\psi} + gsin(\phi_v + \Phi_r)\right)$ is treated as an unknown input into the roll dynamics.

3.4 Unknown Input Observers for Roll and Pitch Dynamics

An unknown input observer (UIO) [89][90] is designed here to estimate the road bank angle (Φ_r) along with the roll rate of the vehicle body ($\dot{\phi}_v$). The available measurement for the observer is the roll angle of the vehicle body ($\hat{\phi}_v$) obtained by the suspension height sensors as described in the previous section.

The output of the system (3-30) over $L+1$ time steps can be augmented as:

$$\underbrace{\begin{bmatrix} y_\phi[k] \\ y_\phi[k+1] \\ \vdots \\ y_\phi[k+L] \end{bmatrix}}_{y_\phi[k:k+L]} = \underbrace{\begin{bmatrix} C_\phi \\ C_\phi A_\phi \\ \vdots \\ C_\phi A_\phi^L \end{bmatrix}}_{\mathcal{O}_{L\phi}} x_\phi[k] + \underbrace{\begin{bmatrix} D_\phi & 0 & \dots & 0 \\ C_\phi B_\phi & D_\phi & \dots & 0 \\ \vdots & \vdots & \ddots & \vdots \\ C_\phi A_\phi^{L-1} B_\phi & C_\phi A_\phi^{L-2} B_\phi & \cdots & D_\phi \end{bmatrix}}_{\mathcal{J}_{L\phi}} \underbrace{\begin{bmatrix} u_\phi[k] \\ u_\phi[k+1] \\ \vdots \\ u_\phi[k+L] \end{bmatrix}}_{u_\phi[k:k+L]} \tag{3-31}$$

where $\mathcal{O}_{L\phi} \in \mathbb{R}^{(L+1)\times 2}$ is the observability matrix for the pair (A_ϕ, C_ϕ) and the $\mathcal{J}_{L\phi} \in \mathbb{R}^{(L+1)\times 2(L+1)}$ is called the invertibility matrix for the system $(A_\phi, B_\phi, C_\phi, D_\phi)$ [90].

An unknown input observer can be designed for this system to estimate the state $x_\phi[k]$ and the unknown input $u_\phi[k{:}\,k+L]$ if and only if the system is strongly detectable, which translates to satisfying the following conditions for some positive integer L [90]:

$$rank(\mathcal{J}_{L\phi}) - rank(\mathcal{J}_{L\phi-1}) = n_u \tag{3-32}$$

$$rank\begin{bmatrix} A_\phi - zI_n & B_\phi \\ C_\phi & D_\phi \end{bmatrix} = n_u + n_x \quad \forall z \in \mathbb{C},\ \ |z| \geq 1 \tag{3-33}$$

where n_u is the number of inputs and n_x is the number of states.

Verifying that the system satisfies the conditions (3-32)-(3-33) for $L = 1$ is straightforward. Therefore, since the system is strongly detectable, an unknown input observer with the following form is proposed to simultaneously estimate the roll states ($x_\phi[k]$) and the unknown input ($u_\phi[k]$):

$$\hat{x}_\phi[k+1] = E_\phi \hat{x}_\phi[k] + F_\phi y_\phi[k{:}\,k+L] \tag{3-34}$$

$$\hat{u}_\phi[k] = \begin{bmatrix} B_\phi \\ D_\phi \end{bmatrix}^{-1} \begin{bmatrix} \hat{x}_\phi[k+1] - A_\phi \hat{x}_\phi[k] \\ y_\phi[k] - C_\phi \hat{x}_\phi[k] \end{bmatrix} \tag{3-35}$$

where $E_\phi \in \mathbb{R}^2$ and $F_\phi \in \mathbb{R}^{2\times(L+1)}$ are the observer gain matrices. To analyze stability of the observer, the state estimation error is defined as:

$$e_\phi[k+1] = \hat{x}_\phi[k+1] - x_\phi[k+1] \tag{3-36}$$

The error dynamics can be calculated using (3-29), (3-30), (3-31), (3-34) and (3-36):

$$e_\phi[k+1] = E_\phi e_\phi[k] + \left(E_\phi - A_\phi + F_\phi O_{L\phi}\right) x_\phi[k] + F_\phi J_{L\phi} u_\phi[k{:}\,k+L] - B_\phi u_\phi[k] \tag{3-37}$$

By choosing E_ϕ and F_ϕ gains such that

a) $\left|\lambda_i(E_\phi)\right| < 1$ (3-38)

b) $E_\phi - A_\phi + F_\phi \mathcal{O}_{L\phi} = 0$ (3-39)

c) $F_\phi J_{L\phi} = \left[B_\phi\ 0 \ldots 0\right]$ (3-40)

where $\lambda_i(E_\phi)$ is the i-th ($i \in \{1, 2\}$) eigenvalue of the matrix E_ϕ, the error dynamics is asymptotically stable and $e[k] \to 0$. Therefore, $\hat{x}_\phi[k] \to x_\phi[k]$ and $\hat{x}_\phi[k+1] \to \hat{x}_\phi[k+1]$, and the states can be estimated. Consequently, using the proposed observer, roll rate of the body ($\hat{\dot{\phi}}_v$) is estimated without

using the roll rate sensor itself. Four independent estimations for the roll rate $\left(\hat{\dot{\phi}}_{v_{-ij}},\ ij \in \{fl, fr, rll, rr\}\right)$ are obtained using this observer when it is fed with the calculated roll angles from the previous section ($\hat{\phi}_{v_{-ij}}$). Moreover, stability of the error dynamics (3-37) together with the system model (3-29)-(3-30) and the unknown input equation (3-35) guarantee that $\hat{u}_{\phi}[k] \rightarrow u_{\phi}[k]$. Consequently, the road bank angle (Φ_r) can be estimated using the observer after the unknown input is estimated from (3-35):

$$\hat{u}_{\phi}[k] = \dot{v}_y[k] + v_x[k]\dot{\psi}[k] + gsin(\hat{\phi}_v[k] + \hat{\Phi}_r[k]) \tag{3-41}$$

$$\hat{\Phi}_r[k] = sin^{-1}\left(\frac{\hat{u}_{\phi}[k] - \dot{v}_y[k] - v_x[k]\dot{\psi}[k]}{g}\right) - \hat{\phi}_v[k] \tag{3-42}$$

where yaw rate of the vehicle ($\dot{\psi}$) is measured by the IMU sensor in commercial vehicles. Longitudinal and lateral velocity of the vehicle (v_x and v_y) can be estimated using available approaches in the literature [91] and will be discussed in the next chapters.

Following the same process, a similar observer is designed to estimate the pitch rate of the vehicle body ($\dot{\theta}_v$) and the unknown road grade angle (Θ_r):

$$\hat{x}_{\theta}[k+1] = E_{\theta}\hat{x}_{\theta}[k] + F_{\theta}y_{\theta}[k{:}\,k+L] \tag{3-43}$$

$$\hat{u}_{\theta}[k] = \begin{bmatrix} B_{\theta} \\ D_{\theta} \end{bmatrix}^{-1} \begin{bmatrix} \hat{x}_{\theta}[k+1] - A_{\theta}\hat{x}_{\theta}[k] \\ y_{\theta}[k] - C_{\theta}\hat{x}_{\theta}[k] \end{bmatrix} \tag{3-44}$$

Stability and convergence of the pitch observer can be proven following the same process described earlier. The measurement for the pitch observer is the pitch angle of the vehicle body. Four independent estimations of the pitch rate $\left(\hat{\dot{\theta}}_{v_{-ij}},\ ij \in \{fl, fr, rll, rr\}\right)$ can be obtained when the observer is fed with the four estimated roll angles from the suspension kinematics in the previous section.

Consequently, the road grade angle (Θ_r) can be estimated using the pitch UIO, after the unknown input is estimated from (3-44):

$$\hat{u}_{\theta}[k] = -\dot{v}_x[k] + v_y[k]\dot{\psi}[k] + gsin(\theta_v[k] + \Theta_r[k]) \tag{3-45}$$

$$\hat{\Theta}_r[k] = sin^{-1}\left(\frac{\hat{u}_{\theta}[k] + \dot{v}_x[k] - v_y[k]\dot{\psi}[k]}{g}\right) - \hat{\theta}_v[k] \tag{3-46}$$

3.5 Analytical Redundancy Relations for Roll Rate and Pitch Rate Sensors

The measurements provided by the vehicle roll and pitch rate sensors ($\dot{\phi}_s$ and $\dot{\theta}_s$, respectively) are affected both by the vehicle body motion and the rate of change of the road bank and grade angles [87]. Estimations for the sensory roll and pitch rates are obtained in this section by using the estimated body roll rate, body pitch rate, road grade and road bank angles from the previous section.

In Figure 3.2, the auxiliary coordinate system (x_A, y_A, z_A) represents a rotation of the global coordinates about the z_G axis. Magnitude of this rotation is equal to the vehicle yaw angle (ψ) [92]. The vehicle frame coordinate system (x_F, y_F, z_F) is fixed on the frame. The global coordinates (x_G, y_G, z_G) can be transformed to the vehicle frame axes using Euler angles ψ, θ and ϕ. These angles are successive rotations about z_G, y_A and x_F, respectively. The angular velocity of the frame relative to the global axis system can be described as:

$$\dot{\Omega}_F = \mathcal{R}_F^G \dot{\Omega} \tag{3-47}$$

in which $\dot{\Omega} = [\dot{\phi} \quad \dot{\theta} \quad \dot{\psi}]^T$ represents the rate of Euler angles and $\dot{\Omega}_F = [\dot{\phi}_F \quad \dot{\theta}_F \quad \dot{\psi}_F]^T$ is the rotation rate of the frame relative to the global coordinates. The rotation matrix R_F^G can be expressed as:

$$\mathcal{R}_F^G = \mathcal{R}_{x_F,\phi} \begin{bmatrix} \dot{\phi} \\ 0 \\ 0 \end{bmatrix} + \mathcal{R}_{\ y_A,\theta} \begin{bmatrix} 0 \\ \dot{\theta} \\ 0 \end{bmatrix} + \mathcal{R}_{x_F,\phi}\, \mathcal{R}_{y_A,\theta}\, \mathcal{R}_{z_G,\psi} \begin{bmatrix} 0 \\ 0 \\ \dot{\psi} \end{bmatrix} \tag{3-48}$$

where $\mathcal{R}_{F,\phi}$ shows rotation by an angle ϕ about the x_F axis, $\mathcal{R}_{y_A,\theta}$ is rotation by an angle θ about the y_A axis, and $\mathcal{R}_{z_G,\psi}$ represents rotation by an angle ψ about the z_G axis. $\mathcal{R}_F^G$ can be found by substituting these rotation matrices in (3-48):

$$\mathcal{R}_F^G = \begin{bmatrix} 1 & 0 & -\sin(\theta) \\ 0 & \sin(\phi) & \sin(\phi)\cos(\theta) \\ 0 & -\sin(\phi) & \cos(\phi)\cos(\theta) \end{bmatrix} \tag{3-49}$$

Road grade (Θ_r), road bank (Φ_r) and relative heading (Ψ_r) angles are rotations between the vehicle frame and the auxiliary axis system (x_A, y_A, z_A). The rate of change of the road angles $\dot{\Omega}_r = [\dot{\Theta}_r \quad \dot{\Phi}_r \quad \dot{\Psi}_r]^T$ is equal to the angular velocity of the vehicle frame relative to the auxiliary coordinate system and can be expressed using the following transformation:

$$\dot{\Omega}_r = \left(\mathcal{R}_{y_a,\theta}\right)^T \begin{bmatrix} \dot{\phi} \\ 0 \\ 0 \end{bmatrix} + \begin{bmatrix} 0 \\ \dot{\theta} \\ 0 \end{bmatrix} = \begin{bmatrix} \cos(\theta) & 0 & 0 \\ 0 & 1 & 0 \\ -\sin(\theta) & 0 & 0 \end{bmatrix} \dot{\Omega} \tag{3-50}$$

Substituting $\dot{\Omega}$ from (3-47) into (3-50) yields:

$$\dot{\Omega}_r = \begin{bmatrix} \cos(\theta) & \sin(\phi)\sin(\theta) & \cos(\phi)\sin(\theta) \\ 0 & \cos(\phi) & -\sin(\phi) \\ -\sin(\theta) & -\sin(\phi)\sin(\theta)\tan(\theta) & -\cos(\phi)\sin(\theta)\,tan(\theta) \end{bmatrix} \dot{\Omega}_F = \mathcal{R}_r^F \dot{\Omega}_F \tag{3-51}$$

where $\mathcal{R}_r^F$ represents the transformation between the road and frame angles. The relative road heading (Ψ_r) is not a focus of this thesis. For road grade and bank angles, (3-51) can be reduced to:

$$\dot{\Omega}_r = \begin{bmatrix} \cos(\theta) & sin(\phi)\sin(\theta) & \cos(\phi)\sin(\theta) \\ 0 & \cos(\phi) & -\sin(\phi) \end{bmatrix} \dot{\Omega}_F = \chi_r^F \dot{\Omega}_F \tag{3-52}$$

where the reduced $\dot{\Omega}_r = [\dot{\Theta}_r \quad \dot{\Phi}_r\,]^T$ represents the rate of the change of the road grade and bank angles and χ_r^F is the rotation matrix from the road to the frame. Therefore, frame rotation rates can be expressed using the pseudo inverse $(\chi_r^F)^{-1}$:

$$\dot{\Omega}_F = (\chi_r^F)^{-1}\dot{\Omega}_r \tag{3-53}$$

Roll and pitch rate sensors are mounted on the vehicle sprung mass which has the body-fixed coordinate system (x_B, y_B, z_B). These sensed angular rates $\dot{\Omega}_s = [\dot{\phi}_s \quad \dot{\theta}_s \quad \dot{\psi}_s]^T$ are influenced by angular rates of the body relative to the frame $\dot{\Omega}_v = [\dot{\phi}_v \quad \dot{\theta}_v \quad \dot{\psi}_v]^T$ and the frame angular rate $\dot{\Omega}_F$:

$$\dot{\Omega}_s = \dot{\Omega}_v + \mathcal{R}_B^F \dot{\Omega}_F \tag{3-54}$$

Since the body-fixed coordinate system has consecutive rotations of ϕ_v around x_F and θ_v around the y_F axis of the vehicle frame, the rotation matrix $\mathcal{R}_B^F$ can be obtained as:

$$\mathcal{R}_B^F = \begin{bmatrix} \cos(\theta_v) & \sin(\phi_v)\sin(\theta_v) & -\cos(\phi_v)\sin(\theta_v) \\ 0 & \cos(\phi_v) & \sin(\phi_v) \\ \sin(\theta_v) & -\cos(\theta_v)\sin(\phi_v) & \cos(\phi_v)\cos(\theta_v) \end{bmatrix} \approx \begin{bmatrix} 1 & 0 & 0 \\ 0 & \cos(\phi_v) & \sin(\phi_v) \\ 0 & -\sin(\phi_v) & \cos(\phi_v) \end{bmatrix} \tag{3-55}$$

The relationship between the roll/pitch rate sensor measurements, vehicle pitch/roll rate, and road angle rates can be described by substituting (3-53) and (3-54) in (3-55):

$$\dot{\Omega}_s = \dot{\Omega}_v + \mathcal{R}_B^F (\chi_r^F)^{-1}\dot{\Omega}_r = \dot{\Omega}_v + \mathcal{R}_B^r \dot{\Omega}_r \tag{3-56}$$

where $\mathcal{R}_B^r = R_b^f \left(\chi_r^f\right)^{-1}$ shows the rotation between the road and the body-fixed axes. Conclusively, the analytical redundancy relation between roll/pitch sensor measurements, body angular rates and road angular rates can be summarized as:

$$\dot{\phi}_s = \dot{\phi}_v + \mathcal{R}^r_{B_1}(\theta_v, \phi_v)\dot{\Phi}_r \tag{3-57}$$

$$\dot{\theta}_s = \dot{\theta}_v + \mathcal{R}^r_{B_2}(\theta_v, \phi_v)\dot{\Theta}_r \tag{3-58}$$

where $\mathcal{R}^r_{B_1}, \mathcal{R}^r_{B_2}$ are components of $\mathcal{R}^r_B = [\mathcal{R}^r_{B_1} \quad \mathcal{R}^r_{B_2}]^T$. Various estimated body roll and pitch angles from the UIOs can be fed into (3-57)-(3-59) to obtain estimates for the roll rate and pitch rate sensors, when certain suspension height measurements are not used in the process:

$$\hat{\dot{\phi}}_{s_{-ij}} = \hat{\dot{\phi}}_{v_{-ij}} + \mathcal{R}^r_{B_1}\left(\hat{\theta}_{v_{-ij}}, \hat{\phi}_{v_{-ij}}\right)\hat{\dot{\Phi}}_{r_{-ij}} \tag{3-59}$$

$$\hat{\dot{\theta}}_{s_{-ij}} = \hat{\dot{\theta}}_{v_{-ij}} + \mathcal{R}^r_{B_2}\left(\hat{\theta}_{v_{-ij}}, \hat{\phi}_{v_{-ij}}\right)\hat{\dot{\Theta}}_{r_{-ij}} \tag{3-60}$$

3.6 Detection and Isolation of Sensor Faults

Figure 3.4. summarizes the previous sections and shows the process to estimate the analytically redundant roll rate, pitch rate and suspension heights.

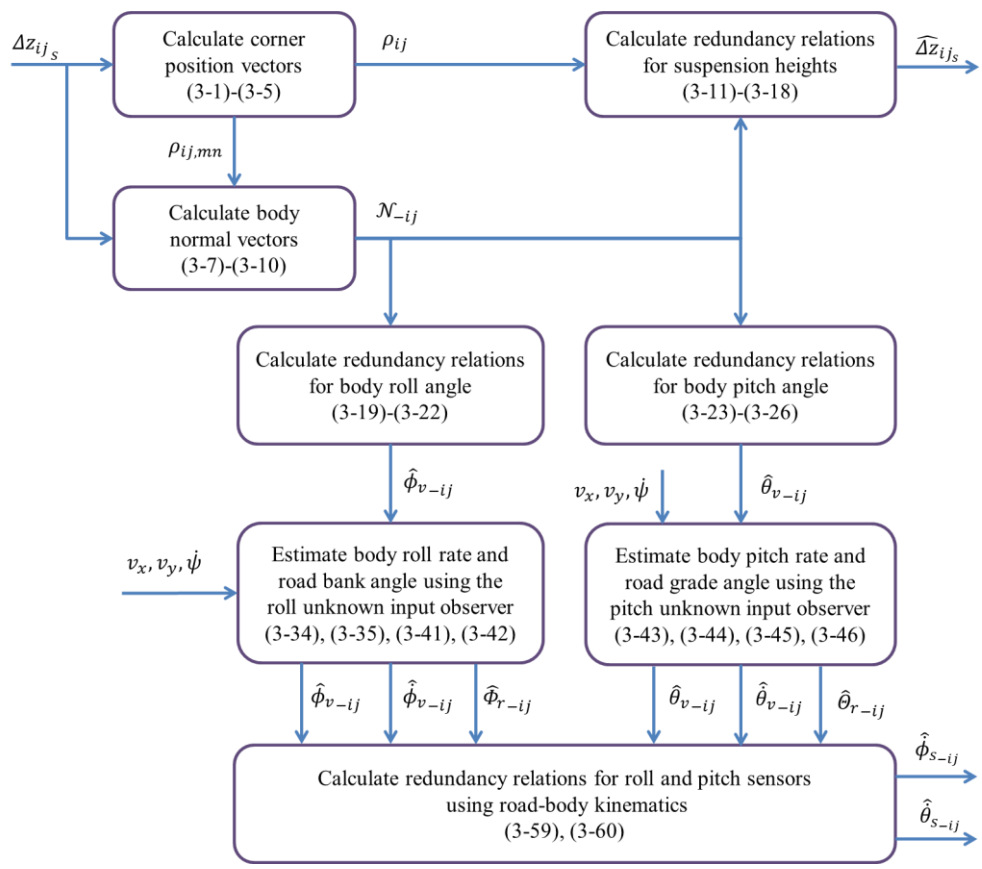

Figure 3.4. Estimation of redundant roll rate, pitch rate and suspension heights

The estimated outputs $\left(\widehat{\Delta z}_{ij_s}, \hat{\phi}_{s_{-ij}}, \hat{\theta}_{s_{-ij}},\ ij \in \{fl, fr, rll, rr\}\right)$ are used in the following sections to generate the residuals, detect sensor faults and reconstruct the faulty sensory signals.

3.6.1 Generating and Processing Suspension Height Residuals

For each corner, the suspension height residual ($R_{z_{ij}}$) is defined as the difference between the estimated height ($\widehat{\Delta z}_{ij}$) and the measured height by the sensor (Δz_{ij_s}):

$$R_{z_{ij}} = \left|\Delta z_{ij_s} - \widehat{\Delta z}_{ij}\right| \qquad ij \in \{fl, fr, rll, rr\} \tag{3-61}$$

Four residuals are created, each corresponding to one corner. When there is no fault in the system, residuals fall below a certain threshold. While many available studies in the literature use fixed thresholds [93], there are some drawbacks:

- Disturbances, nonlinearities and uncertainties may cause spikes or larger than normal residuals, even when there is no sensor fault, which can cause false positives.
- If a larger fixed fault threshold is used to reduce false positives, then the algorithm will not be able to detect the faults with smaller magnitudes (i.e. will be prone to false negatives) and/or will be slower (higher excitation and more time is required for the residuals to pass the large threshold).

To overcome such difficulties, adaptive fault thresholds are developed in this thesis to evaluate the residuals more effectively for a more reliable fault detection. The adaptive thresholds are calculated based on driving conditions. The threshold for the suspension height residuals is formulated as:

$$T_z = B_{s_z} + B_{d_z}\left(|a_x| + |a_y|\right) \tag{3-62}$$

where T_z is the fault threshold, B_{s_z} is a static bound that determines a fixed minimum value for the threshold and B_{d_z} is a constant gain that adds the effects of longitudinal and lateral excitations to the threshold. In this thesis, the static fault thresholds are set to 10% of the operational range of the sensory signals. Dynamic thresholds are tuned over a set of vehicle maneuvers (including harsh maneuvers at the stability limits) to achieve zero false positives in the test scenarios. Such a tuning can reduce the risk of false positives in the real-world driving scenarios.

For further robustness against false positives in transient regions, evaluation of the adaptive threshold is performed over a time window as:

$$T_{d,z} = \max\left(T_z[k], T_z[k-1] \ldots, T_z[k-W_z]\right) \tag{3-63}$$

where W_z is the length of the time window and $T_{d,z}$ is the dynamic fault threshold. When a residual exceeds the dynamic threshold ($R_{z_{ij}} > T_{d_z}$), a fault state counter ($n_{z_{ij}}$, initially set to zero) is incremented in the algorithm:

$$n_{z_{ij}}[k] = n_{z_{ij}}[k-1] + 1 \tag{3-64}$$

Although every single incidence of crossing the threshold can be treated as fault, practically and by definition, a malfunction should persist over a period of time to be labeled as a fault [29]. In this thesis, if a residual $R_{z_{ij}}$ is above the threshold (i.e. the fault persists) for N_z consecutive sample times ($n_{zij} > N_z$), the algorithm concludes that the malfunction is persisting and sets a fault state $S_{z_{ij}}$ to one. However, failure of each corner sensor will result in all four residuals to exceed the thresholds due to the kinematic relation between the corner heights. Subsequently, four fault states are perceived and their corresponding flag is set to one. Hence, the fault cannot yet be localized by only using the suspension height residuals and fault states. The four fault states $S_{z_{ij}}$, which have the same value, are therefore combined into a single fault state S_z. Localization of the fault will be performed using the roll/pitch rate residuals and a decision logic module described in the next sections.

3.6.2 Generating and Processing Roll Rate Residuals

Four roll rate residuals ($R_{\phi_{-ij}}$) are formulated which indicate the difference between the estimated roll rates and the roll rate sensor measurement:

$$R_{\phi_{-ij}} = \left|\dot{\phi}_s - \hat{\dot{\phi}}_{s\ -ij}\right| \qquad ij \in \{fl, fr, rll, rr\} \tag{3-65}$$

The threshold for the roll rate is constructed as:

$$T_\phi = B_{s_\phi} + B_{d_\phi}\left(\left|a_y\right|\right) \tag{3-66}$$

$$T_{d,\phi} = max\left(T_\phi[k], T_\phi[k-1], \ldots, T_\phi[k-W_\phi]\right) \tag{3-67}$$

where B_{s_ϕ} determines a fixed static bound for the threshold, the constant B_{d_ϕ} adds the effect of lateral excitations to the threshold, and W_ϕ is the length of the time window to calculate the dynamic threshold ($T_{d,\phi}$). A fault state counter ($n_{\phi_{-ij}}$, initially set to zero) is incremented in the algorithm if a residual $R_{\phi_{-ij}}$ is above the threshold ($R_{\phi_{-ij}} > T_{d,\phi}$):

$$n_{\phi_{-ij}}(k) = n_{\phi_{-ij}}(k-1) + 1 \tag{3-68}$$

If the fault persists for $N_{\phi_{-ij}}$ consecutive sample times ($n_{\phi_{-ij}} > N_{\phi_{-ij}}$), the algorithm sets the corresponding fault state ($S_{\phi_{-ij}}$) to one.

3.6.3 Generating and Processing Pitch Rate Residuals

Similar to the previous section, four pitch rate residuals ($R_{\theta_{-ij}}$) are formulated which indicate the difference between the estimated pitch rates and the pitch rate measured by the sensor:

$$R_{\theta_{-ij}} = \left|\dot{\theta}_s - \hat{\dot{\theta}}_{s\ -ij}\right| \qquad ij \in \{fl, fr, rll, rr\} \tag{3-69}$$

The threshold for the pitch rate is defined as:

$$T_\theta = B_{s_\theta} + B_{d_\theta}(|a_x|) \tag{3-70}$$

$$T_{d,\theta} = max(T_\theta[k], T_\theta[k-1], \dots, T_\theta[k-W_\theta]) \tag{3-71}$$

Definitions of $B_{s_\theta}, B_{d_\theta}, W_\theta$ and $n_{\theta_{-ij}}$ are similar to the previous section. If a residual $R_{\theta_{-ij}}$ is above the dynamic threshold ($R_{\theta_{-ij}} > T_{d,\theta}$) the fault state counter is incremented:

$$n_{\theta_{-ij}}[k] = n_{\theta_{-ij}}[k-1] + 1 \tag{3-72}$$

The algorithm sets the corresponding fault state ($S_{\theta_{-ij}}$) to one if the fault persists for $N_{\theta_{-ij}}$ consecutive sample times ($n_{\theta_{-ij}} > N_{\theta_{-ij}}$).

3.6.4 Decision Logic for Detection and Isolation of Sensor Faults

Detection and localization of sensor faults is performed using the residuals described in the previous sections. Consider a case where the suspension height sensors and the pitch rate sensor are healthy, and the roll rate sensor is faulty. In this case, the following behavior is expected:

- The suspension height residuals in (3-61) are not impacted by the roll rate sensor fault and fall below their thresholds. Therefore, the fault state for the suspension height sensors is equal to zero $[S_z] = [0]$.
- The inputs to the roll observer ($\hat{\phi}_{v_{-ij}}, ij \in \{fl, fr, rl, rr\}$) are correct since these inputs are calculated using the healthy suspension height sensors. Therefore, the observer can accurately

estimate the vehicle's roll rate. Since the roll rate sensor is faulty, its measurement ($\dot{\phi}_s$) would not match with the four estimated roll rates from the observer ($\hat{\dot{\phi}}_{s\ -ij}, ij \in \{fl, fr, rl, rr\}$). Consequently, the roll residuals in (3-65) exceed the thresholds and result in four roll fault states equal to one $[S_{\phi_{-fl}}\ S_{\phi_{-fr}}\ S_{\phi_{-rl}}\ S_{\phi_{-rr}}] = [1\ 1\ 1\ 1]$.

- The inputs to the pitch UIO ($\hat{\theta}_{v_{-ij}}$) are correct since these inputs are calculated using the healthy suspension height sensors. Therefore, the estimated pitch rates by the observer ($\hat{\dot{\theta}}_{s\ -ij}, ij \in \{fl, fr, rl, rr\}$) are accurate and match the pitch rate measurement from the healthy pitch rate sensor $(\dot{\theta}_s)$. Consequently, Pitch rate residuals in (3-69) all fall below their thresholds and pitch fault states are equal to zero $[S_{\theta_{-fl}}\ S_{\theta_{-fr}}\ S_{\theta_{-rl}}\ S_{\theta_{-rr}}] = [0\ 0\ 0\ 0]$.

Combining the above fault states generates a fault signature for the roll rate sensor fault: $[S_z\ S_{\phi_{-fl}}\ S_{\phi_{-fr}}\ S_{\phi_{-rl}}\ S_{\phi_{-rr}}\ S_{\theta_{-fl}}\ S_{\theta_{-fr}}\ S_{\theta_{-rl}}\ S_{\theta_{-rr}}] = [0\ 1\ 1\ 1\ 1\ 0\ 0\ 0\ 0]$.

Similarly, fault signatures can be obtained for the other possible sensor faults as listed in Table 3-1. As an example, Table 3.1 shows that failure of the front-left suspension height sensor generates the fault signature $[S_z\ S_{\phi_{-fl}}\ S_{\phi_{-fr}}\ S_{\phi_{-rl}}\ S_{\phi_{-rr}}\ S_{\theta_{-fl}}\ S_{\theta_{-fr}}\ S_{\theta_{-rl}}\ S_{\theta_{-rr}}] = [1\ 0\ 0\ 1\ 1\ 0\ 1\ 0\ 1]$.

Table 3.1. Fault signatures for isolation of roll rate, pitch rate and suspension height sensor faults

Fault Signature	Faulty Sensor						
	Δz_{fl_s}	Δz_{fr_s}	Δz_{rl_s}	Δz_{rr_s}	$\dot{\phi}_s$	$\dot{\theta}_s$	No Fault
S_z	1	1	1	1	0	0	0
$S_{\phi_{-fl}}$	0	0	1	1	1	0	0
$S_{\phi_{-fr}}$	0	0	1	1	1	0	0
$S_{\phi_{-rl}}$	1	1	0	0	1	0	0
$S_{\phi_{-rr}}$	1	1	0	0	1	0	0
$S_{\theta_{-fl}}$	0	1	0	1	0	1	0
$S_{\theta_{-fr}}$	1	0	1	0	0	1	0
$S_{\theta_{-rl}}$	0	1	0	1	0	1	0
$S_{\theta_{-rr}}$	1	0	1	0	0	1	0

These fault signatures will be used in the next sections to detect and isolate the sensor faults.

3.7 Fault Detectability and Isolability Analysis

The information in Table 3-1 can be summarized into a fault signature matrix G to analyze detectability and isolability of the faults [94]. In the absence of noises and disturbances, G can be considered as a transfer function between the fault vector $\mathcal{F}$ and the fault state vector (or residual vector) $\mathcal{S}$:

$$\mathcal{S} = G\,\mathcal{F} \tag{3-73}$$

For n_F number of faults and n_R number of residuals, G is a $n_R \times n_F$ matrix. Each element in this matrix, $G(p,q)$, represents sensitivity of the fault state (or residual) p to the fault in sensor q. Using the fault signature matrix G and by defining G_q as the column q in G, fault detectability, complete fault detectability and fault isolability conditions can be checked for (3-73) as follows (derived from [94]):

1) Fault detectability: fault q is detectable if and only if $rank[G_q] > 0$.
2) Complete fault detectability: the system is completely fault detectable (i.e., all sensor faults can be detected) if and only if $rank[G_q] > 0$ for all $q = 1, \dots, n_F$.
3) Fault isolability: fault q is isolable (i.e., the faulty sensor can be localized) if and only if G_q is a unique column in G.

For the fault vector $\mathcal{F} = \left[\mathcal{F}_{\Delta z_{fl_s}}\ \mathcal{F}_{\Delta z_{fr_s}}\ \mathcal{F}_{\Delta z_{rl_s}}\ \mathcal{F}_{\Delta z_{rr_s}}\ \mathcal{F}_{\dot{\phi}_s}\ \mathcal{F}_{\dot{\theta}_s}\right]^T$ and the fault state vector $\mathcal{S} = \left[S_z\ S_{\phi_{-fl}}\ S_{\phi_{-fr}}\ S_{\phi_{-rl}}\ S_{\phi_{-rr}}\ S_{\theta_{-fl}}\ S_{\theta_{-fr}}\ S_{\theta_{-rl}}\ S_{\theta_{-rr}}\right]^T$ in Table 3.1, the fault signature matrix can be expressed as:

$$G = \begin{bmatrix} 1 & 1 & 1 & 1 & 0 & 0 \\ 0 & 0 & 1 & 1 & 1 & 0 \\ 0 & 0 & 1 & 1 & 1 & 0 \\ 1 & 1 & 0 & 0 & 1 & 0 \\ 1 & 1 & 0 & 0 & 1 & 0 \\ 0 & 1 & 0 & 1 & 0 & 1 \\ 1 & 0 & 1 & 0 & 0 & 1 \\ 0 & 1 & 0 & 1 & 0 & 1 \\ 1 & 0 & 1 & 0 & 0 & 1 \end{bmatrix} \tag{3-74}$$

Since $rank[G_q] > 0$ for all columns in G and all columns are unique, the proposed fault detection algorithm satisfies the fault detectability, complete fault detectability and fault isolability conditions.

Consequently, all individual sensor faults $\mathcal{F}_{\Delta z_{fl_s}}, \mathcal{F}_{\Delta z_{fr_s}}, \mathcal{F}_{\Delta z_{rl_s}}, \mathcal{F}_{\Delta z_{rr_s}}, \mathcal{F}_{\dot{\phi}_s}$ and $\mathcal{F}_{\dot{\theta}_s}$ can be detected and localized using the proposed algorithm.

The result of this decision can be expressed in the format of a compact fault signature $\mathcal{S} = [S_{z_{fl}}\ S_{z_{fr}}\ S_{z_{rl}}\ S_{z_{rr}}\ S_{\dot{\phi}}\ S_{\dot{\theta}}]$ to indicate the faulty sensor.

3.8 Reconstruction of Faulty Signals

When a fault is detected by the algorithm, the faulty signal can be reconstructed using the estimated states as indicated in Table 3.2. This table is constructed using the outputs of the process in Figure 3.4 which generated the estimations for these signals.

Table 3.2. Reconstruction of roll rate, pitch rate and suspension height signals

Faulty sensor	Reconstructed signal	Input to the roll UIO	Input to the pitch UIO
Δz_{fl_s}	$\widehat{\Delta z}_{fl_s}$	$\hat{\phi}_{v-fl}$	$\hat{\theta}_{v-fl}$
Δz_{fr_s}	$\widehat{\Delta z}_{fr_s}$	$\hat{\phi}_{v-fr}$	$\hat{\theta}_{v-fr}$
Δz_{rl_s}	$\widehat{\Delta z}_{rl_s}$	$\hat{\phi}_{v-rl}$	$\hat{\theta}_{v-rl}$
Δz_{rr_s}	$\widehat{\Delta z}_{rr_s}$	$\hat{\phi}_{v-rr}$	$\hat{\theta}_{v-rr}$
$\dot{\phi}_s$	$\hat{\dot{\phi}}_s$	$\frac{1}{4}\sum_{ij}\hat{\phi}_{v-ij}$	$\frac{1}{4}\sum_{ij}\hat{\theta}_{v-ij}$
$\dot{\theta}_s$	$\hat{\dot{\theta}}_s$	$\frac{1}{4}\sum_{ij}\hat{\phi}_{v-ij}$	$\frac{1}{4}\sum_{ij}\hat{\theta}_{v-ij}$

3.9 Experiment Results

Figure 3.5 shows the electrified SUV that is used for experimental verification of the methos in this thesis. The vehicle is equipped with multiple sensors and onboard processing units in addition to the stock vehicle sensors.

The RT2500 Inertial and GPS Navigation Systems from OxTS Company is used to measure the longitudinal, lateral and vertical accelerations as well as roll, yaw and pitch rates. Four suspension height measurement sensors from Delphi Company are installed on the four corners of the vehicle to measure deflection of each corner. Four additional laser height measurement sensors are also mounted on the four corners to verify the fault detection results. Data from these laser sensors is not used in the fault detection algorithms. All sensors transmit their data over the CAN-bus communication channel. A dSPACE Autobox controller is used as the onboard processor to receive the sensor data and execute

the fault detection algorithm. The algorithm is developed in MATLAB/Simulink, compiled using the dSPACE target compiler and implemented in the Autobox controller. Sampling rate for the sensor data and execution rate of the embedded code is 200 Hz.

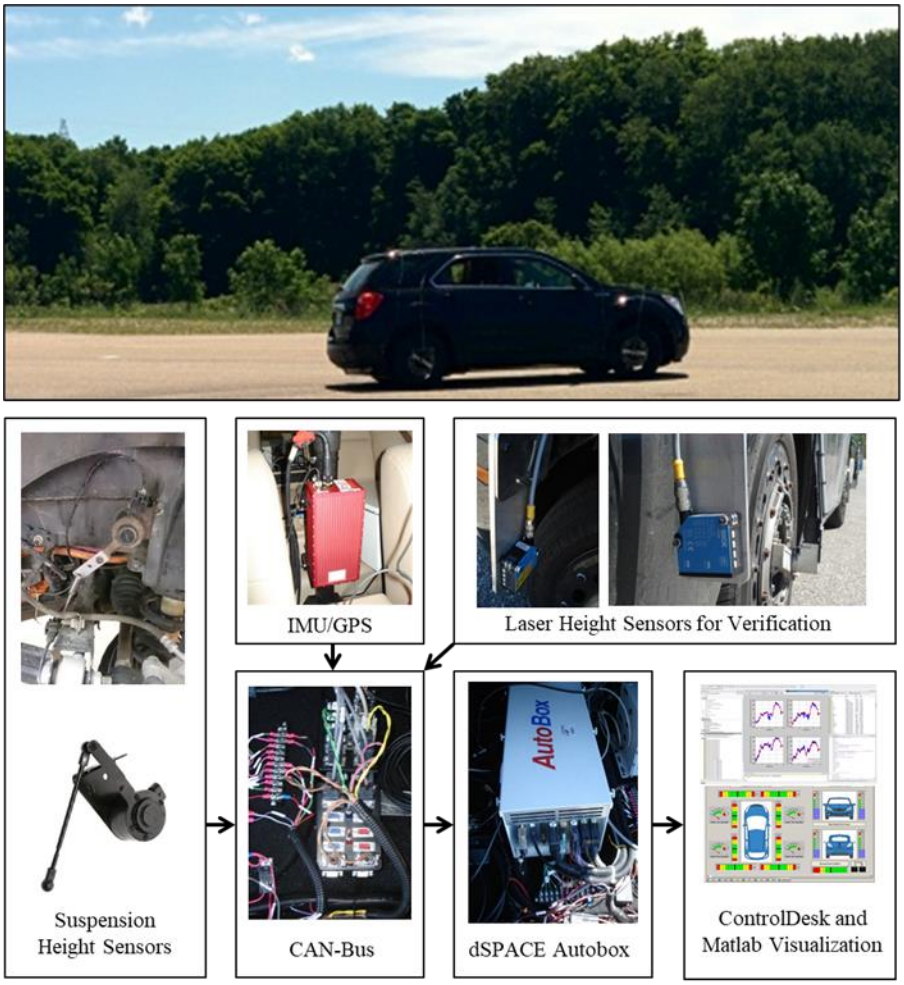

Figure 3.5. Test vehicle, sensors and instrumentation setup

Accuracy of the signal reconstruction process after detection of the fault is evaluated using the normalized root mean square of the error (NRMSE) metric:

$$NRMSE = \frac{\sqrt{\sum_{k=k_r}^{k_r+k_q}\left(\hat{q}(k)-q(k)\right)^2/k_q}}{\max\limits_{k=k_r,\ldots,k_r+k_q}(|q(k)|)} \tag{3-75}$$

where k_r is the first sample time when reconstruction begins, k_q is the number of reconstructed samples during the maneuver, $\hat{q}$ is the reconstructed signal and q is the actual signal.

Vehicle parameters are obtained through manufacturer data or by online identification [95][96]. Table 3.3 summarizes these parameters. The parameters used in the fault detection algorithm are summarized in Table 3.4.

Table 3.3. Vehicle parameters

Parameter	Description	Unit	Value
C_θ	Pitch damping coefficient	$[N.s/m]$	2.52×10^4
C_ϕ	Roll damping coefficient	$[N.s/m]$	0.63×10^4
d	Track width	$[m]$	1.62
H_{CG}	Distance from ground to CG	$[m]$	0.647
H_{PC}	Distance from pitch center to CG	$[m]$	0.54
H_{RC}	Distance from roll center to CG	$[m]$	0.54
I_x	Roll moment of inertia	$[kg.m^2]$	967
I_y	Pitch moment of inertia	$[kg.m^2]$	2710
I_z	Yaw moment of inertia	$[kg.m^2]$	4600
I_w	Wheel moment of inertia	$[kg.m^2]$	3.6
K_θ	Pitch stiffness coefficient	$[N/m]$	2.08×10^5
K_ϕ	Roll stiffness coefficient	$[N/m]$	1.51×10^5
L_f	Distance from front axle to CG	$[m]$	1.41
L_r	Distance from rear axle to CG	$[m]$	1.43
m_s	Sprung mass	$[kg]$	1989
m	Total vehicle mass	$[kg]$	2270
r_e	Effective tire radius	$[m]$	0.32

Table 3.4. Parameters for residual processing and sensor fault detection

Parameter	Value	Parameter	Value	Parameter	Value
B_{s_ϕ}	0.05	B_{s_θ}	0.05	B_{s_z}	0.01
B_{d_ϕ}	0.002	B_{d_θ}	0.002	B_{d_z}	0.0015
$N_{\phi_{-ij}}$	20	$N_{\theta_{-ij}}$	20	N_z	100
W_ϕ	500	W_θ	500	W_z	500

3.9.1 Fault Detection and Signal Reconstruction for Roll Rate Sensor

As the first case study, performance of the proposed method in detection of a roll rate sensor fault and reconstruction of the faulty signal is analyzed in this section. A sine-steer maneuver is performed on a road with combined bank and grade angles. Longitudinal and lateral accelerations of the vehicle during the maneuver are shown in Figure 3.7. The vehicle is first accelerated to a speed of 50kph and then the steering maneuver is performed.

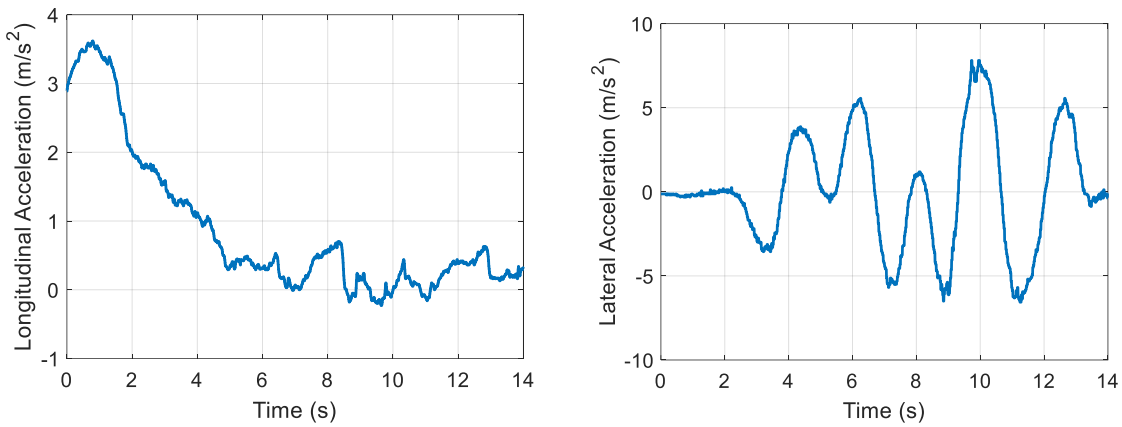

Figure 3.6. Longitudinal and lateral accelerations during the roll rate fault detection test

Variation of the suspension heights and trajectory of the vehicle are shown in Figure 3.7. The vehicle starts on the green dot and finishes the maneuver on the red dot. Bank angle of the road is around 2 degrees at the start and transitions to zero in the middle of the maneuver. Road grade angle is 2 degrees throughout the maneuver.

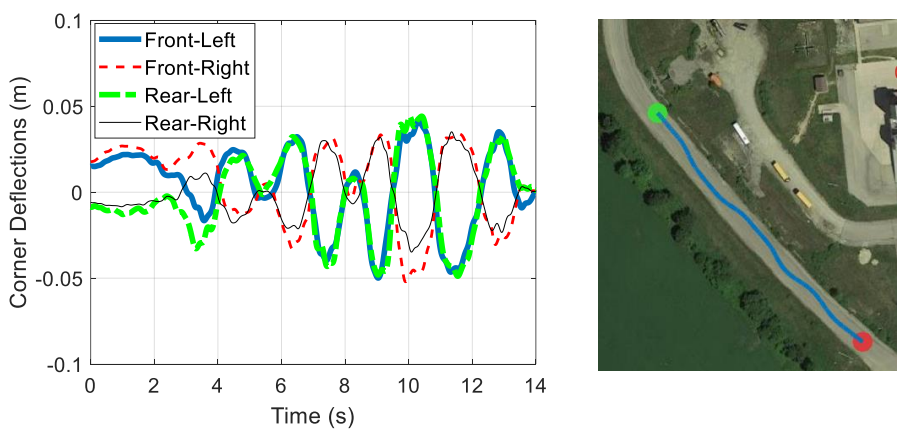

Figure 3.7. Suspension heights and trajectory of the vehicle during the roll rate fault detection test

A roll rate sensor fault is injected at $t = 7s$ by replacing the measured roll rate with a zero signal for the rest of the maneuver. Roll rate residuals are illustrated in Figure 3.8. The residuals are below the adaptive threshold before the fault occurs. Once the fault is injected, $R_{\phi_{-fl}}$, $R_{\phi_{-fr}}$, $R_{\phi_{-rl}}$ and $R_{\phi_{-rr}}$ residuals exceed the thresholds and generate the fault states equal to one for $S_{\phi_{-fl}}$, $S_{\phi_{-fr}}$, $S_{\phi_{-rl}}$, and $S_{\phi_{-rr}}$.

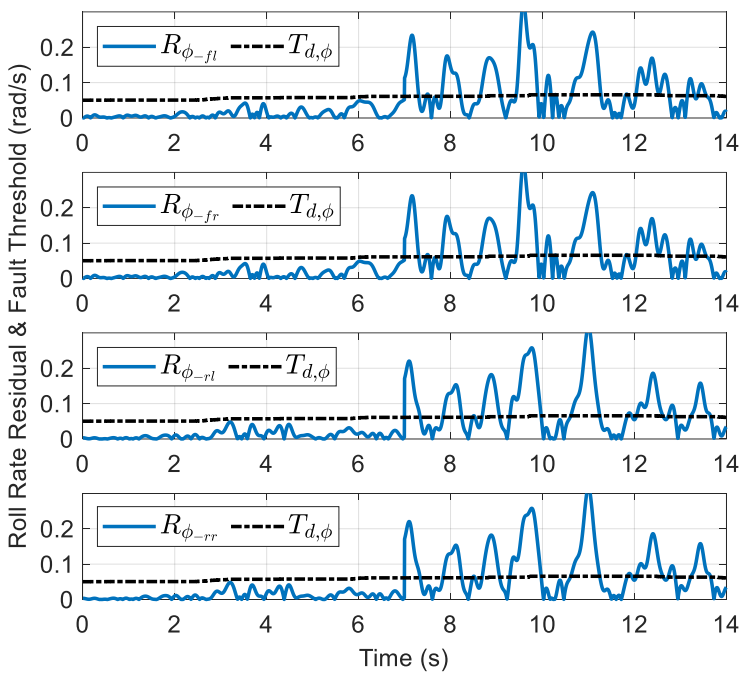

Figure 3.8. Roll rate residuals and fault threshold when the roll rate sensor is faulty

Pitch rate and suspension height residuals are shown in Figure 3.9. Pitch residuals are all below the threshold for the entire maneuver, therefore $S_{\theta_{-fl}}$, $S_{\theta_{-fr}}$, $S_{\theta_{-rl}}$ and $S_{\theta_{-rr}}$ are all zero. Similarly, suspension height residuals are below their respective threshold. Therefore, the suspension fault state residual S_z is zero during the maneuver. These fault states generate the fault signature $[S_z\ S_{\phi_{-fl}}\ S_{\phi_{-fr}}\ S_{\phi_{-rl}}\ S_{\phi_{-rr}}\ S_{\theta_{-fl}}\ S_{\theta_{-fr}}\ S_{\theta_{-rl}}\ S_{\theta_{-rr}}]$=[0 1 1 1 1 0 0 0 0] which corresponds to failure of the roll rate signal according to Table 3.1. The compact fault signature is $[S_{z_{fl}}\ S_{z_{fr}}\ S_{z_{rl}}\ S_{z_{rr}}\ S_{\dot{\phi}}\ S_{\dot{\theta}}] =$ [0 0 0 0 1 0] which indicates failure of the roll rate sensor.

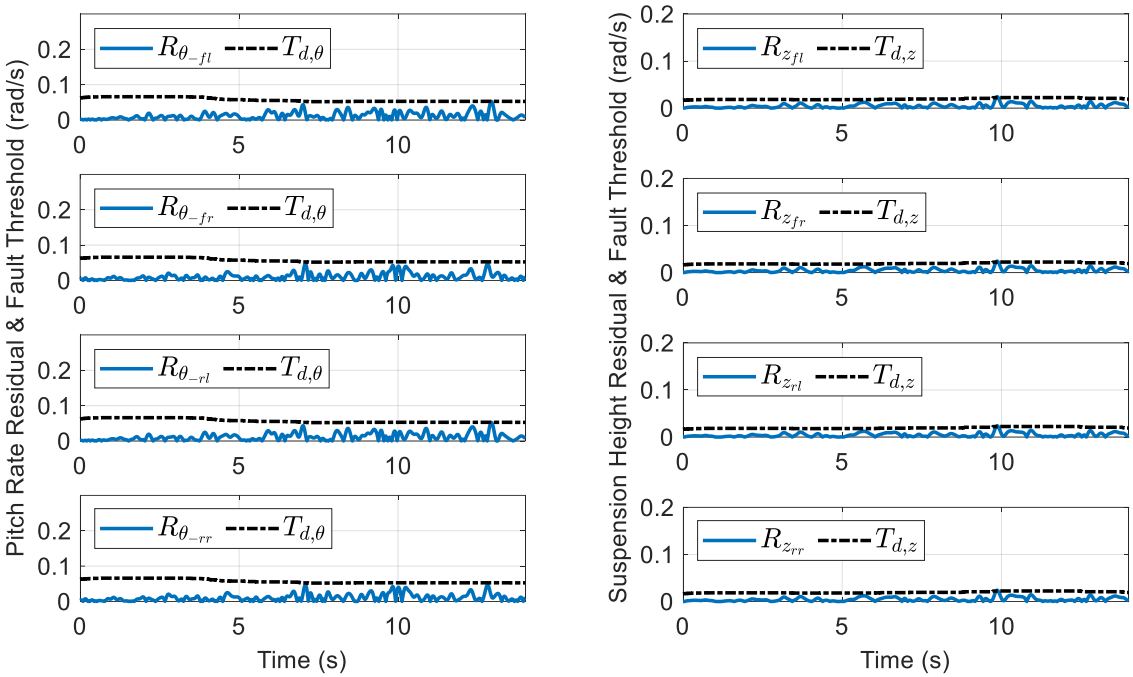

Figure 3.9. Pitch rate and suspension height residuals when the roll rate sensor is faulty

Figure 3.10 shows that the algorithm detects the fault at $t = 7.1s$ and correctly estimates the fault magnitude. The road grade angle and road bank angle are also estimated by the unknown input observers. The result is shown in Figure 3.11.

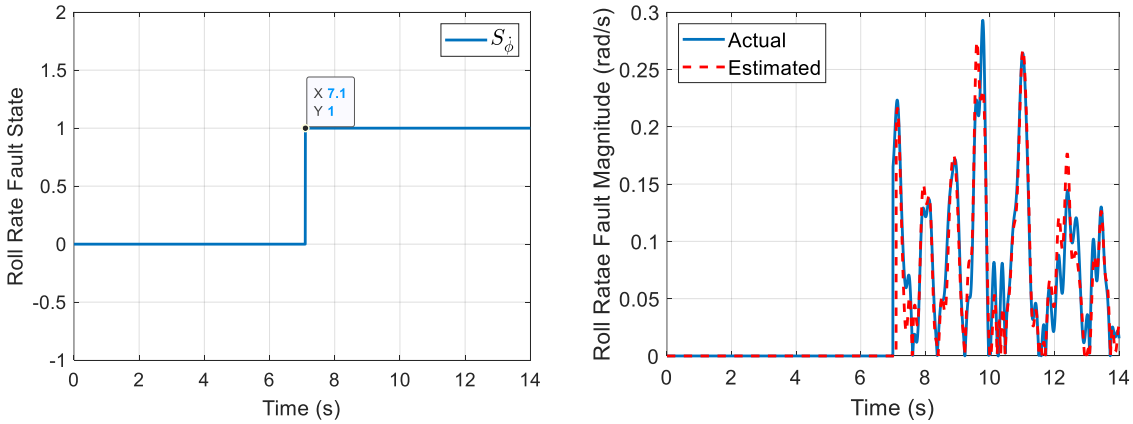

Figure 3.10. Detection of the roll rate sensor fault and estimation of the fault magnitude

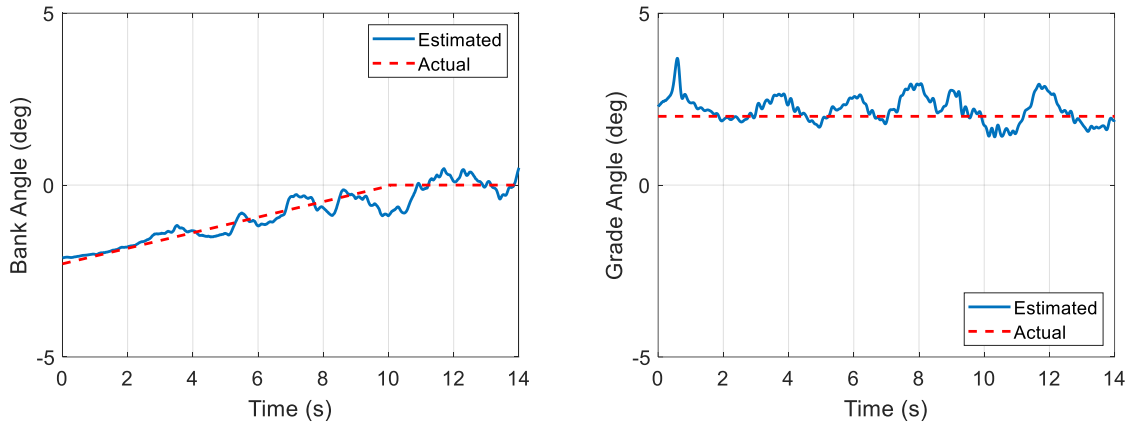

Figure 3.11. Estimation of road grade and bank angles when roll rate sensor is faulty

As soon as the algorithm detects the fault, it starts reconstructing the faulty roll rate signal using the unknown input observers and the estimated states. The reconstructed roll rate is illustrated in Figure 3.12 and is compared to the actual roll rate of the vehicle and the faulty signal.

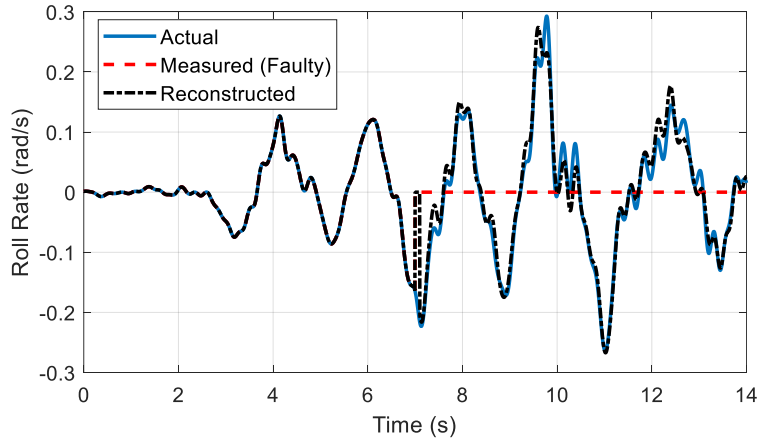

Figure 3.12. Reconstruction of the faulty roll rate signal

The NRMSE of the reconstructed roll rate signal with respect to the actual roll rate of the vehicle is 7.22% in this case study. The results confirm the desirable performance of the proposed method in terms of reliable estimation of the road grade/bank angles, accurate detection of the roll rate fault, and precise reconstruction of the faulty signal.

3.9.2 Fault Detection and Signal Reconstruction for Pitch Rate Sensor

Detection of a bias fault on the pitch rate sensor and reconstruction of the faulty signal is explored in this section. The maneuver involves acceleration and braking on a road with two degrees of grade angle. Longitudinal and lateral accelerations of the vehicle are shown in Figure 3.13. Suspension height measurements and trajectory of the vehicle are illustrated in Figure 3.14.

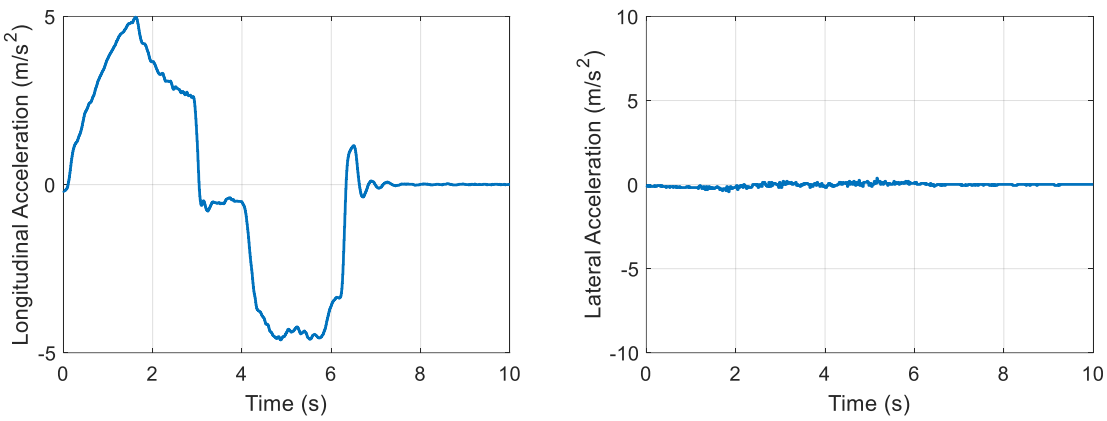

Figure 3.13. Longitudinal and lateral accelerations during the pitch rate fault detection test

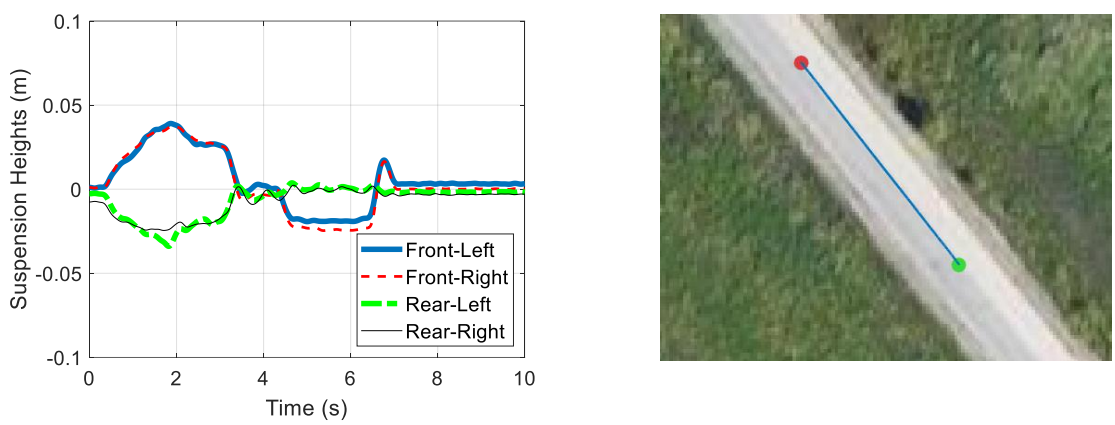

Figure 3.14. Suspension heights and trajectory of the vehicle in the pitch rate fault detection test

The fault in this case study is a bias of $0.1\ \mathrm{rad/s}$ added to the pitch rate signal from the beginning of the maneuver. Figure 3.15 illustrates pitch rate residuals, which are above the thresholds for the entire maneuver. Figure 3.16 shows the roll rate and suspension height residuals which are all below their respective thresholds for the entire maneuver.

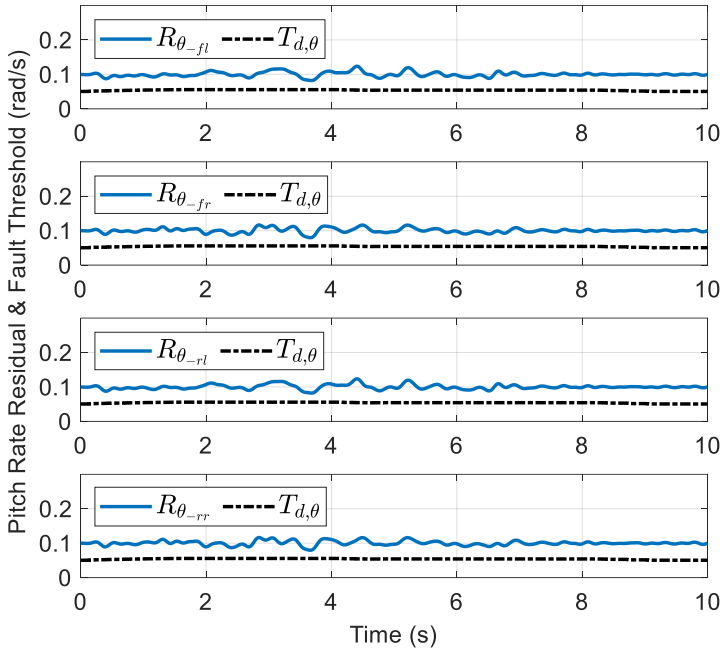

Figure 3.15. Pitch rate residuals when the pitch rate sensor is faulty

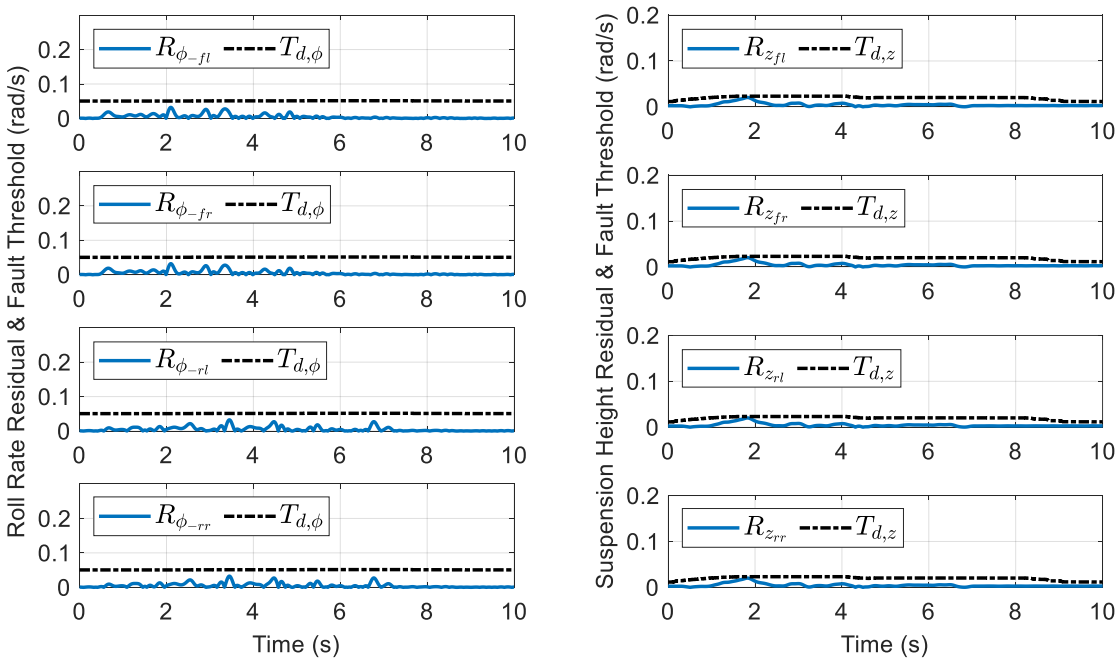

Figure 3.16. Roll rate and suspension height residuals when the pitch rate sensor is faulty

The residuals generate a fault signature of $[S_z\ S_{\phi_{-fl}}\ S_{\phi_{-fr}}\ S_{\phi_{-rl}}\ S_{\phi_{-rr}}\ S_{\theta_{-fl}}\ S_{\theta_{-fr}}\ S_{\theta_{-rl}}\ S_{\theta_{-rr}}]$=[0 0 0 0 0 1 1 1 1] which corresponds to the failure of the pitch rate sensor according to Table 3.1. The compact fault signature is $[S_{z_{fl}}\ S_{z_{fr}}\ S_{z_{rl}}\ S_{z_{rr}}\ S_{\dot{\phi}}\ S_{\dot{\theta}}] = [0\ 0\ 0\ 0\ 0\ 1]$. Figure 3.17 shows that the fault is detected at $t = 0.1$s and the fault magnitude is correctly estimated. The result for estimation of the road grade angle by the observer is shown in Figure 3.18.

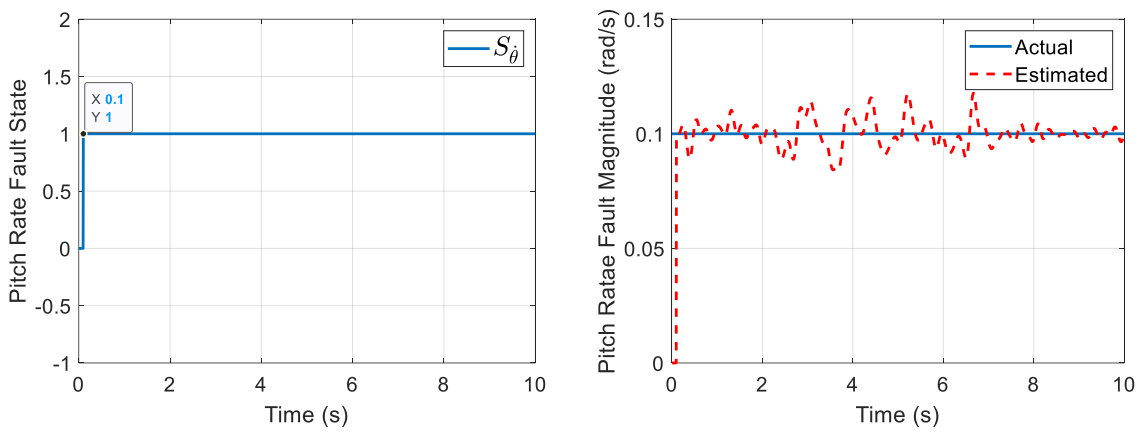

Figure 3.17. Detection of the pitch rate sensor fault and estimation of the fault magnitude

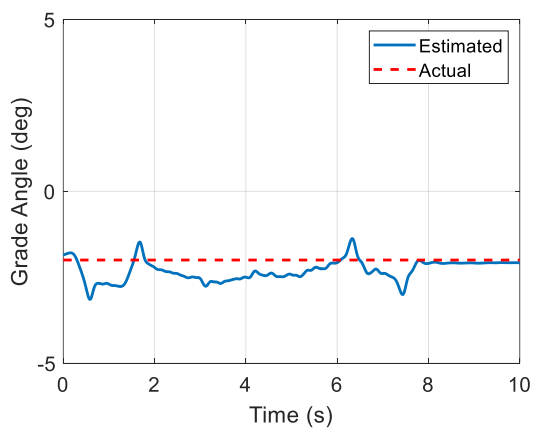

Figure 3.18. Estimation of the road grade when pitch rate sensor is faulty

After detecting the fault, the proposed method reconstructs the faulty pitch rate signal using the observer and the estimated estates. The result is shown in Figure 3.19. Despite the excessive acceleration and the nonlinear longitudinal motion during the maneuver, the proposed method can accurately reconstruct the faulty signal. The NRMSE for reconstruction of the pitch rate signal in this case study is 8.53%.

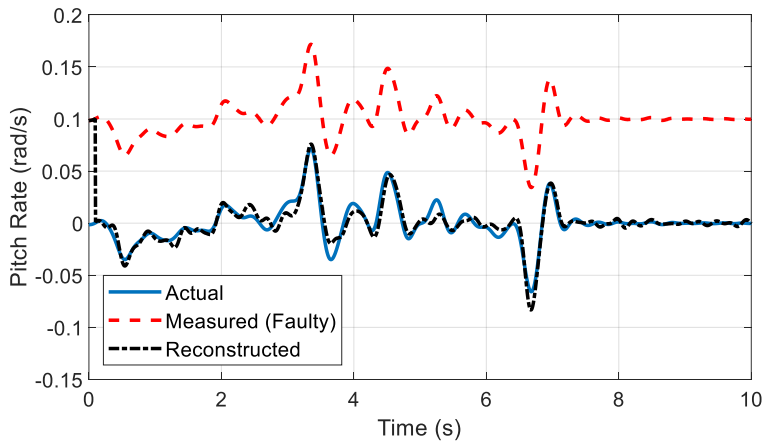

Figure 3.19. Reconstruction of the faulty pitch rate signal

3.9.3 Fault Detection and Signal Reconstruction for Suspension Height Sensor

Detection of a suspension height sensor fault and reconstruction of the faulty signal is discussed in this section. A figure-eight maneuver with a harsh lateral acceleration is performed on a flat road for this case study. Longitudinal and lateral acceleration of the vehicle during the maneuver are shown in Figure 3.20.

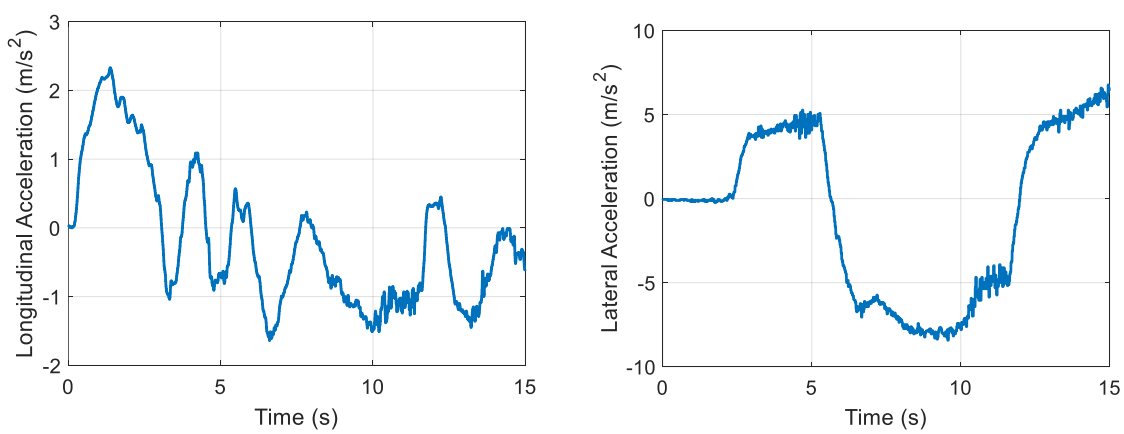

Figure 3.20. Longitudinal and lateral accelerations during the suspension height fault detection test

An actual faulty laser height sensor is installed on the rear-right corner that produces intermittent random faults with no specific patterns during the maneuver. An additional suspension height sensor is also mounted on the rear-right corner to verify the fault detection results. Data from the healthy sensor is not used in the algorithm and is only utilized to verify the results. Therefore, the algorithm receives

healthy signals from the front-left, front-right and rear-left sensors, and a faulty signal from the rear-right sensor as shown in Figure 3.21.

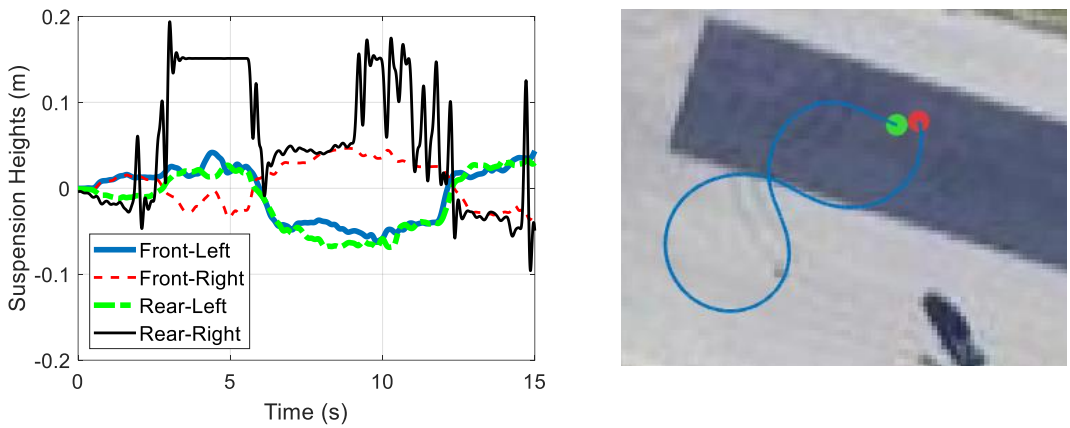

Figure 3.21. Suspension heights and trajectory of the vehicle in the suspension fault detection test

Suspension height residuals are illustrated in Figure 3.22. The results show that all residuals exceed their thresholds at $t = 1.8\ s$ which corresponds to the first instance at which the rear-right sensor produces a large error.

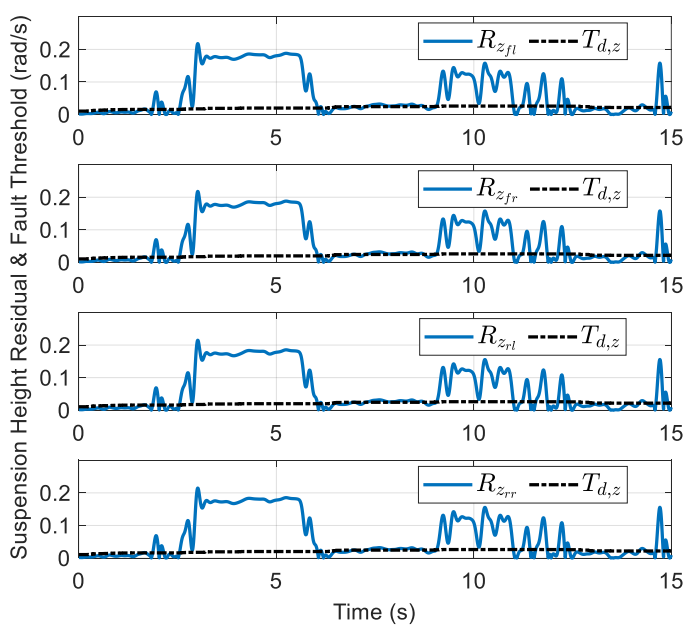

Figure 3.22. Suspension height residuals when the rear-right suspension sensor is faulty

Roll rate and pitch rate residuals are shown in Figure 3.23. Certain roll rate and pitch rate residuals also exceed their threshold during this maneuver. Based on the residuals, the algorithm generates a fault signature of $[S_z\ S_{\phi_{-fl}}\ S_{\phi_{-fr}}\ S_{\phi_{-rl}}\ S_{\phi_{-rr}}\ S_{\theta_{-fl}}\ S_{\theta_{-fr}}\ S_{\theta_{-rl}}\ S_{\theta_{-rr}}]$=[1 1 1 0 0 1 0 1 0] which indicates failure of the rear-right suspension sensor when processed by the decision logic in Table 3.1. The compact fault signature is $[S_{z_{fl}}\ S_{z_{fr}}\ S_{z_{rl}}\ S_{z_{rr}}\ S_{\dot{\phi}}\ S_{\dot{\theta}}] = [0\ 0\ 0\ 1\ 0\ 0]$. The fault is detected at $t = 1.945s$ and the fault magnitude is estimated by the proposed method as shown in Figure 3.24.

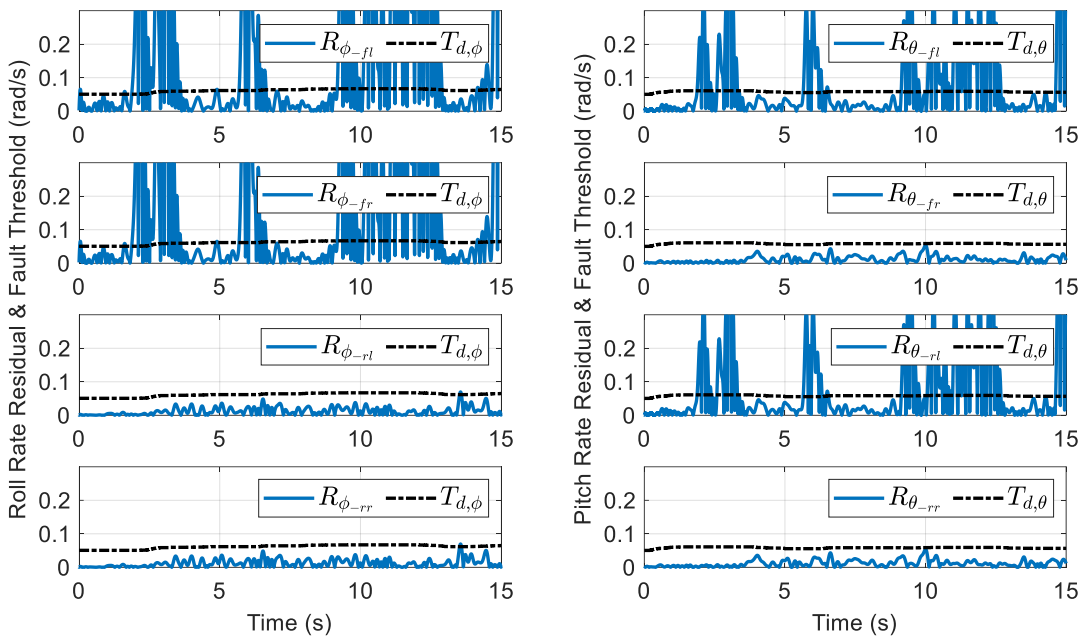

Figure 3.23. Roll rate and pitch rate residuals when the rear-right suspension sensor is faulty

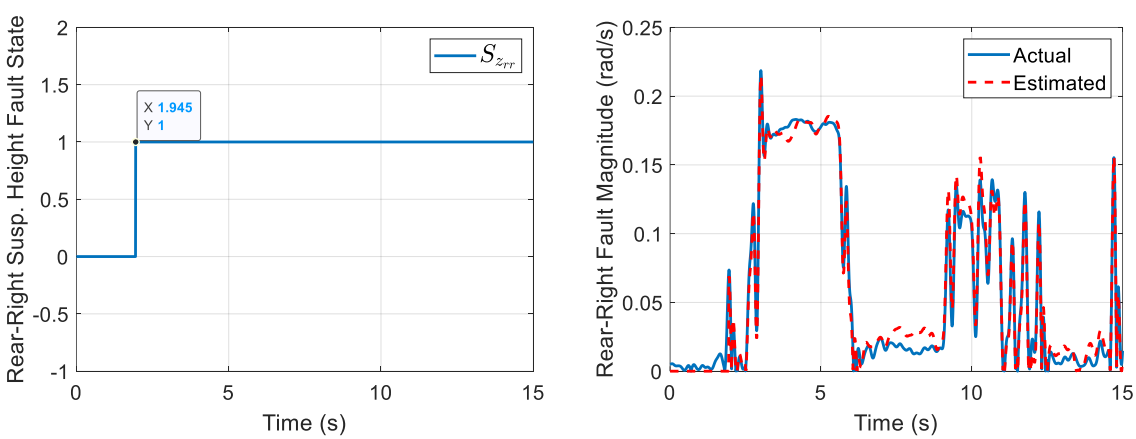

Figure 3.24. Detection of the suspension height sensor fault and estimation of the fault magnitude

After detecting the fault, the algorithm starts reconstructing the failed signal using the healthy sensors. NRMSE of the reconstruction error is 18.24% in this case study. Figure 3.25 compares the faulty signal, the reconstructed signal and the actual suspension height received from the parallel healthy sensor.

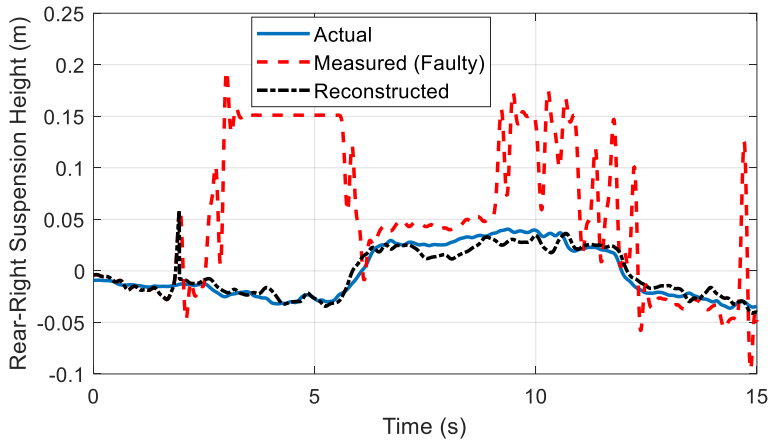

Figure 3.25. Reconstruction of the faulty rear-right suspension height signal

Fault-tolerant estimation of body roll and pitch angles is achieved by using the reconstructed signal as shown in Figure 3.26. Without fault-tolerance, roll and pitch angle estimations are impacted by the faulty sensor and large estimation errors are observed. On the other hand, the fault-tolerant estimation continues to deliver accurate results by switching to the reconstructed signal after the fault is detected.

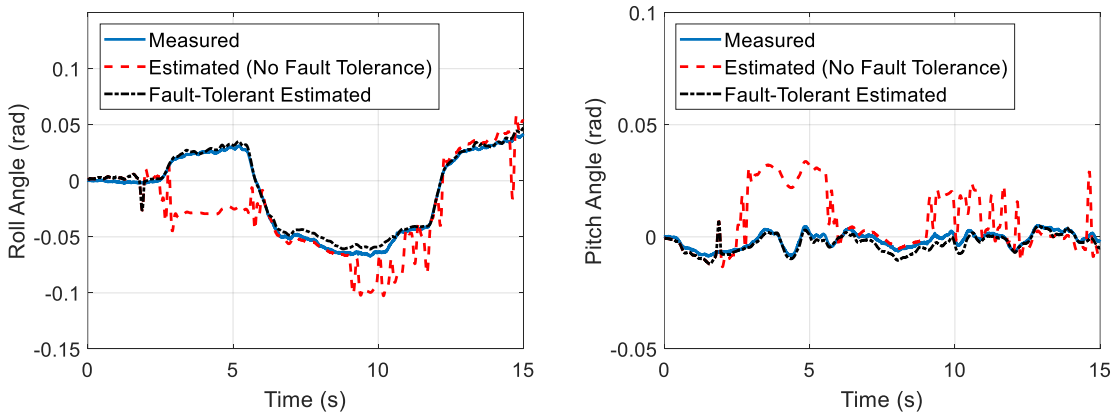

Figure 3.26. Fault-tolerant estimation of roll and pitch angles

3.10 Summary

This chapter presented a structure for detection of roll rate, pitch rate, and suspension height sensor faults and reconstruction of the faulty signals. A method was proposed to generate unique signatures for sensor faults using unknown input observers combined with the vehicle kinematic and dynamic models. Detectability and isolability of the faults by the proposed method was analytically verified using the characteristics of the fault signature matrix. The analytical redundancies and the estimated states from the unknown input observers were used to reconstruct the sensor faults after detection.

Road test experiments were performed on an instrumented vehicle which demonstrated effectiveness of the proposed method in various driving conditions and with different sensor failure scenarios including loss off signal, bias, and random faults. Reliable and fast fault detection, accurate reconstruction of the faulty signal, robustness against road disturbances, and robustness against false positives are among the features of the proposed methodology.

The proposed structure can be integrated with various vehicle control systems such as active suspension and rollover prevention systems to ensure their reliable performance of such systems even in presence of sensor faults.

Chapter 4

Fault Detection and Signal Reconstruction for Accelerations, Yaw Rate and Steering Angle Sensors

This chapter proposes a structure for detection of longitudinal acceleration, lateral acceleration, vertical acceleration, yaw rate, and steering angle sensor faults and reconstruction of faulty signals. Using vehicle kinematic and dynamic models together with the estimated vehicle states, a method is proposed to detect the sensor faults and localize the faulty sensor. After detecting the fault, reconstruction of the faulty sensory signal is achieved by using a random walk observer with adaptive weights. Detectability and isolability of the faults using the proposed approach is verified using properties of the fault signature matrix. Finally, several experimental case studies are conducted to demonstrate the effectiveness of the proposed approach in various driving scenarios.

4.1 Introduction

General structure of the proposed approach is shown in Figure 4.1.

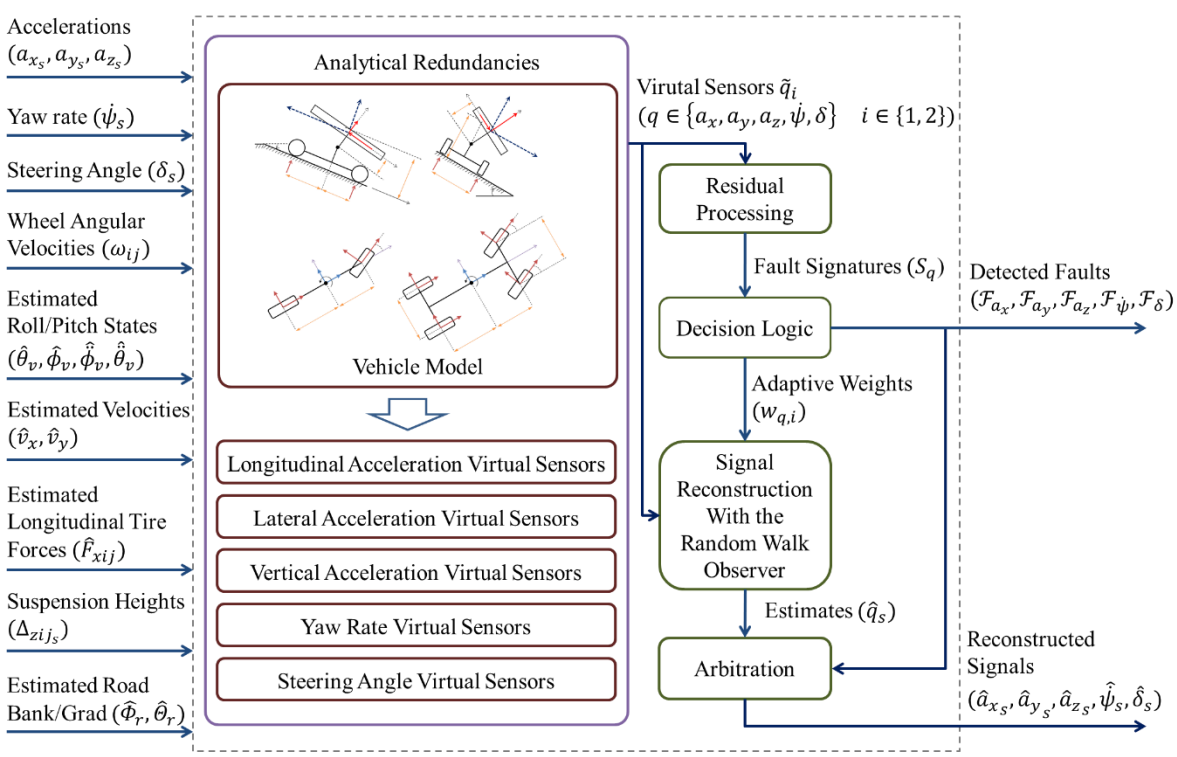

Figure 4.1. Overall structure of the fault detection and signal reconstruction method

This model-based sensor fault detection method is developed based on the idea of virtual sensors. Virtual sensor, which is a mathematically estimated expected value for a sensor measurement, is calculated using the vehicle model, estimated vehicle states, analytical redundancy relations and the other vehicle sensors. When there is no fault in the system, the virtual and actual sensor should deliver similar measurements assuming that the model and estimations are sufficiently accurate. Therefore, the difference between measurements delivered by the virtual and actual sensors falls below a certain threshold. The thresholds are designed to adapt with respect to vehicle excitations and to facilitate a faster and a more reliable fault detection. The residual processor monitors the sensors and detects the sensor faults when there is a significant difference between the actual and virtual sensors. Consequently, the residual processor provides fault signatures to the decision logic to localize the fault. After detecting a fault, the algorithm reconstructs the failed signal using virtual sensor values and a random walk observer with adaptive weights. These weights manage contribution of each virtual sensor in reconstruction of the faulty sensory signal. Finally, the algorithm arbitrates between the healthy and reconstructed sensory signals and outputs the fault-free data to the other estimation or control modules in the vehicle.

4.2 Vehicle Model

The fault detection, signal reconstruction and fault-tolerant estimation algorithms in this chapter are developed using a vehicle model shown in Figure 4.2 [97]. This model covers the major states of vehicle dynamics that are important in vehicle stability and control applications. Using the pitch plane model in Figure 4.2-(a), vertical tire forces on the front and rear axles, F_{zFt} and F_{zRr}, can be calculated as:

$$F_{zFt} = F_{zfl} + F_{zfr} = -m\frac{H_{CG}-H_{PC}(1-cos(\theta_v))}{L_f+L_r}\left[a_{x_s}cos(\theta_v) - a_{z_s}\,sin(\theta_v)\right] - m\frac{L_r+H_{PC}\sin(\theta_v)}{L_f+L_r}\left[a_{x_s}\,sin(\theta_v) + a_{z_s}\,cos(\theta_v)\right] \tag{4-1}$$

$$F_{zRr} = F_{zrl} + F_{zrr} = -m\frac{H_{CG}-H_{PC}[1-cos(\theta_v)]}{L_f+L_r}\left[a_{x_s}\,cos(\theta_v) - a_{z_s}\,sin(\theta_v)\right] + m\frac{L_f-H_{PC}sin\,(\theta_v)}{L_f+L_r}\left[a_{x_s}\,sin(\theta_v) + a_{z_s}\,cos(\theta_v)\right] \tag{4-2}$$

where a_{x_s}, a_{y_s} and a_{z_s} are the acceleration measurements from the sensors in the longitudinal, lateral and vertical directions, respectively, and F_{zij} represents the individual vertical tire forces for each wheel.

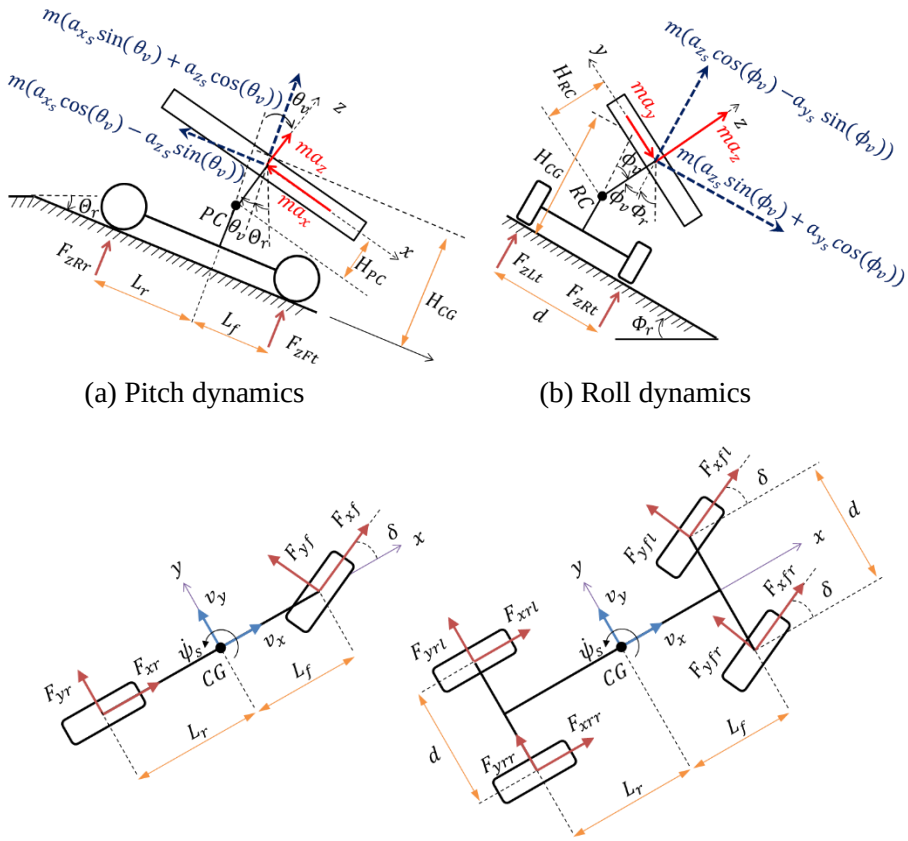

(a) Pitch dynamics (b) Roll dynamics

(c) Single-track dynamics (d) Double-track dynamics

Figure 4.2. Vehicle model

Effects of the vertical forces can be considered as a virtual mass added on the front and rear axles (m_{Ft} and m_{Rr}, respectively) [97]:

$$m_{Ft} = \frac{F_{zFt}}{a_{z_s}} \tag{4-3}$$

$$m_{Rr} = \frac{F_{zRr}}{a_{z_s}} \tag{4-4}$$

Using these virtual masses together with the roll plane model in Figure 4.2-(b) and Equations (4-1)-(4-4), the vertical force on the front-left tire can be calculated by taking the moments about the front-right tire contact point:

$$F_{z_{fl}} = -m_{Ft}\frac{\frac{d}{2} - H_{RC}\sin(\phi_v)}{d}\left[a_{z_s}\cos(\phi_v) - a_{y_s}\sin(\phi_v)\right] - m_{Ft}\frac{H_{CG} - H_{RC}(1-\cos(\phi_v))}{d}\left[a_{z_s}\sin(\phi_v) + a_{y_s}\cos(\phi_v)\right] \tag{4-5}$$

Similarly, vertical forces acting on the other tires are calculated as:

$$F_{z_{fr}} = -m_{Ft}\frac{\frac{d}{2}+H_{RC}\,sin(\phi_v)}{d}\left[a_{z_s}\,cos(\phi_v) - a_{y_s}\,sin(\phi_v)\right] + m_{Ft}\frac{H_{CG}-H_{RC}[1-cos(\phi_v)]}{d}\left[a_{z_s}\,sin(\phi_v) + a_{y_s}\,cos(\phi_v)\right] \tag{4-6}$$

$$F_{z_{rl}} = -m_{Rr}\frac{\frac{d}{2}-H_{RC}\,sin(\phi_v)}{d}\left[a_{z_s}\,cos(\phi_v) - a_{y_s}\,sin(\phi_v)\right] - m_{Rr}\frac{H_{CG}-H_{RC}(1-cos(\phi_v))}{d}\left[a_{z_s}\,sin(\phi_v) + a_{y_s}\,cos(\phi_v)\right] \tag{4-7}$$

$$F_{z_{rr}} = -m_{Rr}\frac{\frac{d}{2}+H_{RC}\,sin(\phi_v)}{d}\left[a_{z_s}\,cos(\phi_v) - a_{y_s}\,sin(\phi_v)\right] + m_{Rr}\frac{H_{CG}-H_{RC}[1-cos(\phi_v)]}{d}\left[a_{z_s}\,sin(\phi_v) + a_{y_s}\,cos(\phi_v)\right] \tag{4-8}$$

Using the single-track model in Figure 4.2-(c), longitudinal, lateral and yaw dynamics can be expressed as:

$$a_x = \frac{1}{m}\left(F_{xf}\,cos(\delta) + F_{xr} - F_{yf}\,sin\,(\delta)\right) \tag{4-9}$$

$$a_y = \frac{1}{m}\left(F_{yr} + F_{yf}\,cos(\delta) + F_{xf}\,sin(\delta)\right) \tag{4-10}$$

$$\ddot{\psi} = \frac{1}{I_z}\left(\left(F_{yf}\,cos(\delta) + F_{xf}\,sin(\delta)\right)L_f - F_{yr}\,L_r\right) \tag{4-11}$$

Where m is the vehicle mass, I_z is the yaw moment of inertia, $\dot{\psi}$ is the yaw rate, δ is the steering angle, and:

$$F_{xf} = F_{xfl} + F_{xfr} \tag{4-12}$$

$$F_{xr} = F_{xrl} + F_{xrr} \tag{4-13}$$

$$F_{yf} = F_{yfl} + F_{yfr} \tag{4-14}$$

$$F_{yr} = F_{yrl} + F_{yrr} \tag{4-15}$$

The vehicle model will be used in the next sections to generate multiple analytical redundancy relations for each sensor and enable detection, isolation and reconstruction of faulty sensory signals.

4.3 Analytical Redundancy Relations for Lateral Acceleration Sensor

Sensor measurement for the lateral acceleration of the vehicle is a function of vehicle kinematic states:

$$a_y = \dot{v}_y + v_x\dot{\psi} + gsin(\phi_v + \Phi_r) \tag{4-16}$$

where $\dot{v}_y$ is the acceleration component due to the lateral slip, $v_x\dot{\psi}$ is the acceleration component due to the vehicle yaw motion and $gsin(\phi_v + \Phi_r)$ is the acceleration due to the vehicle roll and road bank angles. In general, $\dot{v}_y$ is considerably smaller than the other terms in (4-16) [70]. Therefore, the vehicle lateral acceleration can be approximated as:

$$a_y \cong v_x\dot{\psi} + gsin(\phi_v + \Phi_r) \tag{4-17}$$

In (4-17), longitudinal velocity of the vehicle is needed and can be approximated using the wheel angular velocities (ω_{ij}) and the tire effective radius (r_e):

$$v_x(\omega_{ij}, \delta) \cong \left(\frac{\omega_{rr}+\omega_{fl}}{2} r_e\right) \cong \left(\frac{\omega_{fr}+\omega_{fl}}{2} r_e\right) cos(\delta) \cong \frac{1}{2}\left[\left(\frac{\omega_{rr}+\omega_{fl}}{2} r_e\right) + \left(\frac{\omega_{fr}+\omega_{fl}}{2} r_e\right) cos(\delta)\right] \tag{4-18}$$

or using an observer to account for any uncertainties and improve the accuracy [92]. The observer is constructed as:

$$\dot{\hat{v}}_x = a_x - gsin(\hat{\theta}_v + \hat{\Theta}_r) + \sum K_{v_x}(a_x, \omega_{ij})(v_{x_{CG\leftarrow ij}} - \hat{v}_x) \tag{4-19}$$

where $v_{x_{CG\leftarrow ij}}$ represents the CG velocity when this velocity is derived from the ij corner. These velocities are calculated using the yaw rate, wheel angular velocities and the double track model in Figure 4.2-(d):

$$v_{x_{CG\leftarrow fl}} = r_e\omega_{fl}\cos(\delta) + \dot{\psi}\frac{d}{2} \tag{4-20}$$

$$v_{x_{CG\leftarrow fr}} = r_e\omega_{fr}\cos(\delta) - \dot{\psi}\frac{d}{2} \tag{4-21}$$

$$v_{x_{CG\leftarrow rl}} = r_e\omega_{rl} + \dot{\psi}\frac{d}{2} \tag{4-22}$$

$$v_{x_{CG\leftarrow rr}} = r_e\omega_{rr} - \dot{\psi}\frac{d}{2} \tag{4-23}$$

In (4-19), $K_{v_x}(a_x, \omega_{ij})$ is the observer gain which also determines contribution of each wheel in estimation of the longitudinal velocity based on the wheel slip conditions. Selecting the best wheel for estimation of the longitudinal velocity is well documented in the literature [91][98]. Proof of stability and convergence of the observer is given in [99] for both zero and non-zero slip conditions. In this thesis, the observer (4-19) is implemented using a Kalman filter [100]. The Kalman gain $K_{v_x}(a_x, \omega_{ij})$ is modified based on the wheel slip conditions such that when there is no wheel slip, all wheels have

similar effects in the estimation process. For example, if the front-left wheel is locked or is excessively spinning, $K_{v_x}(a_x, \omega_{fl})$ is set to a small value and consequently the front-left wheel does not contribute to the estimation process.

Using the estimated $\hat{v}_x$ and Equation (4-17), the first analytical redundancy relation for the lateral acceleration signal is formulated as:

$$\tilde{a}_{y_1} = \hat{v}_x \dot{\psi} + g sin(\hat{\phi}_v + \hat{\Phi}_r) \tag{4-24}$$

where $\hat{\phi}_v$ and $\hat{\phi}_r$ were estimated in the previous chapter. Functionally, $\tilde{a}_{y_1}$ can be considered as a virtual lateral acceleration sensor. Although the difference between this virtual sensor and the actual lateral acceleration measurement can indicate presence of a fault, a single virtual sensor is not sufficient to locate the faulty sensor (e.g., to determine if the lateral acceleration sensor is faulty or the yaw rate signal used in (4-24) is faulty and causes the mismatch). Therefore, a second virtual sensor is needed to generate additional information for localizing the fault.

To design the second virtual lateral acceleration sensor, an approximate for the yaw rate is found using Equations (4-20) and (4-21):

$$\dot{\psi} \cong \left(\frac{\omega_{fr} - \omega_{fl}}{d} r_e\right) cos(\delta) \tag{4-25}$$

From Equations (4-17), (4-18) and (4-25), the second virtual lateral acceleration sensor is formulated as:

$$\tilde{a}_{y_2} = \frac{1}{2}\left[\left(\frac{\omega_{rr} + \omega_{rl}}{2} r_e\right) + \left(\frac{\omega_{fr} + \omega_{fl}}{2} r_e\right) cos(\delta)\right]\left(\frac{\omega_{fr} - \omega_{fl}}{d} r_e\right) cos(\delta) + g sin(\hat{\phi}_v + \hat{\Phi}_r) \tag{4-26}$$

Using the two virtual sensors (4-24) and (4-26), an estimate for the lateral acceleration of the vehicle without using the lateral acceleration sensor is defined as:

$$\hat{a}_{y_s} = \left(w_{a_y,1} \tilde{a}_{y_1} + w_{a_y,2} \tilde{a}_{y_2}\right) \tag{4-27}$$

where $\hat{a}_y$ is the estimated lateral acceleration for the sensor. The weight factors $w_{a_y,1}$ and $w_{a_y,2}$ are automatically tuned based on the wheel slip conditions and using a distribution function:

$$\begin{cases} w_{a_y,1} = 1 - w_{a_y,2} \\ w_{a_y,2} = \frac{1}{2} e^{-\frac{\left(100 \max\left(|\lambda_{fj}|, |\lambda_{rj}|\right)\right)^2}{2\sigma^2}} \end{cases} \tag{4-28}$$

where σ is a constant parameter and λ_{ij} is an approximated slip ratio:

$$\begin{cases} \lambda_{fj} = \frac{r_e\omega_{fj}\cos(\delta)-\hat{v}_x}{\max(r_e\omega_{fj}\cos(\delta),\hat{v}_x)} & \text{front wheels} \\ \lambda_{rj} = \frac{r_e\omega_{rj}-\hat{v}_x}{\max(r_e\omega_{rj}-\hat{v}_x)} & \text{rear wheels} \end{cases} \tag{4-29}$$

These adaptive weights help to improve the accuracy of the estimated lateral acceleration in nonlinear driving conditions. Additionally, in case that the longitudinal acceleration or yaw rate sensor is diagnosed as faulty (which will be discussed in the next sections), the first virtual sensor $\tilde{a}_{y_1}$ is no longer reliable. Therefore, $\tilde{a}_{y_1}$ should be eliminated from the fault detection and signal reconstruction process. The residual processor executes this elimination by setting $w_{a_{y,1}}$ to zero and $w_{a_{y,2}}$ to one.

4.4 Analytical Redundancy Relations for Longitudinal Acceleration Sensor

The first virtual sensor for the longitudinal acceleration of the vehicle is designed using the single-track vehicle model in Figure 4.2-(d). Lateral force on the rear track (F_{yr}) is found from (4-10):

$$F_{yr} = ma_y - F_{yf}\cos(\delta) - F_{xf}\sin(\delta) \tag{4-30}$$

By replacing the calculated F_{yr} in (4-11) and simplifying, lateral tire force on the front track is expressed as:

$$F_{yf} = \frac{ma_yL_r+I_z\ddot{\psi}-F_{xf}(L_f+L_r)\sin(\delta)}{(L_f+L_r)\cos(\delta)} \tag{4-31}$$

Using Equations (4-9), (4-12), (4-13) and (4-31), longitudinal acceleration of the vehicle can be expressed as a function of the yaw rate, lateral acceleration and longitudinal tire forces:

$$a_x = \frac{1}{m}\left((F_{xfl}+F_{xfr})\cos(\delta) + (F_{xrl}+F_{xrr}) - \frac{ma_yL_r+I_z\ddot{\psi}-(F_{xfl}+F_{xfr})(L_f+L_r)\sin(\delta)}{(L_f+L_r)\cos(\delta)}\sin(\delta)\right) \tag{4-32}$$

An approach for estimation of the longitudinal tire force for each wheel will be discussed in the next chapter. Assuming that accurate estimations of longitudinal tire forces are available, the first virtual sensor for longitudinal acceleration of the vehicle is defined as:

$$\tilde{a}_{x_1} = \frac{1}{m}\left((\hat{F}_{xfl}+\hat{F}_{xfr})\cos(\delta) + (\hat{F}_{xrl}+\hat{F}_{xrr}) - \frac{ma_yL_r+I_z\ddot{\psi}-(\hat{F}_{xfl}+\hat{F}_{xfr})(L_f+L_r)\sin(\delta)}{(L_f+L_r)\cos(\delta)}\sin(\delta)\right) \tag{4-33}$$

where $\hat{F}_{xij}$ are the estimated longitudinal tire forces.

To design the second virtual sensor, kinematic description of the longitudinal acceleration is considered:

$$a_x = \dot{v}_x - v_y r + gsin(\hat{\theta}_v + \hat{\Theta}_r) \tag{4-34}$$

Assuming that v_y is significantly smaller than the other terms in Equation (4-34), the longitudinal acceleration can be approximated as:

$$\tilde{a}_{x_2} = \dot{\hat{v}}_x + gsin(\hat{\theta}_v + \hat{\Theta}_r) \tag{4-35}$$

where $\hat{\theta}_v$ and $\hat{\Theta}_r$ are available from the previous chapter, and $\dot{\hat{v}}_x$ is obtained using the following observer:

$$\dot{\hat{v}}_x = \frac{\sum \hat{F}_{xij} \cos(\delta)}{m} - gsin(\hat{\theta}_v + \hat{\Theta}_r) + \sum K_{ax}\left(\frac{\sum \hat{F}_{xij} \cos(\delta)}{m}, \omega_{ij}\right)(r_e \omega_{ij} \cos(\delta) - \hat{v}_x) \tag{4-36}$$

where the observer gain $K_{a_x}(\frac{\sum \hat{F}_{xij} \cos(\delta_{ij})}{m}, \omega_{ij})$ determines contribution of each wheel in estimation of the longitudinal acceleration depending upon the wheel slip conditions.

Using the two virtual sensors given by (4-33) and (4-35), longitudinal acceleration of the vehicle can be estimated as:

$$\hat{a}_{x_s} = \left(w_{a_x,1}\tilde{a}_{x_1} + w_{a_x,2}\tilde{a}_{x_2}\right) \tag{4-37}$$

where weights. $w_{a_x,1}$ and $w_{a_x,2}$ are designed similar to Equations (4-28) and (4-29). In case that the lateral acceleration or yaw rate sensor is diagnosed as faulty, the first virtual sensor is not reliable and is eliminated by the residual processor, $w_{a_x,1}$ is set to zero and $w_{a_x,2}$ is set to one.

4.5 Analytical Redundancy Relations for Vertical Acceleration Sensor

From the kinematic model in Figure 3.2, vertical position of the CG can be found from the corner positions:

$$\Delta z_{CG} = \Delta z_{ij} + L_{ij}\theta_v + \frac{d_{ij}}{2}\phi_v \tag{4-38}$$

where Δz_{CG} is the vertical displacement of CG. Coefficients L_{ij} and d_{ij} for each corner are defined as:

$$L_{fl} = L_{fr} = L_f \tag{4-39}$$

$$L_{rl} = L_{rr} = -L_r \tag{4-40}$$

$$d_{fl} = d_{rl} = \frac{d}{2} \tag{4-41}$$

$$d_{fr} = d_{rr} = -\frac{d}{2} \tag{4-42}$$

Consequently, vertical acceleration of the CG relative to the corners can be expressed as:

$$a_{z_{CG}} = \ddot{\Delta z}_{ij} + L_{ij}\ddot{\theta}_v + \frac{d_{ij}}{2}\ddot{\phi}_v \tag{4-43}$$

Considering that fault-tolerant estimations for the corner suspension sensors and roll/pitch sensors are available from the method presented in Chapter 3, the first virtual sensors for the vertical acceleration is defined as:

$$\tilde{a}_{z_1} = \widehat{\ddot{\Delta z}}_{ij} + L_{ij}\hat{\ddot{\theta}}_v + \frac{d_{ij}}{2}\hat{\ddot{\phi}}_v \qquad ij \in \{fl, fr, rl, rr\} \tag{4-44}$$

The second virtual sensor for vertical acceleration is found using the estimated vertical forces. In (4-5)-(4-8), the vertical acceleration is replaced by a constant gravity to make the force approximation independent of the vertical sensor measurement. Consequently, the approximated virtual sensor can be expressed as:

$$\tilde{a}_{z_2} = \frac{1}{m}\sum \hat{F}_{zij} \qquad ij \in \{fl, fr, rl, rr\} \tag{4-45}$$

Using the two virtual sensors given in Equations (4-44)-(4-45), vertical acceleration of the vehicle is estimated as:

$$\hat{a}_{z_s} = \left(w_{a_z,1}\tilde{a}_{z_1} + w_{a_z,2}\tilde{a}_{x_2}\right) \tag{4-46}$$

The weights $w_{a_z,1}$ and $w_{a_z,2}$ are tuned by the residual processing unit similar to the previous cases.

4.6 Analytical Redundancy Relations for Yaw Rate Sensor

The first yaw rate virtual sensor $\tilde{\dot{\psi}}_1$ is formulated using Equation (4-17):

$$\tilde{\dot{\psi}}_1 = \begin{cases} \frac{a_y - g\sin(\hat{\phi}_v + \hat{\Phi}_r)}{\hat{v}_x} & \hat{v}_{x_2} \geq v_0 \\ \left(\frac{\omega_{rr} - \omega_{rl}}{d} r_e\right) & \hat{v}_{x_2} < v_0 \end{cases} \tag{4-47}$$

For lower speeds ($\hat{v}_x < v_0$ where v_0 is a sufficiently low speed), the yaw rate is approximated using the difference between the rear-left and rear-right wheel speeds to prevent a division by zero. In (4-47), $\hat{v}_x$ is the estimated longitudinal velocity as described in the previous section. The only difference is that

in Equations (4-20)-(4-23), $\dot{\psi}$ is replaced with the following equations to make the velocity estimation independent from the yaw rate:

$$v_{v_{x_{CG\leftarrow fl}}} = r_e\omega_{fl}\cos(\delta) + \left(\frac{\omega_{rr}-\omega_{rl}}{2}r_e\right) \tag{4-48}$$

$$v_{v_{x_{CG\leftarrow fr}}} = r_e\omega_{fr}\cos(\delta) - \left(\frac{\omega_{rr}-\omega_{rl}}{2}r_e\right) \tag{4-49}$$

$$v_{v_{x_{CG\leftarrow rl}}} = r_e\omega_{rl} + \left(\frac{\omega_{rr}-\omega_{rl}}{2}r_e\right) \tag{4-50}$$

$$v_{v_{x_{CG\leftarrow rr}}} = r_e\omega_{rr} - \left(\frac{\omega_{rr}-\omega_{rl}}{2}r_e\right) \tag{4-51}$$

The second yaw rate virtual sensor is designed using (4-25):

$$\tilde{\dot{\psi}}_2 = \left[\left(\frac{\omega_{fr}-\omega_{fl}}{d}r_e\right)cos(\delta)\right] \tag{4-52}$$

Subsequently, an estimate for the sensory yaw rate ($\hat{\dot{\psi}}_s$) is obtained using the two virtual sensors given in Equations (4-47) and (4-52):

$$\hat{\dot{\psi}}_s = \left(w_{\dot{\psi},1}\,\tilde{\dot{\psi}}_1 + w_{\dot{\psi},2}\,\tilde{\dot{\psi}}_2\right) \tag{4-53}$$

where the weights $w_{\dot{\psi},1}$ and $w_{\dot{\psi},2}$ are designed similar to Equations (4-28)-(4-29). In case that the lateral acceleration or longitudinal acceleration sensor is diagnosed as faulty, the first virtual sensor $\tilde{\dot{\psi}}_1$ is no longer reliable and should be eliminated from the fault detection and signal reconstruction process. In such a scenario, $w_{\dot{\psi},1}$ is set to zero and $w_{\dot{\psi},2}$ is set to one by the residual processor.

4.7 Analytical Redundancy Relations for Steering Angle Sensor

The first virtual sensor for the steering angle can be obtained from (4-32). Defining C_1, C_2, C_3 and C_4 coefficients as follows and re-writing Equation (4-32) using the C_i coefficients give:

$$C_1 = ma_x - (F_{xrl} + F_{xrr}) \tag{4-54}$$

$$C_2 = F_{xfl} + F_{xfr} \tag{4-55}$$

$$C_3 = \frac{ma_yL_r + I_z\ddot{\psi}}{L_f + L_r} \tag{4-56}$$

$$C_1 = C_2\cos(\delta) - C_3\tan(\delta) + C_2\tan(\delta)\sin(\delta) \tag{4-57}$$

The numerical solution of (4-57) can be used as the first virtual sensor for the steering angle ($\tilde{\delta}_1$). Finding this real-time numerical solution in onboard processing units with constrained resources might pose practical challenges. As an alternative, the virtual sensor can be obtained from a steady state handling dynamic model [101]:

$$\tilde{\delta}_1 = \left(\frac{2}{v_{x_{CG\leftarrow rl}}+v_{x_{CG\leftarrow rr}}}\right)^2 a_y \left[(L_f + L_r) + K_{us}\left(\frac{v_{x_{CG\leftarrow rl}}+v_{x_{CG\leftarrow rr}}}{2}\right)^2\right] \tag{4-58}$$

where K_{us} is the understeer coefficient of the vehicle.

Similarly, the second virtual sensor for the steering angle is defined as:

$$\tilde{\delta}_2 = \frac{2}{v_{x_{CG\leftarrow rl}}+v_{x_{CG\leftarrow rr}}}\dot{\psi}\left[(L_f + L_r) + K_{us}\left(\frac{v_{x_{CG\leftarrow rl}}+v_{x_{CG\leftarrow rr}}}{2}\right)^2\right] \tag{4-59}$$

The estimated steering angle of the vehicle using the two virtual sensors is defined as:

$$\hat{\delta}_s = \left(w_{\delta,1}\tilde{\delta}_1 + w_{\delta,2}\tilde{\delta}_2\right) \tag{4-60}$$

If the yaw rate sensor is faulty, then the second residual is no longer reliable. Therefore, the residual processor sets $w_{\delta,2}$ to zero and $w_{\delta,1}$ to one to solely rely on the first virtual sensor. Similarly, if the lateral acceleration sensor is faulty, $w_{\delta,1}$ is set to one and $w_{\delta,2}$ is set to zero to solely rely on the first virtual sensor. At very low speeds, where there is no correlation between the steering angle of the vehicle and other vehicle states, both weights are set to zero and the fault detection process is paused for the steering angle sensor to avoid false positives. An example for this scenario is when the vehicle is stationary. In this scenario the steering wheel can be rotated without generating any lateral acceleration and yaw rate.

4.8 Detection and Isolation of Sensor Faults

The flowchart illustrated in Figure 4.3 explains the fault detection and signal reconstruction process using the virtual sensors. This process generates residuals, detects faults using a decision logic, reconstructs the failed signal in an adaptive estimator and arbitrates between the healthy sensor data or the reconstructed signals when a fault is detected. A detailed description of the process is presented in the next sections.

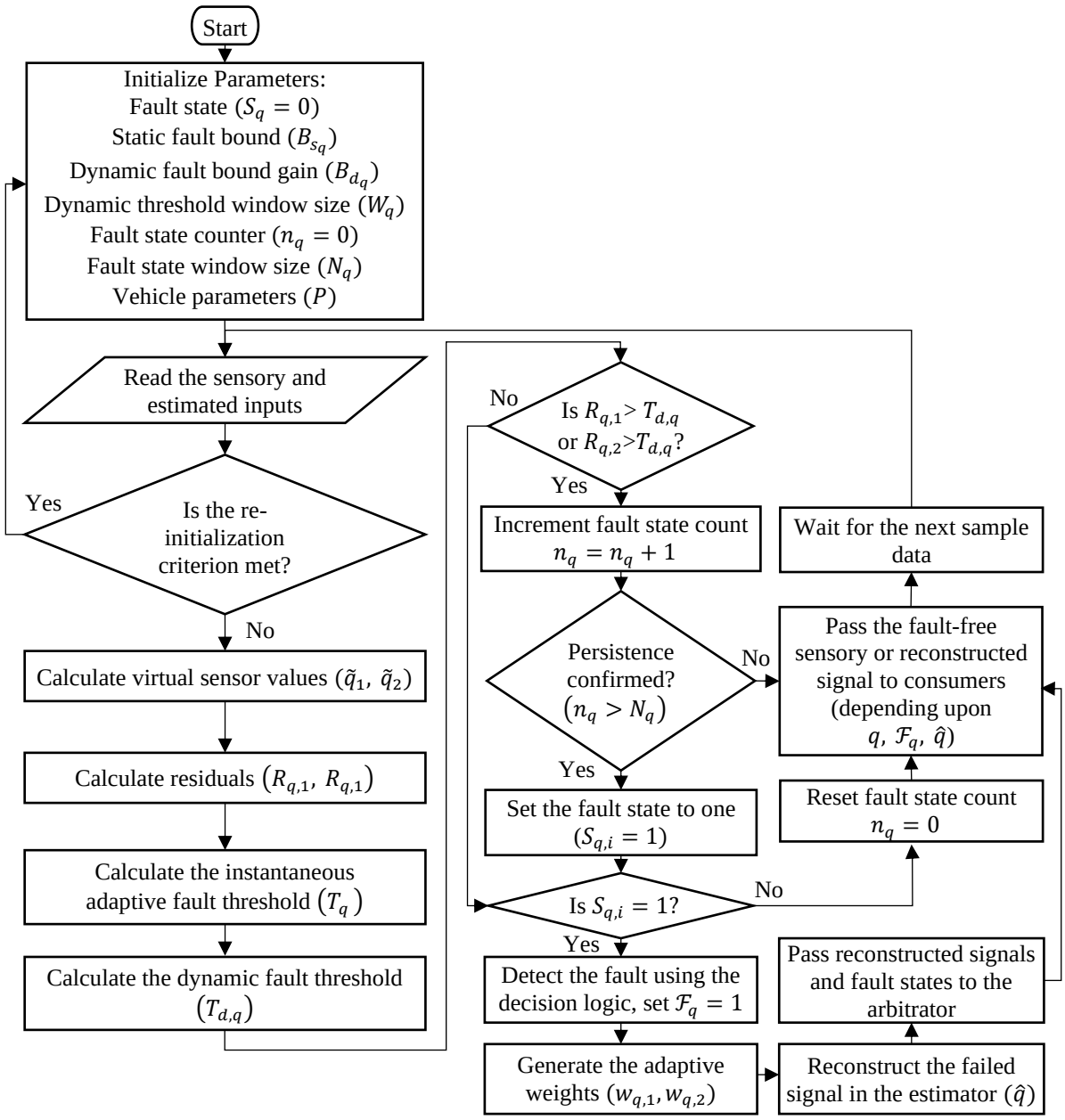

Figure 4.3. Fault detection and signal reconstruction process

4.8.1 Generating and Processing the Residuals

The residual processing steps are similar to what was presented in the previous chapter. For each sensor $q \in \{a_{x_s}, a_{y_s}, a_{z_s}, \dot{\psi}_s, \delta_s\}$, two residuals are generated using the virtual sensors ($\tilde{q}_1, \tilde{q}_2$):

$$R_{q,i} = |q - \tilde{q}_i| \qquad i \in \{1, 2\} \tag{4-61}$$

The residual processor computes the fault bounds (B_{s_q}, B_{d_q}), adaptive thresholds $(T_q, T_{d,q})$, time window (W_q), fault state counter (n_q) and checks the persistency against the fault window (N_q). If a residual $R_{q,i}$ is above the thresholds and the persistence is confirmed, the corresponding fault state $(S_{q,i})$ is set to one by the algorithm. These residual processing steps in Figure 4.3 are executed once per each sensor q to cover the five sensors discussed in this chapter. The fault state flags $S_{q,i} \in \{S_{a_x,1}, S_{a_x,2}, S_{a_y,1}, S_{a_y,2}, S_{a_z,1}, S_{a_z,2}, S_{\dot{\psi},1}, S_{\dot{\psi},2}, S_{\delta,1}, S_{\delta,2}\}$ are then sent to the decision logic module for detecting and localizing the sensor faults.

4.8.2 Decision Logic for Detection and Isolation of Sensor Faults

Effects of each sensor fault on the entire set of residuals need to be evaluated to localize the fault. Consider a case where the lateral acceleration sensor (a_{y_s}) is faulty, and all other sensors are healthy. In this case, the fault directly impacts the lateral acceleration residuals $R_{a_y,1}, R_{a_y,2}$. Moreover, since the lateral acceleration sensor measurement is directly or indirectly used in calculation of virtual sensors $\tilde{a}_{x_1}, \tilde{a}_{z_2}$, $\tilde{\dot{\psi}}_1$, and $\tilde{\delta}_1$, the lateral acceleration fault also impacts $R_{a_x,1}, R_{a_z,2}, R_{\dot{\psi},1}$ and $R_{\delta,1}$. The rest of the residuals are not impacted in this case. Therefore, the fault signature for the lateral acceleration sensor fault is $[S_{a_x,1}\ S_{a_x,2}\ S_{a_y,1}\ S_{a_y,2}\ S_{a_z,1}\ S_{a_z,2}\ S_{\dot{\psi},1}\ S_{\dot{\psi},2}\ S_{\delta,1}\ S_{\delta,2}]$=[1 0 1 1 0 1 1 0 1 0]. Similarly, explicit fault signatures can be assigned to each possible sensor fault as listed in Table 4.1.

Table 4.1. Fault signatures for detection of sensor faults

Fault Signature	Faulty Sensor					
	a_{x_s}	a_{y_s}	a_{z_s}	$\dot{\psi}_s$	δ_s	No Fault
$S_{a_x,1}$	1	1	0	1	1	0
$S_{a_x,2}$	1	0	0	0	1	0
$S_{a_y,1}$	1	1	0	1	1	0
$S_{a_y,2}$	0	1	0	0	1	0
$S_{a_z,1}$	0	0	1	0	0	0
$S_{a_z,2}$	1	1	1	0	0	0
$S_{\dot{\psi},1}$	1	1	0	1	1	0
$S_{\dot{\psi},2}$	0	0	0	1	1	0
$S_{\delta,1}$	1	1	0	0	1	0
$S_{\delta,2}$	0	0	0	1	1	0

4.9 Fault Detectability and Isolability Analysis

As discussed in the previous chapter, fault detectability and isolability can be investigated using the fault signature matrix. For the fault state $\mathcal{S} = \left[S_{a_x,1}\ S_{a_x,2}\ S_{a_y,1}\ S_{a_y,2}\ S_{a_z,1}\ S_{a_z,2}\ S_{\dot{\psi},1}\ S_{\dot{\psi},2}\ S_{\delta,1}\ S_{\delta,2}\right]^T$ and the fault vector $\mathcal{F} = \left[\mathcal{F}_{a_{x_s}}\ \mathcal{F}_{a_{y_s}}\ \mathcal{F}_{a_{z_s}}\ \mathcal{F}_{\dot{\psi}_s}\ \mathcal{F}_{\delta_s}\right]^T$, the signature matrix is constructed using Table 4.1:

$$G = \begin{bmatrix} 1 & 1 & 0 & 1 & 1 \\ 1 & 0 & 0 & 0 & 1 \\ 1 & 1 & 0 & 1 & 1 \\ 0 & 1 & 0 & 0 & 1 \\ 0 & 0 & 1 & 0 & 0 \\ 1 & 1 & 1 & 0 & 0 \\ 1 & 1 & 0 & 1 & 1 \\ 0 & 0 & 0 & 1 & 1 \\ 1 & 1 & 0 & 0 & 1 \\ 0 & 0 & 0 & 1 & 1 \end{bmatrix} \tag{4-62}$$

Since $rank[G_q] > 0$ for all columns in G and all columns in G are unique, the proposed fault detection algorithm satisfies the fault detectability, complete fault detectability and fault isolability conditions. Consequently, all individual sensor faults $\mathcal{F}_{a_{x_s}}, \mathcal{F}_{a_{y_s}}, \mathcal{F}_{a_{z_s}}, \mathcal{F}_{\dot{\psi}_s}$ and $\mathcal{F}_{\delta_s}$ can be detected and localized using the proposed algorithm.

Further analysis of Table 4.1 and the signature matrix G verifies that evaluating a reduced set of fault states is sufficient to detect and isolate the faults. As an example, if both $S_{a_y,1}$ and $S_{a_y,2}$ are equal to one, then there is a sufficient indication for the lateral acceleration sensor fault regardless of the other fault state values. Therefore, to reduce complexity and save computational resources, the decision logic for detection and isolation of the faults can be updated as summarized in Table 4-2.

Consequently, the modified fault signature matrix is updated as:

$$G = \begin{bmatrix} 1 & 0 & 0 & 0 & 0 \\ 0 & 1 & 0 & 0 & 0 \\ 0 & 0 & 1 & 0 & 0 \\ 0 & 0 & 0 & 1 & 0 \\ 0 & 0 & 0 & 0 & 1 \end{bmatrix} \tag{4-63}$$

which still meets the detectability and isolability conditions since all columns are non-zero and unique. The updated decision logic will be used in the next section for reconstruction of faulty signals.

Table 4.2. Decision logic for detection of sensor faults and reconstruction of faulty signals

Fault Signature	Faulty Sensor					
	a_{x_s}	a_{y_s}	a_{z_s}	$\dot{\psi}_s$	δ_s	No Fault
$S_{a_x} = S_{a_x,1}$ & $S_{a_x,2}$	1	0	0	0	0	0
$S_{a_y} = S_{a_y,1}$ & $S_{a_y,2}$	0	1	0	0	0	0
$S_{a_z} = S_{a_z,1}$ & $S_{a_z,2}$	0	0	1	0	0	0
$S_{a_y} = S_{\dot{\psi},1}$ & $S_{\dot{\psi},2}$	0	0	0	1	0	0
$S_{\delta} = S_{\delta,1}$ & $S_{\delta,2}$	0	0	0	0	1	0

4.10 Reconstruction of Faulty Signals

When a sensor fault is detected by the algorithm, the failed signal can be reconstructed using the virtual sensors. For each sensor $q \in \{a_{x_s}, a_{y_s}, a_{z_s}, \dot{\psi}_s, \delta_s\}$, a weighted average of the corresponding virtual sensor values $(w_{q,1}\tilde{q}_1 + w_{q,2}\tilde{q}_2)$ can be used to estimate the sensor measurement $(\hat{q})$ and reconstruct the failed signal. The wights $w_{q,1}$ and $w_{q,2}$ have a default value of 0.5 and are further modified by the algorithm depending upon the sensor faults and vehicle dynamics conditions (e.g., wheel slips). Consequently, the reconstructed signals $\hat{a}_{x_s}, \hat{a}_{y_s}, \hat{a}_{z_s}, \hat{\dot{\psi}}_s$ and $\hat{\delta}_s$ can be obtained as:

$$\left[\hat{a}_{x_s}\ \hat{a}_{y_s}\ \hat{a}_{z_s}\ \hat{\dot{\psi}}_s\ \hat{\delta}_s\right] = \left[w_{a_x,1}\tilde{a}_{x_1} + w_{a_x,2}\tilde{a}_{x_2}\quad w_{a_y,1}\tilde{a}_{y_1} + w_{a_y,2}\tilde{a}_{y_2}\quad w_{a_z,1}\tilde{a}_{z_2} + w_{a_z,1}\tilde{a}_{z_2}\quad w_{\dot{\psi},1}\tilde{\dot{\psi}}_1 + w_{\dot{\psi},1}\tilde{\dot{\psi}}_2\quad w_{\delta,1}\tilde{\delta}_1 + w_{\delta,1}\tilde{\delta}_2\right]^T \tag{4-64}$$

To better manage noises and uncertainties, instead of a simple averaging of the virtual sensor values in (4-64), a random walk observer method [19] is integrated in the system to estimate the reconstructed signals. The aggregated system covering the sensors and residuals is summarized with states x_s and measurements y_s:

$$x_s = \left[a_{x_s}, a_{y_s}, a_{z_s}, \dot{\psi}_s, \delta_s\right]^T \tag{4-65}$$

$$y_s = \left[w_{a_x,1}\tilde{a}_{x_1} + w_{a_x,2}\tilde{a}_{x_2}\quad w_{a_y,1}\tilde{a}_{y_1} + w_{a_y,2}\tilde{a}_{y_2}\quad w_{a_z,1}\tilde{a}_{z_2} + w_{a_z,1}\tilde{a}_{z_2}\quad w_{\dot{\psi},1}\tilde{\dot{\psi}}_1 + w_{\dot{\psi},1}\tilde{\dot{\psi}}_2\quad w_{\delta,1}\tilde{\delta}_1 + w_{\delta,1}\tilde{\delta}_2\right]^T \tag{4-66}$$

System dynamics is summarized as:

$$x_s[k+1] = A_s x_s[k] + w_s \tag{4-67}$$

$$y_s[k] = H_s(x_s[k], u_s[k]) + v_s \tag{4-68}$$

where $A_s = I_{5\times5}$ is the state matrix, w_s represents the process uncertainties and v_s represents the measurement noise. The measurement function H_s is obtained from Equation (4-66) and the virtual sensor equations in the previous sections. The random walk observer is implemented using the UKF method to estimate the states and deliver the reconstructed states ($\hat{x}_s = [\hat{a}_{x_s}, \hat{a}_{y_s}, \hat{a}_{z_s}, \hat{\dot{\psi}}_s, \hat{\delta}_s]$). More details on the random walk observer and the UKF method is provided in Chapter 5.

4.11 Experiment Results

The experimental results for detection of sensor faults and reconstruction of faulty signals in a variety of driving maneuvers are presented in this section. The test vehicle and parameters are similar to the setup that was reviewed in Chapter 3. Parameters for the fault detection and signal reconstruction algorithm are summarized in Table 4.3.

Table 4.3. Parameters for residual processing, fault detection and signal reconstruction

Parameter	Value	Parameter	Value	Parameter	Value
$B_{s_{a_x}}$	0.5	$B_{s_{a_z}}$	0.5	B_{s_δ}	0.5
B_{d_x}	0.04	$B_{d_{a_z}}$	0.15	B_{d_δ}	0.05
N_{a_x}	30	N_{a_z}	20	N_δ	10
W_{a_x}	300	W_{a_z}	500	W_δ	500
$B_{s_{a_y}}$	1	$B_{s_{\dot{\psi}}}$	0.08	$w_{q,i}$	0.5
$B_{d_{a_y}}$	0.2	$B_{d_{\dot{\psi}}}$	0.14	σ	3.2
N_{a_y}	30	$N_{\dot{\psi}}$	10	v_0	1
W_{a_y}	200	$W_{\dot{\psi}}$	300	K_{us}	25

4.11.1 Experiment Results when all Sensors are Functional

As the first case study, a step-steer maneuver combined with longitudinal excitations is executed while all sensors are functioning properly. The objective is to evaluate accuracy of the virtual sensors and verify that the algorithm does not generate false positives when there is no sensor fault. Driver's steering

wheel command, wheel torque commands, longitudinal velocity and trajectory of the vehicle are shown in Figure 4.4.

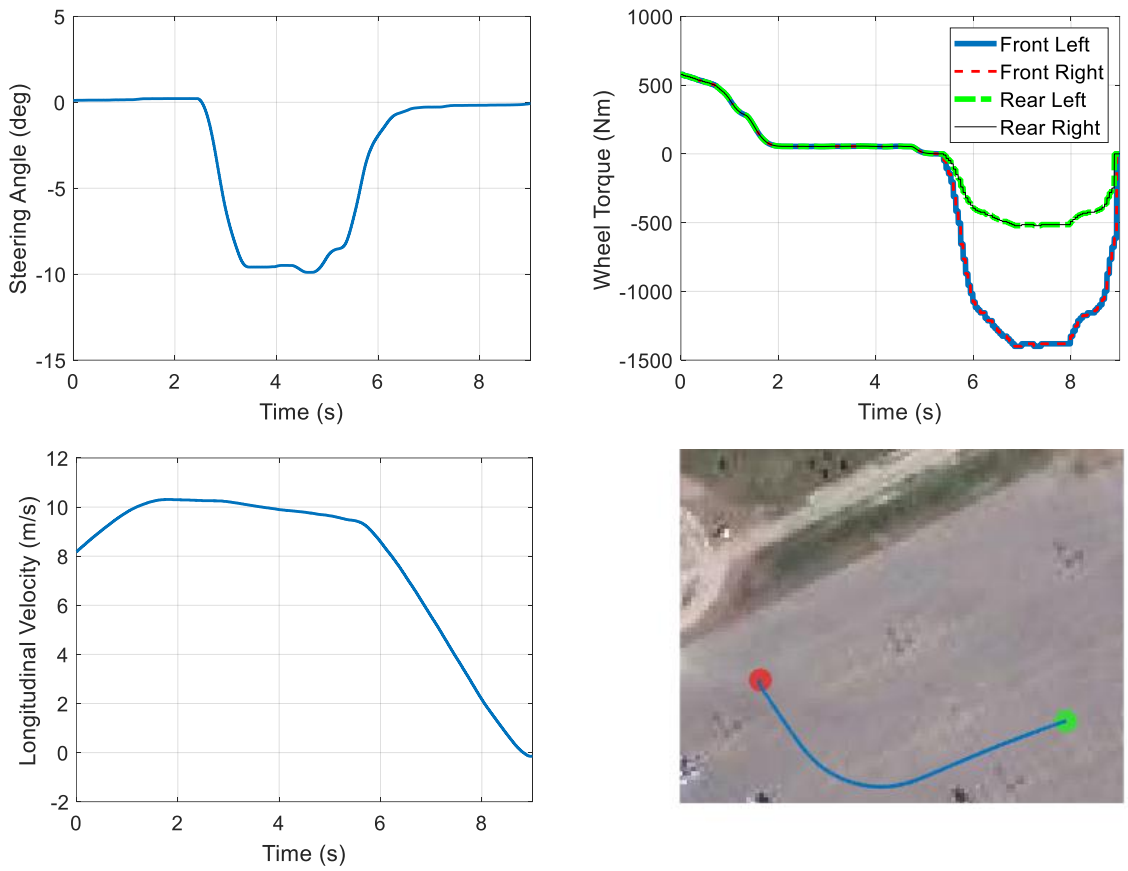

Figure 4.4. Driver commands and and trajectory of the vehicle during the meanuever with no fault

Experiment results for lateral acceleration virtual sensors and residuals are shown in Figure 4.5. The results illustrate that the virtual sensors can accurately replicate the actual measured lateral acceleration of the vehicle. In the middle of the maneuver and when the vehicle is excited in the lateral direction, the adaptive threshold has increased to prevent potential false alarms that might have been generated due to model uncertainties and residual spikes. Both residuals are below the adaptive threshold for the entire maneuver and no fault is detected by the algorithm.

Similarly, virtual sensor measurements and residuals for the longitudinal acceleration, vertical acceleration, yaw rate and steering angle sensors are shown in Figure 4.6 to Figure 4.9.

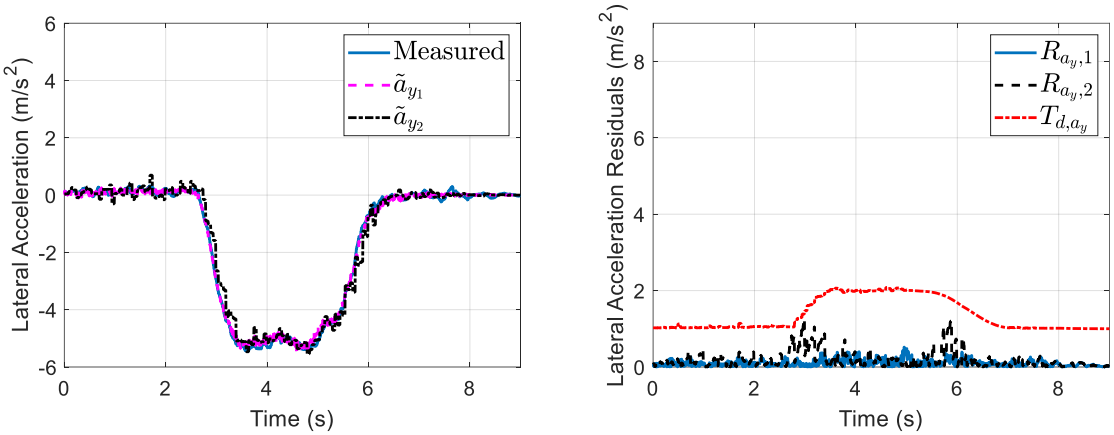

Figure 4.5. Lateral acceleration virtual sensors and residuals

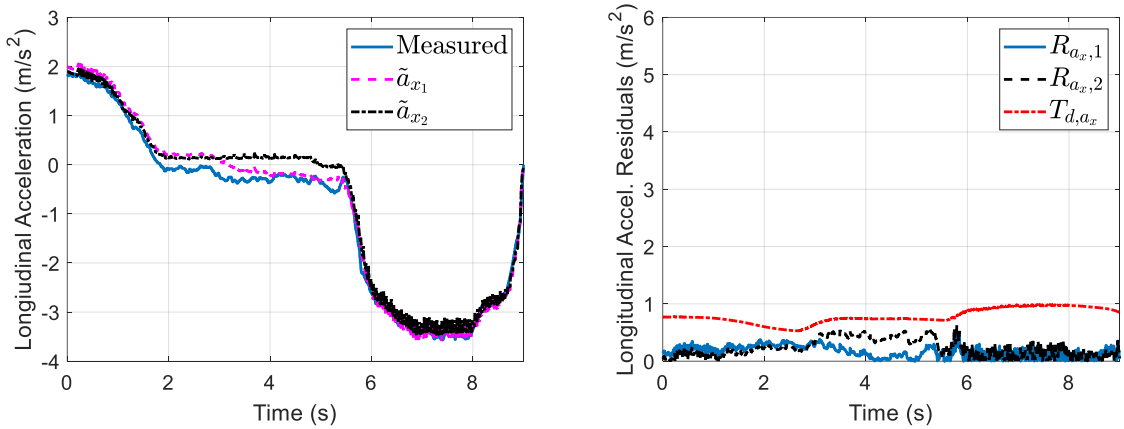

Figure 4.6. Longitudinal acceleration virtual sensors and residuals

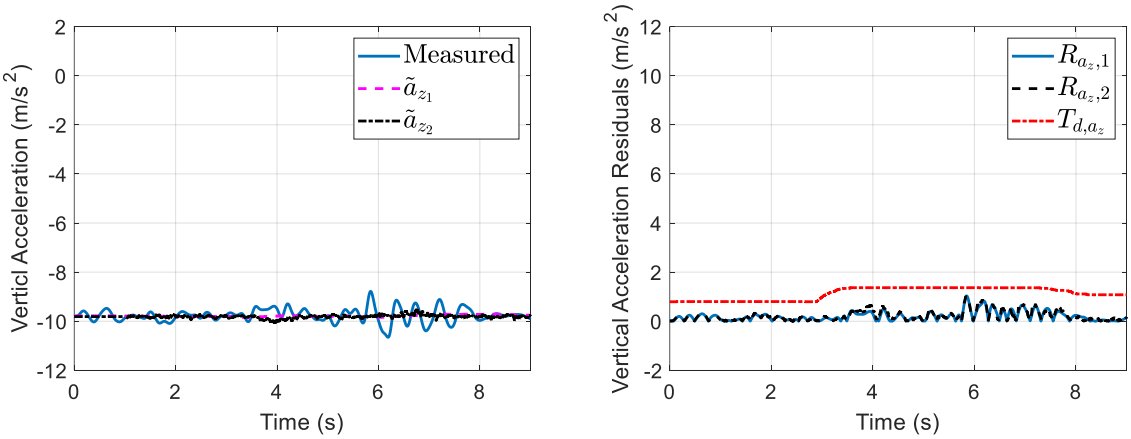

Figure 4.7. Vertical acceleration virtual sensors and residuals

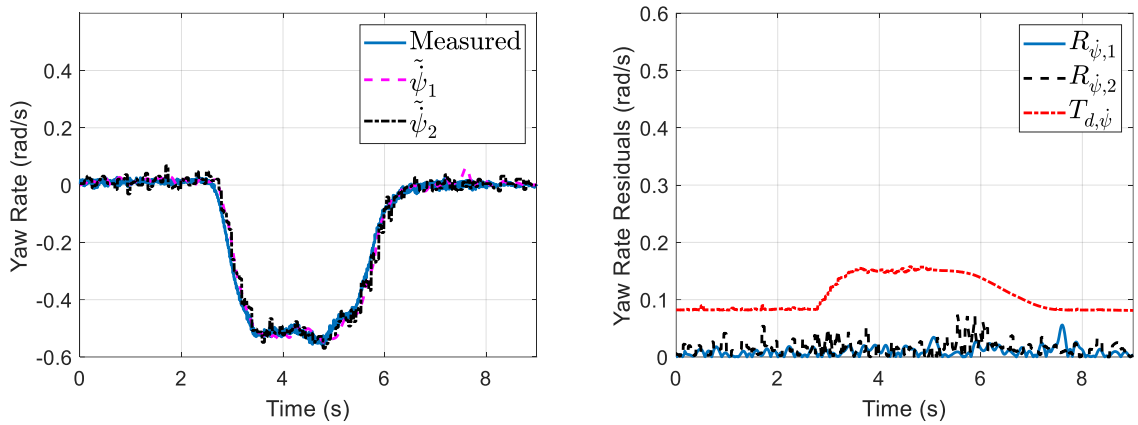

Figure 4.8. Yaw rate virtual sensors and residuals

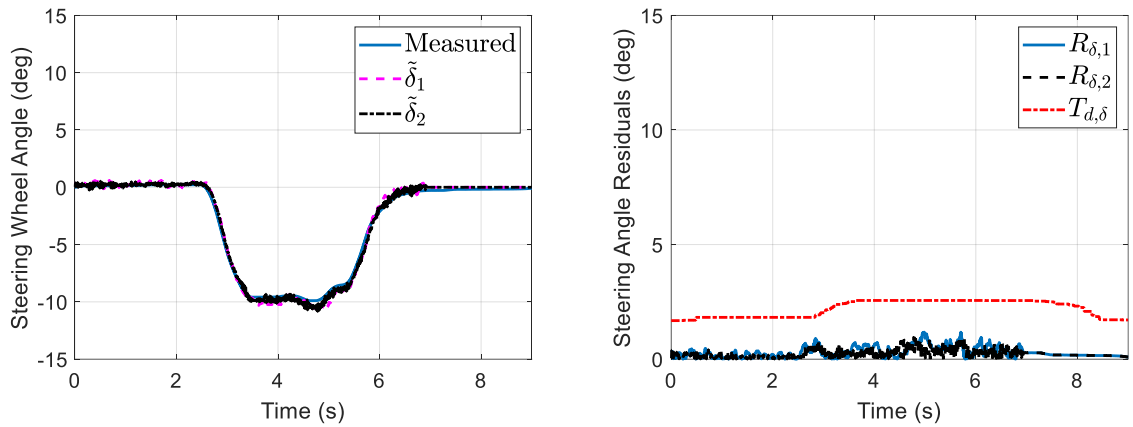

Figure 4.9. Steering angle virtual sensors and residuals

The results demonstrate reliable performance of the virtual sensors to replicate sensor measurements and illustrate advantages of the adaptive threshold in terms of avoiding false positives.

4.11.2 Fault Detection and Signal Reconstruction for Lateral Acceleration Sensor

Performance of the proposed structure for detection of a lateral acceleration sensor fault and reconstruction of the faulty signals is analyzed during a double-lane-change (DLC) maneuver. Driver's steering wheel command, wheel torque commands and trajectory of the vehicle are shown in Figure 4.10. The lane change portion of the maneuver is performed at the speed of 40kph. Lateral acceleration fault is injected at $t = 3.5s$ by replacing the measured lateral acceleration with a zero signal for the rest of the maneuver.

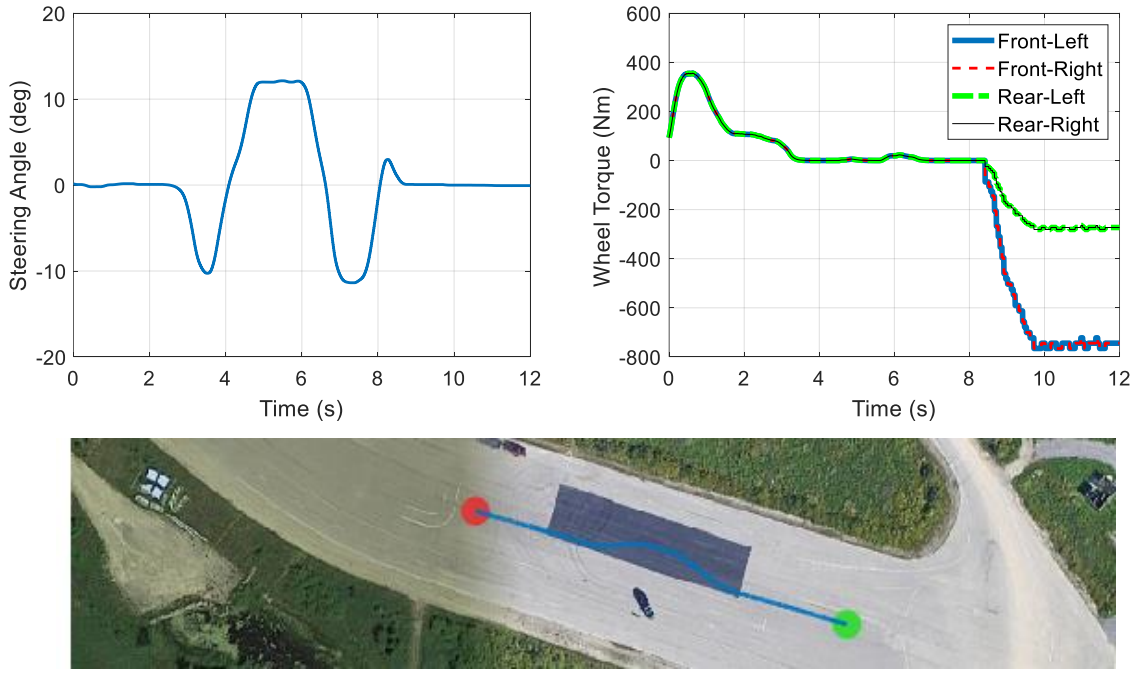

Figure 4.10. Driver commands and trajectory of the vehicle during the maneuver with lateral acceleration sensor fault

Lateral acceleration residuals and the fault state are shown in Figure 4.11. Both residuals exceed the adaptive threshold after the fault occurs. The algorithm detected the fault at $t = 3.65s$ and sets the lateral acceleration fault state to one. The result also shows that the algorithm reliably estimated the actual magnitude of the fault using the virtual sensors $\left(\tilde{a}_{y_1}, \tilde{a}_{y_2}\right)$.

After detecting the fault, the algorithm starts reconstructing the lateral acceleration signal using the virtual sensors. The reconstructed signal is compared with the actual lateral acceleration of the vehicle and the faulty signal in Figure 4.12. The result shows that the lateral acceleration signal is successfully reconstructed after detection of the fault. In this case study, the NRMSE for the reconstructed signal is 7.68%.

The reconstructed signal can be used by other vehicle estimation and control modules to continue a reliable operation despite the sensor fault. Fault-tolerant estimation of vehicle states using such reconstructed signals will be studied in Chapter 5.

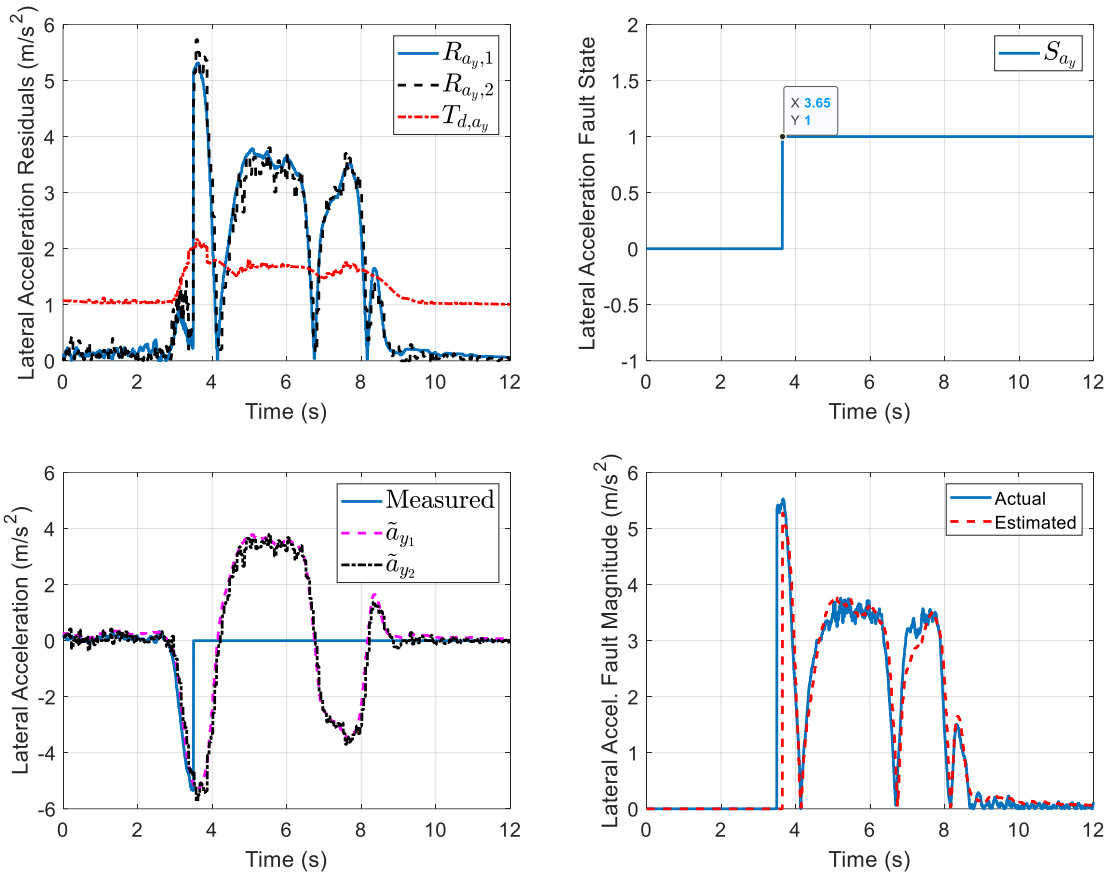

Figure 4.11. Detection of lateral acceleration sensor fault

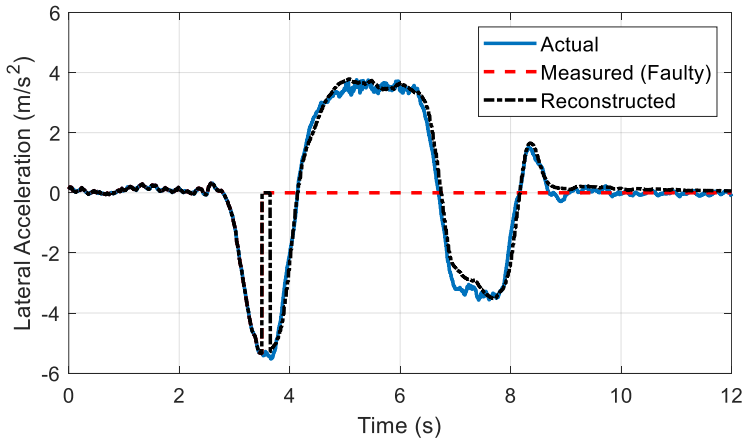

Figure 4.12. Reconstruction of the faulty lateral acceleration signal

4.11.3 Fault Detection and Signal Reconstruction for Longitudinal Acceleration Sensor

A lane-change maneuver followed by a harsh braking is executed to evaluate the performance of the proposed method in terms of detection of a longitudinal acceleration sensor fault and reconstruction of the faulty signal. Driver commands and trajectory of the vehicle are shown in Figure 4.13.

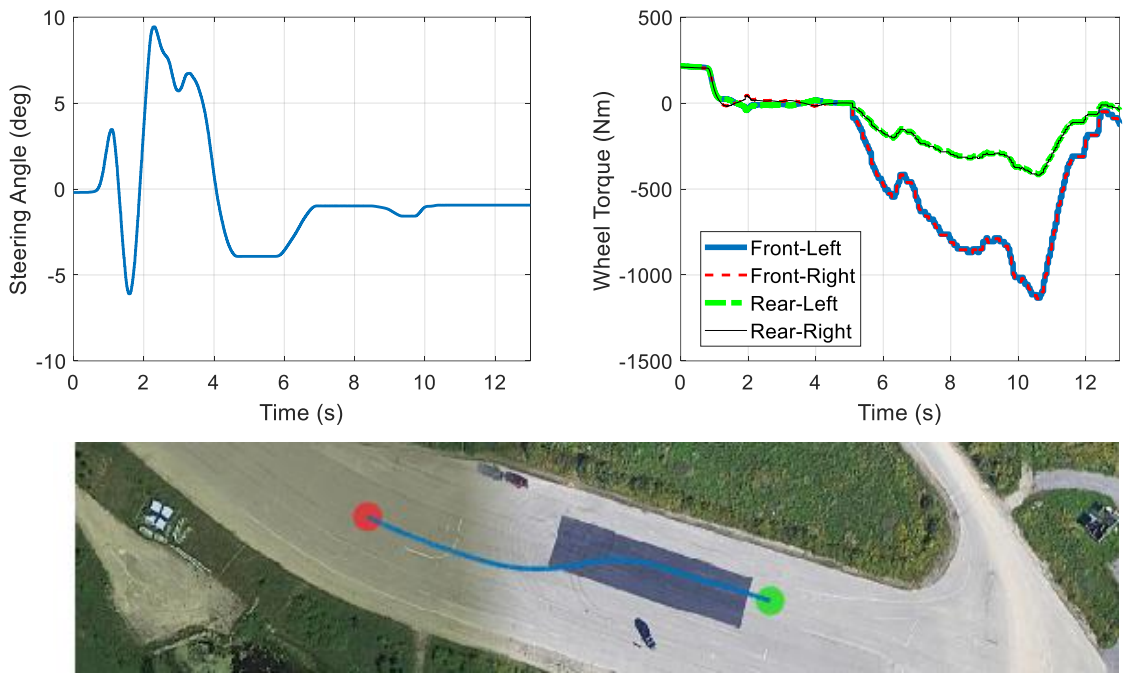

Figure 4.13. Driver commands and trajectory of the vehicle during the maneuver with longitudinal acceleration sensor fault

The sensor fault in this case is a scaling fault (gain fault). The fault is injected such that the sensor reports 10% of the actual lateral acceleration of the vehicle after $t = 7s$.

Longitudinal acceleration residuals and the fault state are shown in Figure 4.14. The results show that the fault is detected at $t = 7.15s$ and the fault magnitude is reliably estimated using the virtual sensors.

Figure 4.15 shows the reconstructed longitudinal acceleration signal and verifies accurate reconstruction of the failed signal by the proposed method. In this case study, the NRMSE for reconstruction of the longitudinal acceleration signal is 4.53%. The high-frequency noise on the reconstructed signal is due to the unfiltered input signals which feed into the virtual sensors (e.g. wheel

angular velocities, accelerations, etc.). Filtering was avoided to prevent a phase shift in the reconstructed signal.

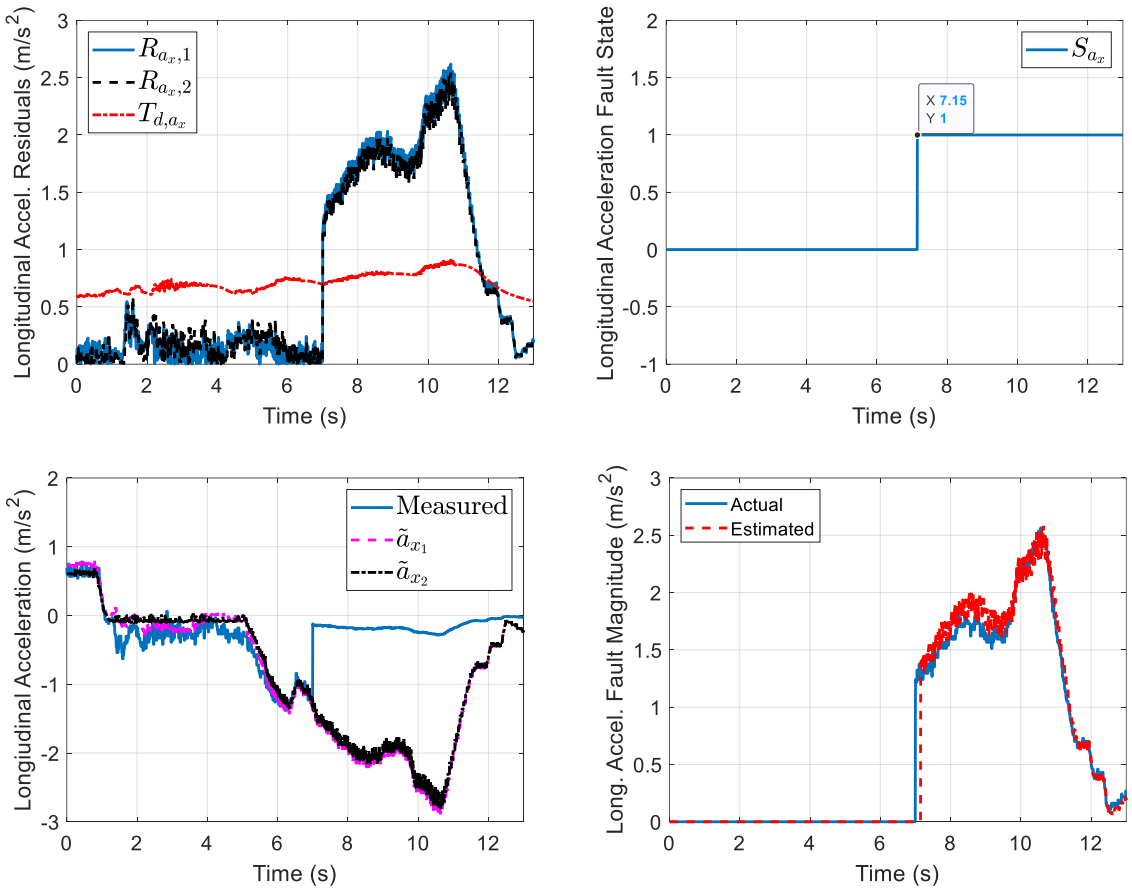

Figure 4.14. Detection of longitudinal acceleration sensor fault

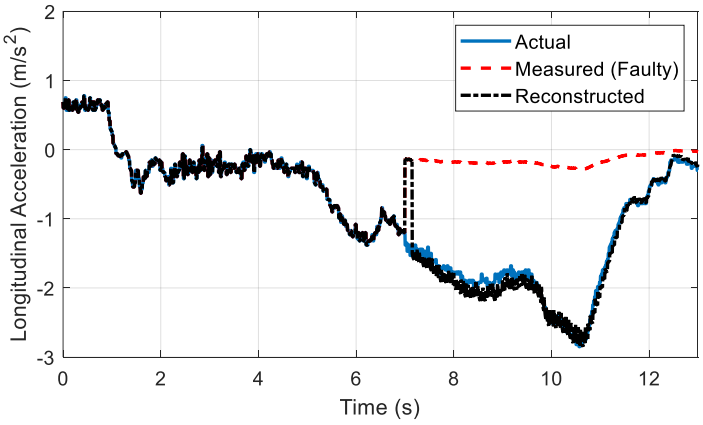

Figure 4.15. Reconstruction of the faulty longitudinal acceleration signal

4.11.4 Fault Detection and Signal Reconstruction for Vertical Acceleration Sensor

Performance of the proposed algorithm in detection of a vertical acceleration sensor fault and reconstruction of the faulty signal is investigated during an acceleration/braking maneuver. Driver's steering wheel command, wheel torque command, vehicle speed and trajectory of the vehicle are shown in Figure 4.16.

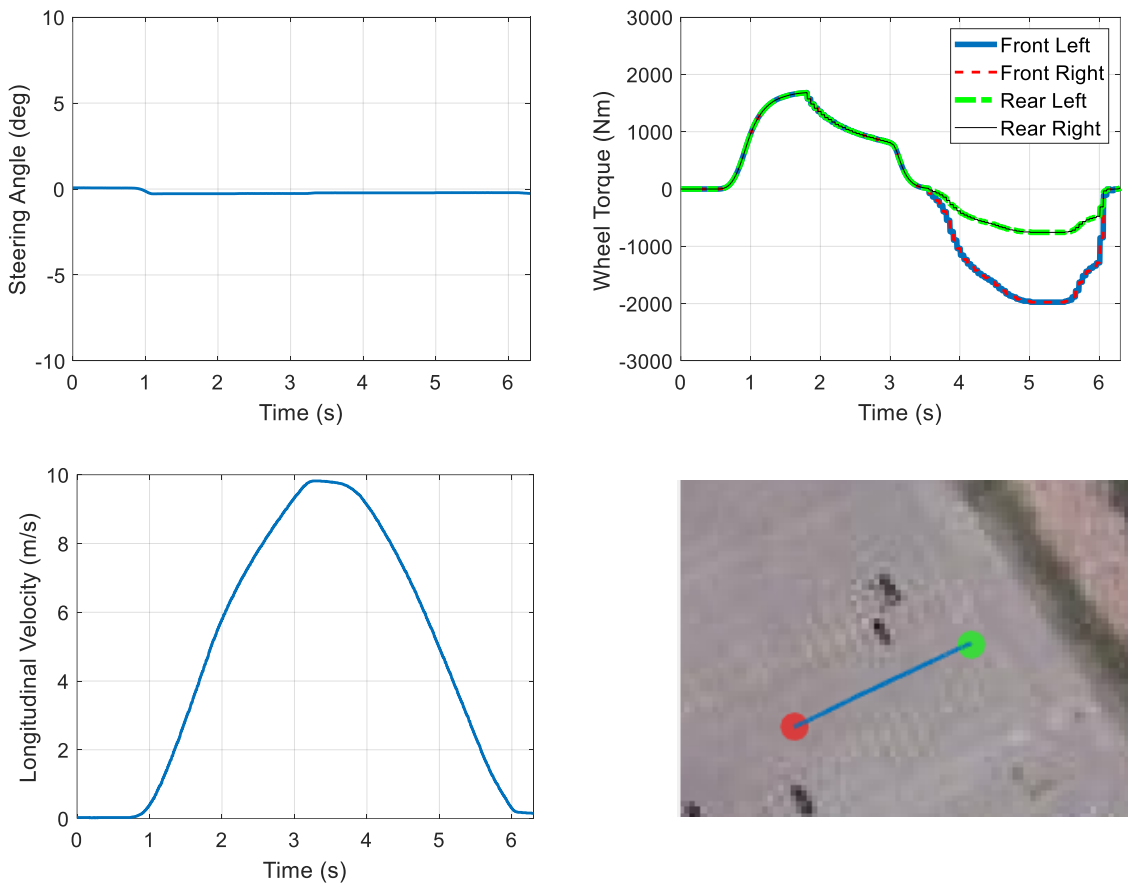

Figure 4.16. Driver commands and trajectory of the vehicle during the maneuver with vertical acceleration sensor fault

A vertical acceleration fault is injected at $t = 3s$ by replacing the measured vertical acceleration with a zero signal for the rest of the maneuver. Experiment results for detection of the fault are shown in Figure 4.17. Both residuals exceed the adaptive threshold as soon as the fault occurs. Consequently, the algorithm detected the fault at $t = 3.1s$ after confirming the persistence and correctly estimated the fault magnitude. The failed signal is reconstructed for the rest of the maneuver as shown in Figure 4.18.

During the reconstruction period, the NRMSE is 1.22% which confirms the desirable performance of the proposed method in terms of accurate reconstruction of the faulty signal.

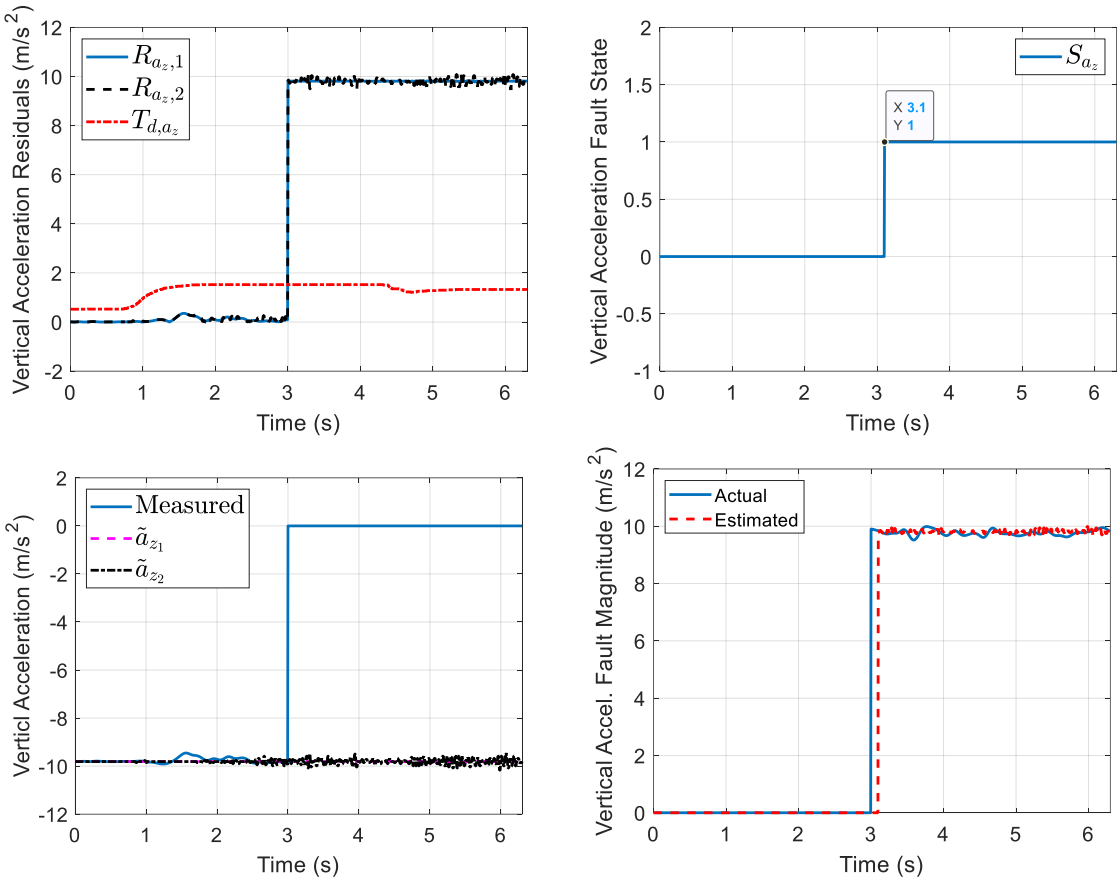

Figure 4.17. Detection of vertical acceleration fault

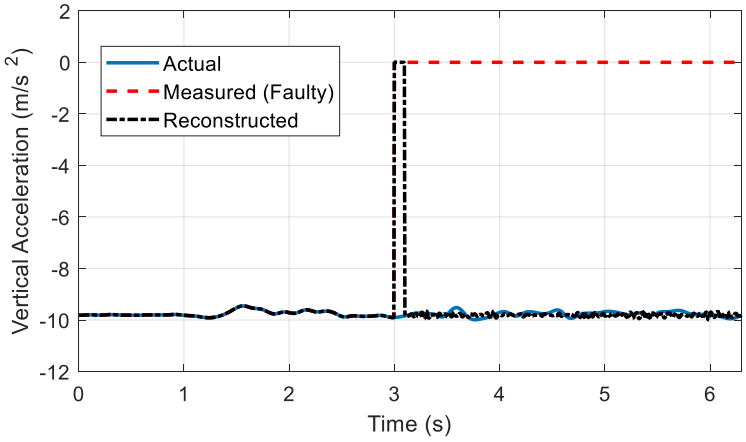

Figure 4.18. Reconstruction of the faulty vertical acceleration signal

4.11.5 Fault Detection and Signal Reconstruction for Yaw Rate Sensor

Detection of a bias fault on the yaw rate measurement and reconstruction of the faulty signal is studied in this section. The vehicle performs a lane-change maneuver on a wet sealer with a low friction coefficient ($\mu \approx 0.4$). Driver's steering wheel command, torque commands and trajectory of the vehicle are shown in Figure 4.19. Figure 4.20 shows the wheel angular velocities during the maneuvers.

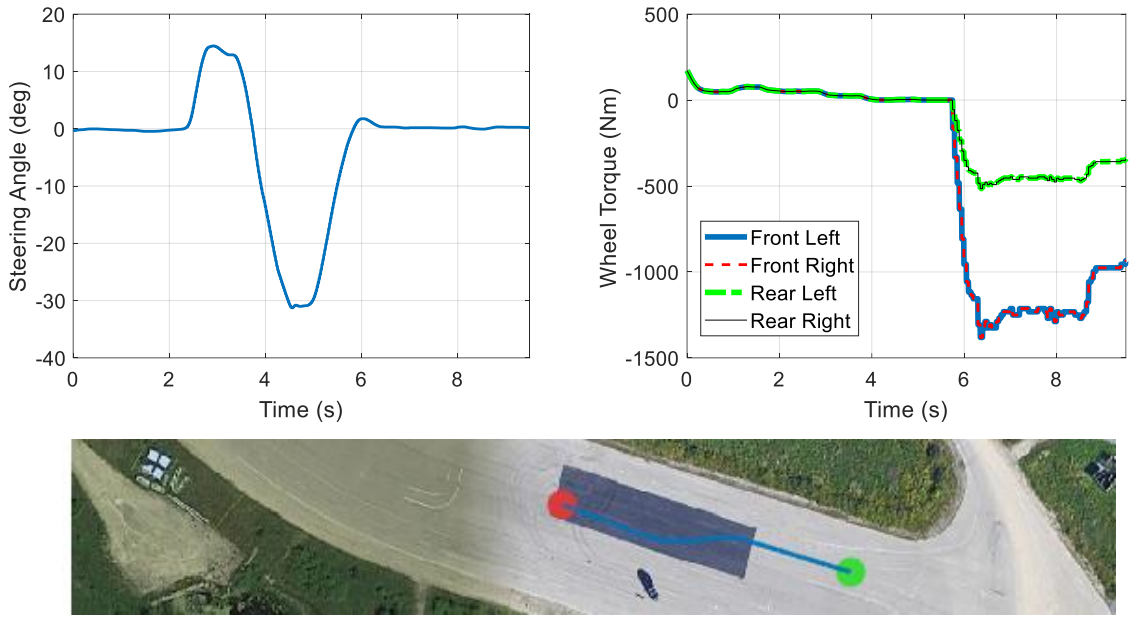

Figure 4.19. Driver commands and trajectory of the vehicle during maneuver with yaw rate sensor fault

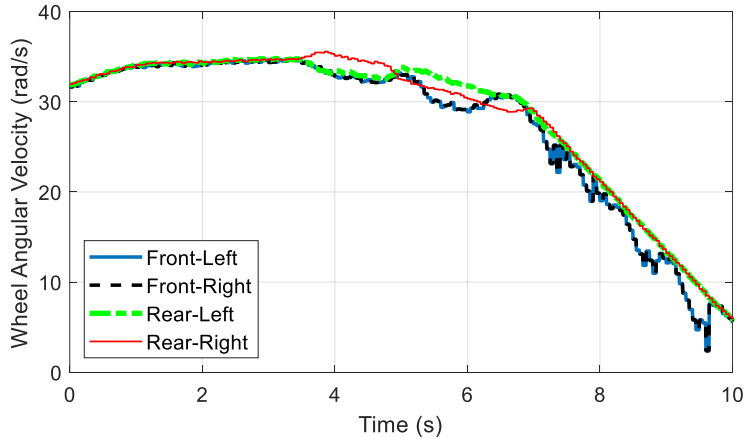

Figure 4.20. Wheel angular velocities during the lane-change maneuver on the wet road

Significant wheel slips are observed especially on the front wheels during this maneuver. This is expected considering the road surface condition and the aggressive steering and braking commands.

From the beginning of the maneuver, a constant bias of 0.1 rad/s is added to the measured yaw rate by the sensor. Yaw rate residuals, fault state, virtual sensor values, and the estimated fault magnitude are shown in Figure 4.21. The residuals are above the adaptive fault threshold from the beginning of the maneuver and the algorithm detects the fault at $t = 0.05s$.

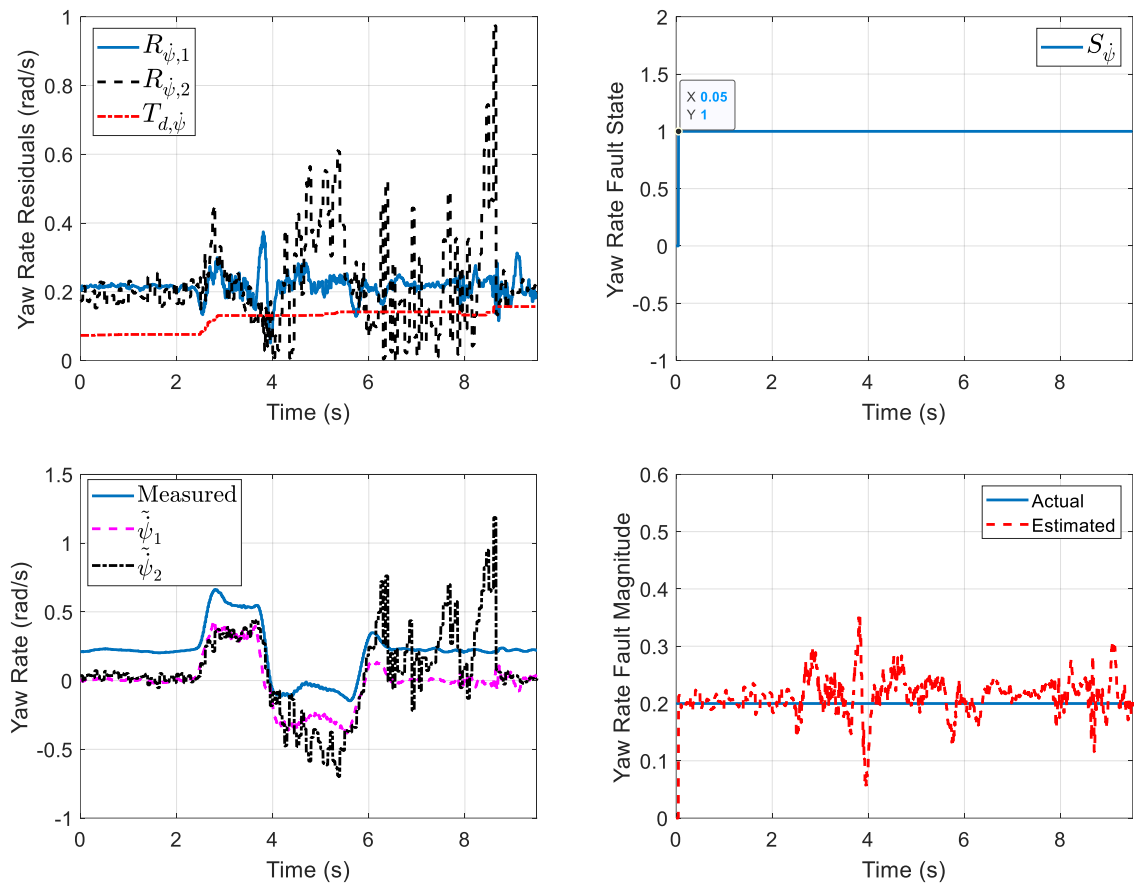

Figure 4.21. Detection of the yaw rate sensor fault

Figure 4.22 compares the actual, faulty and reconstructed signals. The result shows the desirable reconstruction of the yaw rate signal despite the unfavorable road surface condition, wheel slips and the aggressive steering command. The adaptive weights $(w_{\dot{\psi},1}, w_{\dot{\psi},2})$ for contribution of the virtual sensors $(\hat{\dot{\psi}}_1, \hat{\dot{\psi}}_2)$ in the reconstruction process are shown in Figure 4.23. These weights are automatically modified by the proposed method during the maneuver. In regions with considerable

wheel slips, the algorithm reduced the effect of the second yaw rate virtual sensor $\left(\hat{\dot{\psi}}_2\right)$. This is desirable since the second virtual sensor relies on wheel angular velocities and is less accurate when there is a high wheel slip.

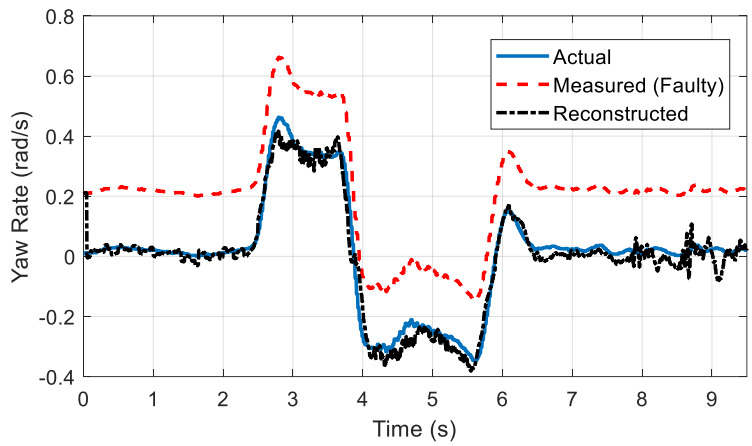

Figure 4.22. Reconstruction of the faulty yaw rate signal

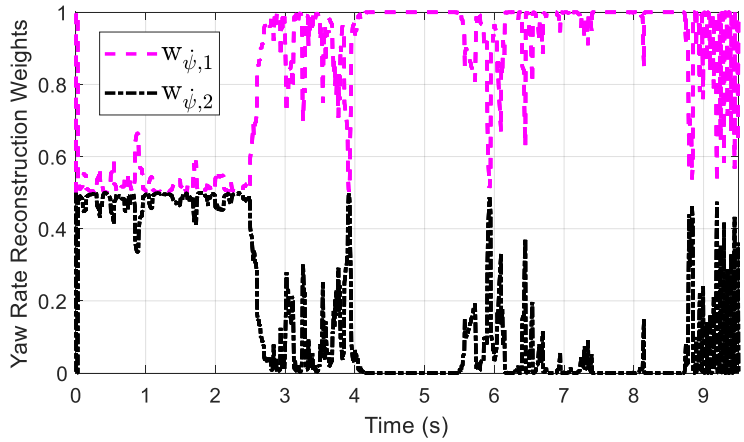

Figure 4.23. Adaptive virtual sensor weights for reconstruction of the yaw rate fault

In this case study, the NRMSE for the reconstructed yaw rate is 11.28%. The results confirm a desirable reconstruction performance and showcase advantages of the adaptive estimator in terms of a more accurate reconstruction of the failed signal in challenging driving conditions.

4.11.6 Fault Detection and Signal Reconstruction for Steering Angle Sensor

Performance of the proposed structure in detection of a steering angle sensor fault and reconstruction of the faulty signal is analyzed during a slalom maneuver. Driver's steering wheel command, wheel torque commands and trajectory of the vehicle are shown in Figure 4.24.

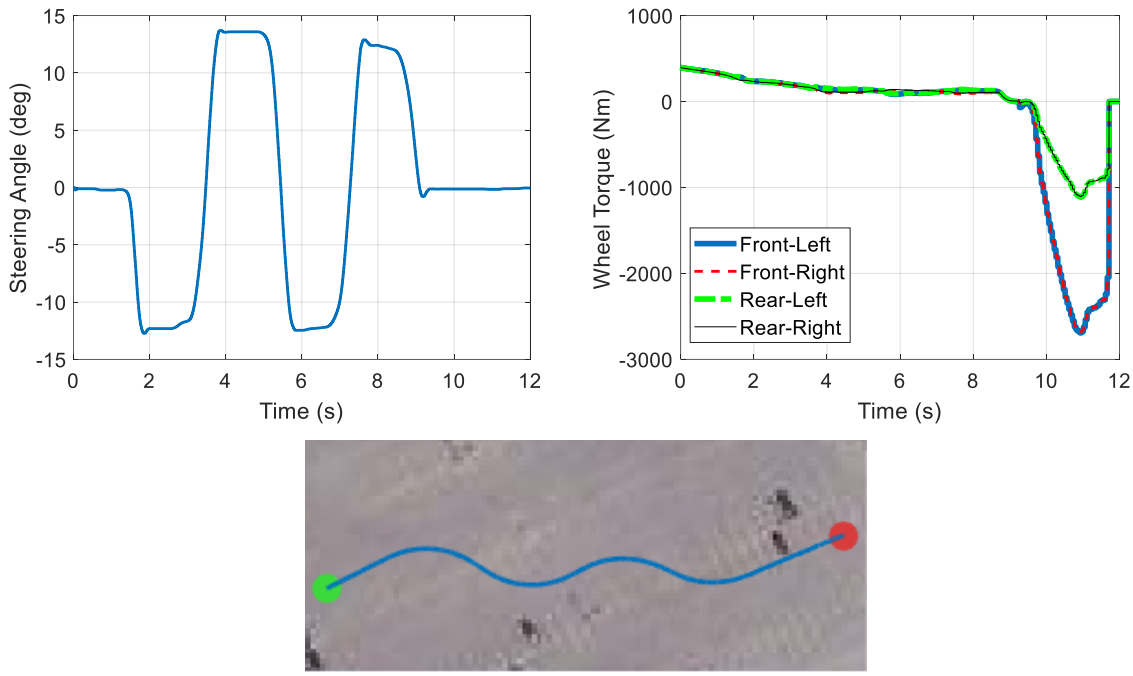

Figure 4.24. Driver commands and trajectory of the vehicle during the maneuver with steering angle sensor fault

A stuck-output fault is considered in this case study. The fault is injected such that when the steering angle reaches 5 degrees, the sensor gets stuck in this value and continues to output this fixed measurement until the end of the maneuver. The fault occurs at $\mathrm{t} = 1.58\mathrm{s}$ in this case study.

Figure 4.25 shows that the steering angle residuals exceed the adaptive threshold after the fault occurs. The steering angle fault is detected at $t = 1.725s$ and the fault magnitude is estimated using the virtual sensor values.

Figure 4.26 shows that the faulty steering angle signal is accurately reconstructed after detection of the fault. In this case study, the NRMSE for the reconstructed steering angle is 5.91%.

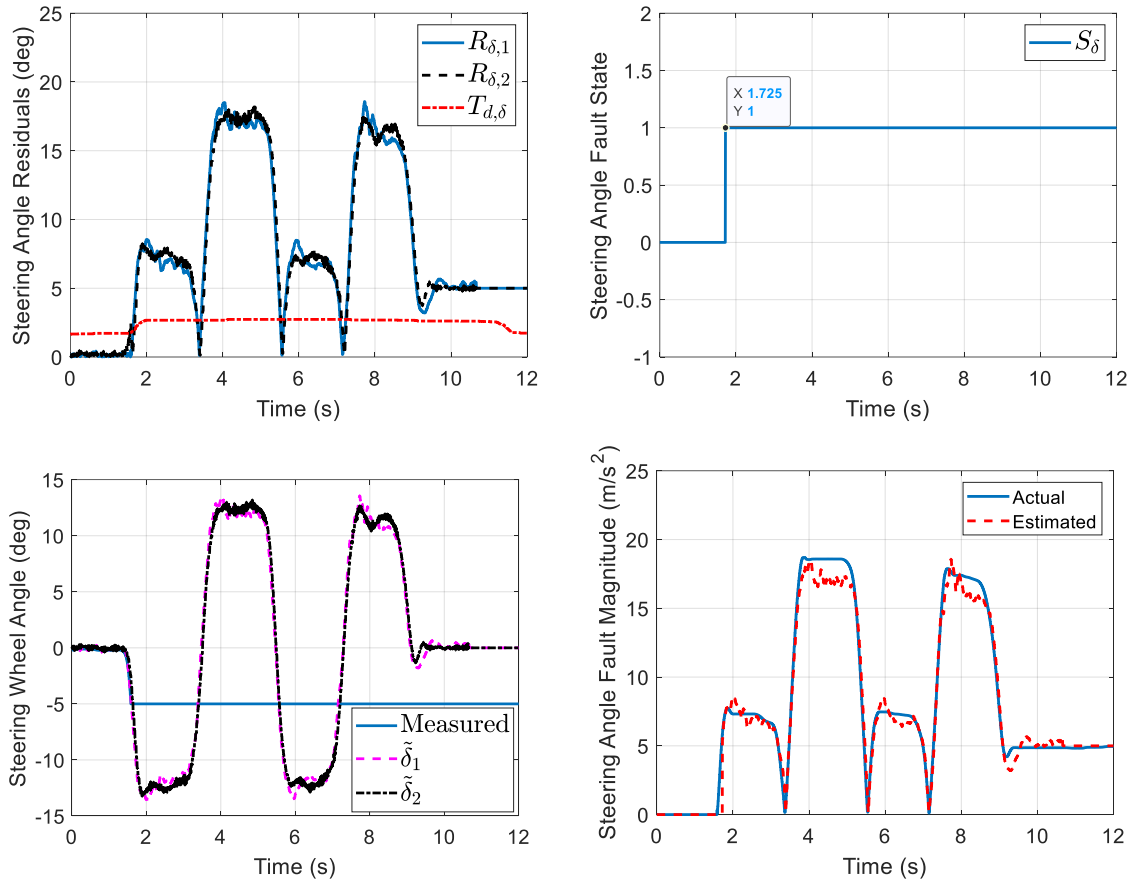

Figure 4.25. Detection of steering angle sensor fault

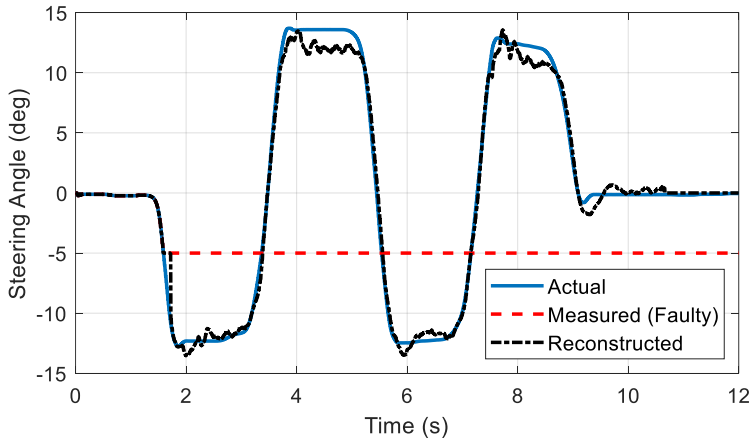

Figure 4.26. Reconstruction of the faulty steering angle signal

4.12 Summary

This chapter presented a structure for detection of longitudinal acceleration, lateral acceleration, vertical acceleration, yaw rate, and steering angel sensor faults and reconstruction of the faulty signals. As the first step for the fault detection process, a set of virtual sensors were developed using the vehicle models, estimated vehicle states and analytical redundancy relations. These virtual sensors helped to generate residuals and unique fault signatures for the fault detection process. A systematic method to detect and isolate sensor faults using the residuals was discussed which benefits from several advantages including the adaptive fault thresholds. Detectability/isolability of faults was verified using the properties of the fault signature matrix. After detecting the sensor faults, reconstruction of the faulty signals was executed using an estimator with adaptive weights to manage contribution of virtual sensors in the reconstruction process. The weights are adapted depending upon the driving condition and the remaining healthy sensor set.

Several experimental case studies were conducted to evaluate the performance of the proposed structure. Various types of sensor faults including loss of signal, bias, stuck-output and scaling faults were considered in the case studies. The experiments covered several driving maneuvers including step-steer, acceleration/braking, lane change, double-lane-change, and slalom maneuvers on a variety of road surface conditions.

The results verified the effectiveness of the proposed structure in terms of avoiding false positives, fast detection of sensor faults and accurate reconstruction of the faulty sensory signals.

Chapter 5
Fault-Tolerant Estimation of Vehicle States

This chapter presents a novel structure for detection of torque sensor faults and fault-tolerant estimation of vehicle states. Combination of the fault detection, signal reconstruction and estimation methods in thesis is also discussed here. Finally, experimental case studies are presented to demonstrate the effectiveness of the proposed approach in various driving scenarios with different sensor faults.

5.1 Introduction

General structure of the proposed method for detection of torque sensor faults, reconstruction of the faulty signals, and fault-tolerant estimation of vehicle states is illustrated in Figure 5.1.

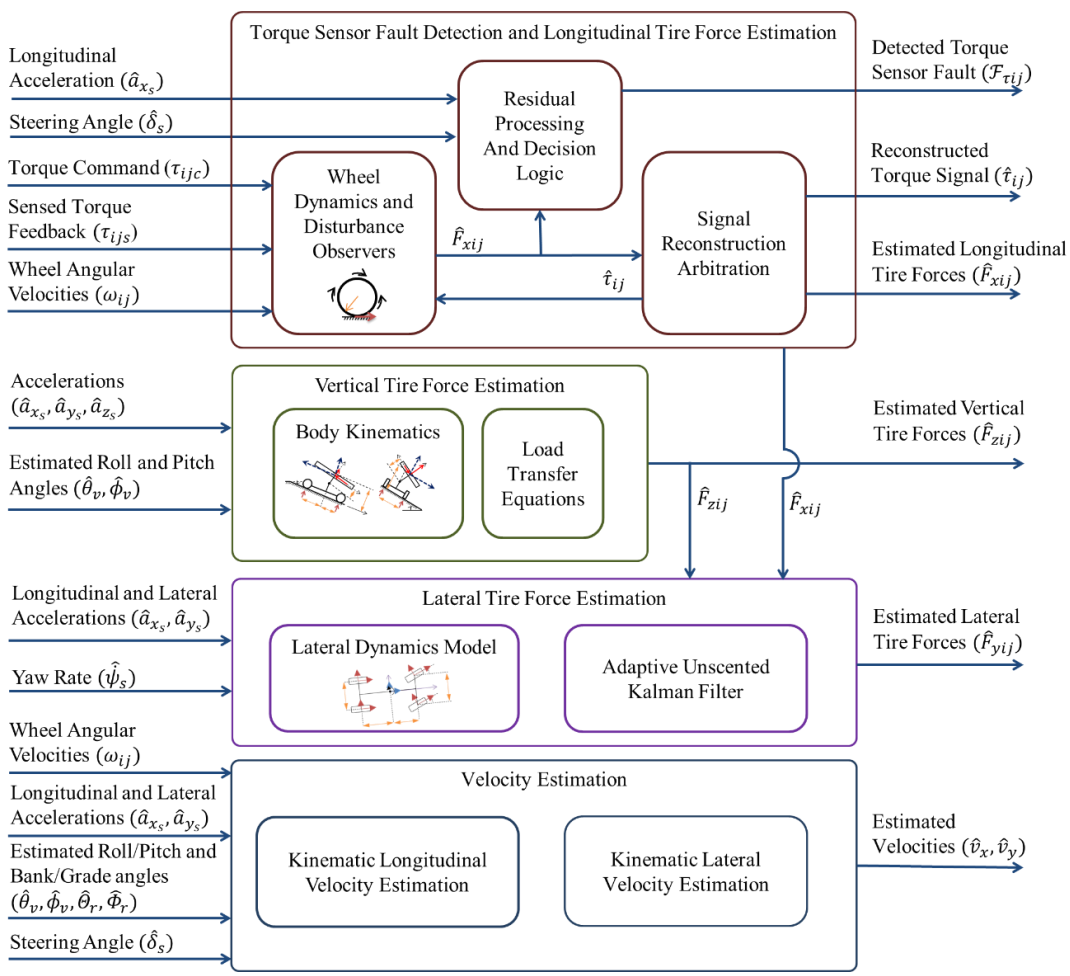

Figure 5.1. Detection of torque sensor faults and fault-tolerant estimation of vehicle states

In this structure, first a set of disturbance observers combined with a residual processor and a decision logic is designed to detect the motor torque sensor faults for the electric vehicle. This module can reconstruct the faulty signal and provide fault-tolerant estimation of longitudinal tire forces even when a torque sensor fails. Estimation of vertical tire forces is discussed next, where the reconstructed acceleration signals from the previous chapter combined with the estimated roll/pitch angles and load transfer equations deliver the fault-tolerant estimates. For lateral tire forces, an adaptive UKF is designed in which effects of measurement faults are mitigated by leveraging the reconstructed input signals and adapting the measurement equations. Fault-tolerant estimation of longitudinal and lateral velocities is achieved by feeding the reconstructed input signals into kinematic velocity estimation methods. Details of the proposed methods are discussed in the next sections.

5.2 Detection of Torque Sensor Faults, Reconstruction of Faulty Signals and Fault-Tolerant Estimation of Longitudinal Tire Forces

A set of disturbance observers is designed to achieve fault-tolerant estimation of longitudinal tire forces in presence of motor torque sensor faults. The wheel dynamics model in Figure 5.2 describes the relationship between longitudinal tire forces (F_{xij}), wheel angular velocities (ω_{ij}), traction torques (τ_{dij}), and brake torques (τ_{bij}) for each wheel [97]:

$$I_w\dot{\omega}_{ij} = \tau_{dij} - \tau_{bij} - r_e F_{xij} \qquad ij \in \{fl, fr, rl, rr\} \tag{5-1}$$

where I_w is the wheel moment of inertia about its spin axis and r_e is the effective tire radius. Since the longitudinal tire force appears as an external disturbance into the wheel dynamics (5-1), a disturbance observer is considered here to estimate this force.

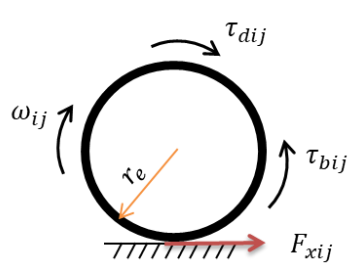

Figure 5.2. Wheel dynamics

Proposition: considering wheel dynamics for each wheel:

$$I_w\dot{\omega}_{ij} = \tau_{ijs} - r_e F_{xij} \tag{5-2}$$

where τ_{ijs} is the sensed torque acting on the wheel ij:

$$\tau_{ijs} = \tau_{dij} - \tau_{bij} \tag{5-3}$$

the following observer can estimate the longitudinal tire force:

$$I_w \dot{\hat{\omega}}_{ij} = \tau_{ijs} - r_e \hat{F}_{xij} + \Lambda \tilde{\omega}_{ij} \tag{5-4}$$

$$\hat{F}_{xij} = \frac{\tau_{ij} - I_w \dot{\omega}_{ij}}{r_e} - (K_P \tilde{\omega}_{ij} + K_I \int \tilde{\omega}_{ij} dt + K_D \dot{\tilde{\omega}}_{ij}) \tag{5-5}$$

where K_P, K_I, K_D and Λ are constant observer gains, $\hat{F}_{xij}$ is the estimated longitudinal force and

$$\tilde{\omega}_{ij} = \omega_{ij} - \hat{\omega}_{ij} \tag{5-6}$$

Proof: Error dynamics can be calculated by subtracting Equation (5-4) from Equation (5-2):

$$I_w \dot{\tilde{\omega}}_{ij} + r_e \tilde{F}_{xij} + \Lambda \tilde{\omega}_{ij} = 0 \tag{5-7}$$

where:

$$\tilde{F}_{xij} = F_{xij} - \hat{F}_{xij} \tag{5-8}$$

Differentiating Equation (5-7) results in:

$$I_w \ddot{\tilde{\omega}}_{ij} + r_e \dot{\tilde{F}}_{xij} + \Lambda \dot{\tilde{\omega}}_{ij} = 0 \tag{5-9}$$

in which $\dot{\tilde{F}}_{xij}$ can be calculated from Equation (5-2) and Equation (5-5):

$$\dot{\tilde{F}}_{xij} = \dot{F}_{xij} - \dot{\hat{F}}_{xij} = K_P \dot{\tilde{\omega}}_{ij} + K_I \tilde{\omega}_{ij} + K_D \ddot{\tilde{\omega}}_{ij} \tag{5-10}$$

Finally, error dynamics can be expressed by replacing Equation (5-10) in Equation (5-9):

$$(I_w + r_e K_D) \ddot{\tilde{\omega}}_{ij} + (\Lambda + r_e K_P) \dot{\tilde{\omega}}_{ij} + (r_e K_I)\, \tilde{\omega}_{ij} = 0 \tag{5-11}$$

By choosing the observer gains such that $K_D > \frac{-I_w}{r_e}$, $K_P > 0$, $\frac{\Lambda}{K_P} > -r_e$ and $K_I > 0$, the error dynamics is stable, thus $\tilde{\omega}_{ij} \longrightarrow 0$ and $\dot{\tilde{\omega}}_{ij} \longrightarrow 0$. Consequently, Equation (5-7) shows that $\tilde{F}_{xij} \longrightarrow 0$ and Equation (5-8) shows that $\hat{F}_{xij} \longrightarrow F_{xij}$.

For the electric vehicle in this thesis, the effective torque on each wheel is available from the in-wheel motor feedbacks. For conventional vehicles, these torques can be calculated using the brake torque, engine torque, and models of the brake, transmission and differential systems. Since the

observer receives wheel torque as inputs, a wheel torque sensor fault results in an incorrect estimation of the longitudinal tire force for that wheel. Therefore, the total longitudinal force residual ($R_{\Sigma F_x}$) will exceed a predefined threshold:

$$R_{\Sigma F_x} = \left|\left(\hat{F}_{xfl} + \hat{F}_{xfr}\right)\cos(\delta) + \hat{F}_{xrl} + \hat{F}_{xrr} - ma_x\right| \tag{5-12}$$

Similar to the previous chapters, the residual processor computes the fault bounds ($B_{s_{Fx}}, B_{d_{Fx}}$), the adaptive threshold (T_{d,F_x}), time window (W_{F_x}), fault state counter (n_{F_x}) and checks the persistency against the fault state window size (N_{F_x}). If the residual $R_{\Sigma F_x}$ is above the thresholds and the persistence is confirmed, the fault state flag (S_{F_x}) is set to one.

To isolate the fault, four additional residuals ($R_{\tau_{ij}}$) are defined which compare the command torque (τ_{ijc}) and the feedback torque (τ_{ijs}) reported by the sensor:

$$R_{\tau_{ij}} = \left|\tau_{ijc} - \tau_{ijs}\right| \qquad ij \in \{fl, fr, rl, rr\} \tag{5-13}$$

In normal conditions with no faults, the feedback from the motor is equal to the driver's command and $R_{\tau_{ij}}$ is below a threshold $T_{d,\tau}$. A mismatch between the command torque and the feedback torque can have two underlying reasons:

1) Torque sensors are healthy, but a motor is applying a different torque than commanded: in this situation, since the sensed torques are correct and the estimated longitudinal forces by the observers are still accurate, the main total longitudinal force residual ($R_{\Sigma F_x}$) will still be below its threshold. Therefore, the algorithm won't detect a motor fault and avoids false positives.

2) Torque sensor for the ij motor is faulty: in this situation, since the estimated $\hat{F}_{xij}$ using the faulty torque signal is not accurate, both the total longitudinal force residual ($R_{\Sigma F_x}$) and the corresponding motor torque residual ($R_{\tau_{ij}}$) exceed their thresholds. Therefore, the algorithm can identify the faulty sensor (τ_{ijs}) and set its corresponding fault state ($S_{\tau_{ij}}$) to one.

Table 5.1 summarizes the decision logic and the signal reconstruction method. For the fault state vector $\mathcal{S} = \left[S_{\tau_{fl}}\ S_{\tau_{fr}}\ S_{\tau_{rl}}\ S_{\tau_{rr}}\ S_{\Sigma Fx}\right]^T$ and the fault vector $\mathcal{F} = \left[\mathcal{F}_{\tau_{fl}}\ \mathcal{F}_{\tau_{fl}}\ \mathcal{F}_{\tau_{fl}}\ \mathcal{F}_{\tau_{fl}}\right]^T$, the fault signature matrix is obtained as:

$$G = \begin{bmatrix} 1 & 0 & 0 & 0 \\ 0 & 1 & 0 & 0 \\ 0 & 0 & 1 & 0 \\ 0 & 0 & 0 & 1 \\ 1 & 1 & 1 & 1 \end{bmatrix} \tag{5-14}$$

which satisfies the detectability, complete detectability and isolability conditions.

When a torque sensor fault is detected, the fault is reconstructed using the estimated forces from the other healthy sensors and the longitudinal dynamics of the vehicle. If there is no fault, all observers operate normally, receive the sensed torque for their wheel and deliver the estimation of longitudinal tire force for their corresponding tire. If a torque sensor is diagnosed as faulty, then the reconstructed torque from Table 5.1 is fed to the impacted observer to achieve the fault-tolerant estimation of the longitudinal tire force for that tire.

Table 5.1. Decision logic for detection of torque sensor faults and reconstruction of faulty signals

Faulty Sensor	Residuals Above Thresholds	Fault State Flag	Reconstructed Motor Torque Signal
τ_{fls}	$R_{\tau_{fl}}$ *and* $R_{\Sigma F_x}$	$S_{\tau_{fl}}$	$\hat{\tau}_{fl} = I\dot{\omega}_{fl} + \frac{r_e}{\cos(\delta)}\left[ma_{x_s} - \left(\hat{F}_{xfr}\cos(\delta) + \hat{F}_{xrl} + \hat{F}_{xrr}\right)\right]$
τ_{frs}	$R_{\tau_{fr}}$ *and* $R_{\Sigma F_x}$	$S_{\tau_{fr}}$	$\hat{\tau}_{fr} = I\dot{\omega}_{fr} + \frac{r_e}{\cos(\delta)}\left[ma_{x_s} - \left(\hat{F}_{xfl}\cos(\delta) + \hat{F}_{xrl} + \hat{F}_{xrr}\right)\right]$
τ_{rls}	$R_{\tau_{rl}}$ *and* $R_{\Sigma F_x}$	$S_{\tau_{rl}}$	$\hat{\tau}_{rl} = I\dot{\omega}_{rl} + r_e\left[ma_{x_s} - \left(\hat{F}_{xfl}\cos(\delta) + \hat{F}_{xfr}\cos(\delta) + \hat{F}_{xrr}\right)\right]$
τ_{rrs}	$R_{\tau_{rr}}$ *and* $R_{\Sigma F_x}$	$S_{\tau_{rr}}$	$\hat{\tau}_{rr} = I\dot{\omega}_{rr} + r_e\left[ma_{x_s} - \left(\hat{F}_{xfl}\cos(\delta) + \hat{F}_{xfr}\cos(\delta) + \hat{F}_{xrl}\right)\right]$
None	$R_{\Sigma F_x}$ *or* None	N/A	None

5.3 Fault-Tolerant Estimation of Vertical Tire Forces

Vertical tire forces acting on each wheel were formulated in chapter 4 as functions of the longitudinal, lateral and vertical accelerations as well as roll and pitch angles:

$$\hat{F}_{zij} = f\left(a_{x_s}, a_{y_s}, a_{z_s}, \theta_v, \phi_v\right) \tag{5-15}$$

Consequently, these estimated forces are sensitive to the longitudinal, lateral and vertical acceleration sensor faults. Moreover, since suspension height and roll/pitch rate sensor faults impact estimation of roll and pitch angles, the vertical tire forces are also impacted by these sensor faults.

To obtain fault-tolerant estimation of the vertical tire forces, the reconstructed acceleration signals from Chapter 4 ($\hat{a}_{x_s}, \hat{a}_{y_s}, \hat{a}_{z_s}$) and fault-tolerant estimations of roll/pitch angles from Chapter 3 ($\hat{\theta}_v, \hat{\phi}_v$) are fed to the vertical force estimator. Figure 5.3 summarizes this process.

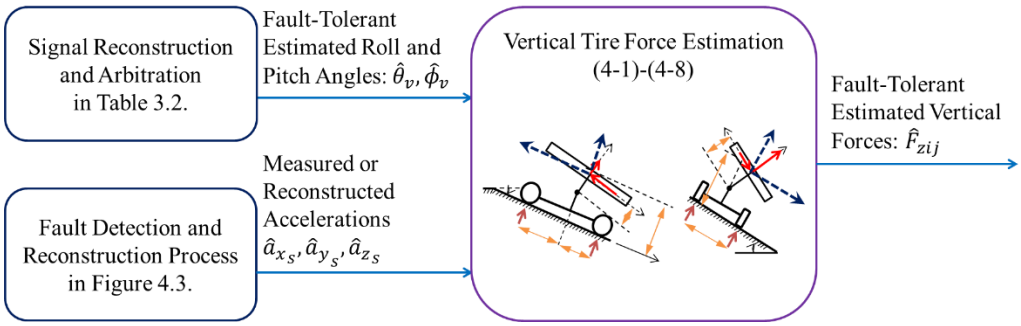

Figure 5.3. Fault-tolerant estimation of vertical tire forces

It is noteworthy that the proposed approach can be extended to other vertical tire force estimation methods available in the literature. As an example, in [102] suspension deflections and corner stiffness/damping coefficients are used to estimate the vertical tire force for each corner. The reconstructed suspension height signals from this thesis can be fed into the vertical tire force estimation method in [102] to obtain fault-tolerant estimation of the corner vertical forces.

5.4 Fault-Tolerant Estimation of Lateral Tire Forces

An adaptive unscented Kalman filter is designed here for fault-tolerant estimation of lateral tire forces. UKF does not require calculation of the Jacobian matrix and linearization of the system around operating points. This is the main benefit of UKF compared to other available methods for nonlinear state estimation such as extended Kalman filter (EKF).

To design the estimator, first lateral tire forces on the front and rear axles are approximated based on the distribution of vertical tire forces [97]:

$$\hat{F}_{yf,a} = \frac{\hat{F}_{zfl}+\hat{F}_{zfr}}{\hat{F}_{zfl}+\hat{F}_{zfr}+\hat{F}_{zrl}+\hat{F}_{zrr}} m a_{y_s} \tag{5-16}$$

$$\hat{F}_{yr,a} = \frac{\hat{F}_{zrl}+\hat{F}_{zrr}}{\hat{F}_{zfl}+\hat{F}_{zfr}+\hat{F}_{zrl}+\hat{F}_{zrr}} m a_{y_s} \tag{5-17}$$

In harsh driving maneuvers with high wheel slippage, these approximated latera axle forces ($\hat{F}_{yf,a}$, $\hat{F}_{yr,a}$) are not accurate. To overcome this issue, vehicle handling dynamics is integrated into the estimator to develop a robust scheme for accurate and fault-tolerant estimation of the lateral forces.

A random walk observer method [19] is used here to develop the estimator. The state vector (X) is defined as:

$$X = [x_1\ x_2]^T \tag{5-18}$$

$$x_1 = F_{yf} - \hat{F}_{yf,a} \tag{5-19}$$

$$x_2 = F_{yr} - \hat{F}_{yr,a} \tag{5-20}$$

These states are treated as random signals with an identity dynamics matrix impacted by the process noise vector (w):

$$\dot{X} = I_{2\times 2} w \tag{5-21}$$

The measurement equation is defined as:

$$Y = H(X, U) + v \tag{5-22}$$

where v is the measurement noise, $U = \delta$ is the input, and $H(X, U)$ is the measurement matrix. The measurement vector Y is expressed as:

$$Y = \begin{bmatrix} ma_{x_s} - \left(\hat{F}_{xf}\, cos(\delta) + \hat{F}_{xr} - \hat{F}_{yf,t}\, sin(\delta)\right) \\ ma_{y_s} - \left(\hat{F}_{yf}\, cos(\delta) + \hat{F}_{yr,a} + \hat{F}_{xf}\, sin(\delta)\right) \\ I_z\dot{\psi}_s - \left(\left(\hat{F}_{yf,a}\, cos(\delta) + \hat{F}_{xf}\, sin(\delta)\right) L_f - \hat{F}_{yr,a}\, L_r\right) \end{bmatrix} + v \tag{5-23}$$

Using this measurement and assuming that:

1) Accurate estimations of the longitudinal and vertical tire forces are available from the previous sections $\left(\hat{F}_{xij} = F_{xij},\ \hat{F}_{zij} = F_{zij}\right)$

2) If a sensor fails, an accurate reconstructed signal for that sensor is available from Chapter 4 $\left(\hat{a}_{x_s} = a_{x_s},\ \hat{a}_{y_s} = a_{y_s},\ \hat{\dot{\psi}}_s = \dot{\psi}_s,\ \hat{\delta}_s = \delta_s\right)$

then $H(X, U)$ can be expresses as a function of the states and the input steering angle using Equations (4-9)-(4-11):

$$H(X,\delta) = \begin{bmatrix} -x_1\, sin(\delta) \\ x_1 \cos(\delta) + x_2 \\ x_1\, cos(\delta)\, L_f - x_2 L_r \end{bmatrix} = \begin{bmatrix} -\sin(\delta) & 0 \\ \cos(\delta) & 1 \\ L_f \cos(\delta) & -L_r \end{bmatrix} \begin{bmatrix} x_1 \\ x_2 \end{bmatrix} \tag{5-24}$$

Consequently, the discrete time state-space model can be summarized as:

$$X_k = I_{2\times 2} X_{k-1} + w_k \tag{5-25}$$

$$Y_k = H(X_k, \delta_k) + v_k \tag{5-26}$$

Using this model, the UKF method introduced in [103] and used in [97] is adopted for estimation of lateral tire forces. The algorithm is modified in this thesis to maintain a reliable estimation performance even when a sensor is faulty. The overall process is shown in Figure 5.4. Details about the UKF method are provided in Appendix A.

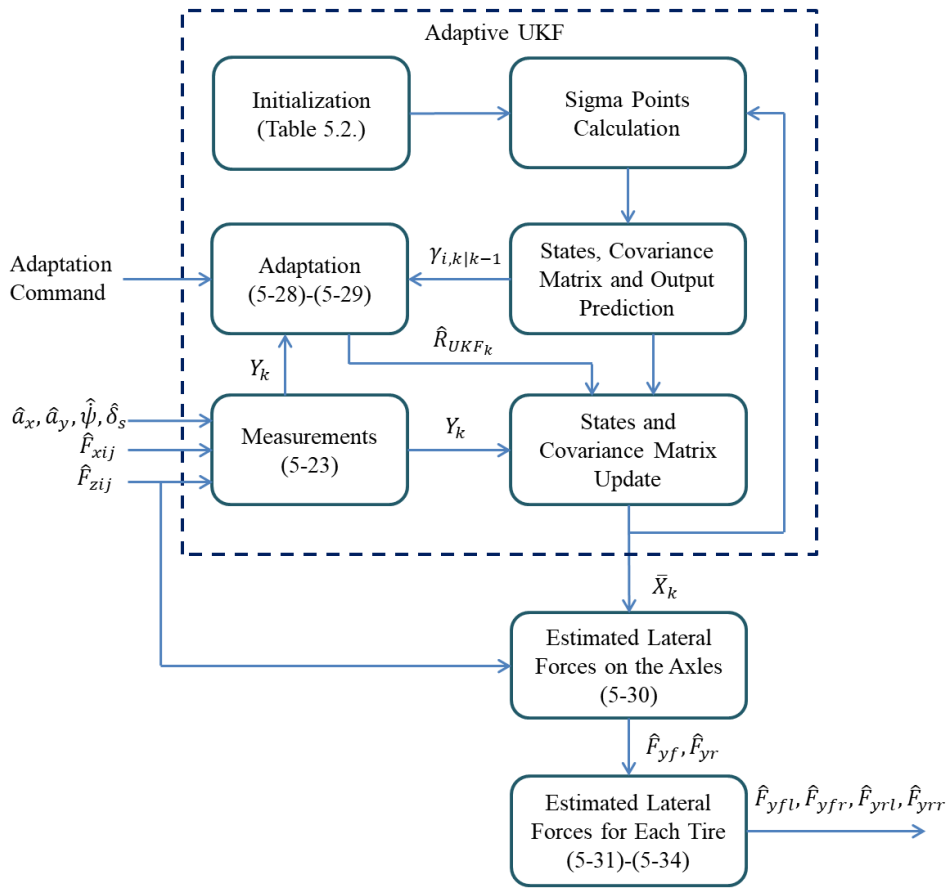

Figure 5.4. Adaptive UKF for fault-tolerant estimation of lateral tire forces

In summary, UKF includes the following three main steps:

1) Calculating a set of carefully chosen weighted sample points, called sigma points, around each state of the system.

2) Predicting the covariance matrix, outputs and states using the sigma points. This prediction is performed using the estimated states and the error covariance matrices from the previous sample time $(k-1)$.

3) Updating the states and covariance matrices using measurements at the current sample time (k) using the sigma points, estimated states from the previous sample time, and the error covariance.

When a sensor fails, the main issue arises in the third step when UKF uses sensor measurements to update the measurement covariance matrix:

$$\mathcal{P}_{\bar{Y}_k\bar{Y}_k} = \sum_{i=0}^{2n} w_i^{(c)} \left(\gamma_{i,k|k-1} - \bar{Y}_{k|k-1} \right) \times \left(\gamma_{i,k|k-1} - \bar{Y}_{k|k-1} \right)^T + \mathcal{R} \tag{5-27}$$

where n is the number of states, $i = 0,2,\dots,2n$ indicates sigma points, $w_i^{(c)}$ is a constant weight for the covariance of sigma points, $\mathcal{P}_{\bar{Y}_k\bar{Y}_k}$ is the innovation covariance, $\bar{Y}_{k|k-1}$ is the predicted output, $\gamma_{i,k|k-1}$ is the predicted measurement and $\mathcal{R}$ is the measurement noise covariance matrix. Normally, $\mathcal{R}$ is a fixed diagonal matrix containing statistical information about the expected sensor noise levels. When the noise characteristic of a sensor changes, the initially set value for $\mathcal{R}$ is no longer valid. Such a change may produce an unstable estimation performance [104].

An approach for adapting the UKF parameters for sensors with time varying noise characteristics is presented in [105]. A similar approach is developed in this thesis to adapt $\mathcal{R}$ when a reconstructed signal is used in the estimation process. The idea is to update $\mathcal{R}$ over a time window and obtain its updated estimate $(\hat{\mathcal{R}})$ after detection of the fault. The updated matrix $\hat{\mathcal{R}}$ is calculated using predicted outputs by the model and the observed measurements:

$$\hat{\mathcal{R}} = \mathcal{C}_k + \sum_{i=0}^{2n} \omega_i^{(c)} \left(\gamma_{i,k|k-1} - \bar{Y}_{k|k-1} \right) \times \left(\gamma_{i,k|k-1} - \bar{Y}_{k|k-1} \right)^T \tag{5-28}$$

$$\mathcal{C}_k = \frac{1}{W} \sum_{j=k-W+1}^{k} \left(Y_j - \bar{Y}_{j|j-1} \right) \times \left(Y_j - \bar{Y}_{j|j-1} \right)^T \tag{5-29}$$

where W represents the time window. After the fault is detected and reconstructed, Equations (5-28) and (5-29) are used to adapt the estimator, maintain stability and achieve a desirable estimation performance.

Using the estimated states from the proposed adaptive UKF ($\bar{X}_k$), lateral tire forces on the axles ($\hat{F}_{yf}, \hat{F}_{yr}$) are obtained from (5-19) and (5-20):

$$\begin{bmatrix} \hat{F}_{yf} \\ \hat{F}_{yr} \end{bmatrix} = \bar{X}_k + \begin{bmatrix} \hat{F}_{yf,a} \\ \hat{F}_{yr,a} \end{bmatrix} \tag{5-30}$$

Lateral tire forces on each wheel are then calculated by distributing the axle forces between the left and right tires considering the load transfer effects:

$$\hat{F}_{yfl} = \frac{\hat{F}_{zfl}}{\hat{F}_{zfr}+\hat{F}_{zfl}} \hat{F}_{yf} \tag{5-31}$$

$$\hat{F}_{yfr} = \frac{\hat{F}_{zfr}}{\hat{F}_{zfr}+\hat{F}_{zfl}} \hat{F}_{yf} \tag{5-32}$$

$$\hat{F}_{yrl} = \frac{\hat{F}_{zrl}}{\hat{F}_{zrr}+\hat{F}_{zrl}} \hat{F}_{yr} \tag{5-33}$$

$$\hat{F}_{yrr} = \frac{\hat{F}_{zrr}}{\hat{F}_{zrr}+\hat{F}_{zrl}} \hat{F}_{yr} \tag{5-34}$$

where $\hat{F}_{zij}$ is the estimated vertical tire force from the previous section and $\hat{F}_{yij}$ are the estimated lateral tire forces for each wheel.

5.5 Fault-Tolerant Estimation of Longitudinal and Lateral Velocities

A method to estimate the longitudinal velocity was discussed in Chapter 4. The same estimator is used here and is fed with the reconstructed longitudinal acceleration signal ($\hat{a}_{x_s}$) and the reconstructed yaw rate signal in the transformation ($v_{x_{CG\leftarrow ij}}$) when any of these sensors are faulty:

$$\dot{\hat{v}}_x = \hat{a}_{x_s} - gsin(\hat{\theta}_v + \hat{\Theta}_r) + \sum K_{v_x}(\hat{a}_x, \omega_{ij})(v_{x_{CG\leftarrow ij}} - \hat{v}_x) \tag{5-35}$$

For estimation of the lateral velocity, the kinematic relation between the lateral states is considered, the reconstructed lateral acceleration and yaw rate signals are fed to this kinematics, and lateral velocity is obtained as:

$$\hat{v}_y = \int (\hat{a}_{y_s} - gsin\big(\hat{\phi}_v + \hat{\Phi}_r\big) - \hat{\dot{\psi}}_s \hat{v}_x) dt \tag{5-36}$$

More comprehensive methods for estimation of lateral velocity are available in the literature [99][106]. These methods can be fed with the reconstructed signals from this thesis to deliver a more precise estimation in presence of the sensor faults.

5.6 Unified Structure for Fault-Tolerant Estimation of Vehicle States

Several fault detection, signal reconstruction and fault-tolerant estimation modules were discussed in this thesis. The unified structure that connects these modules is illustrated in Figure 5.5.

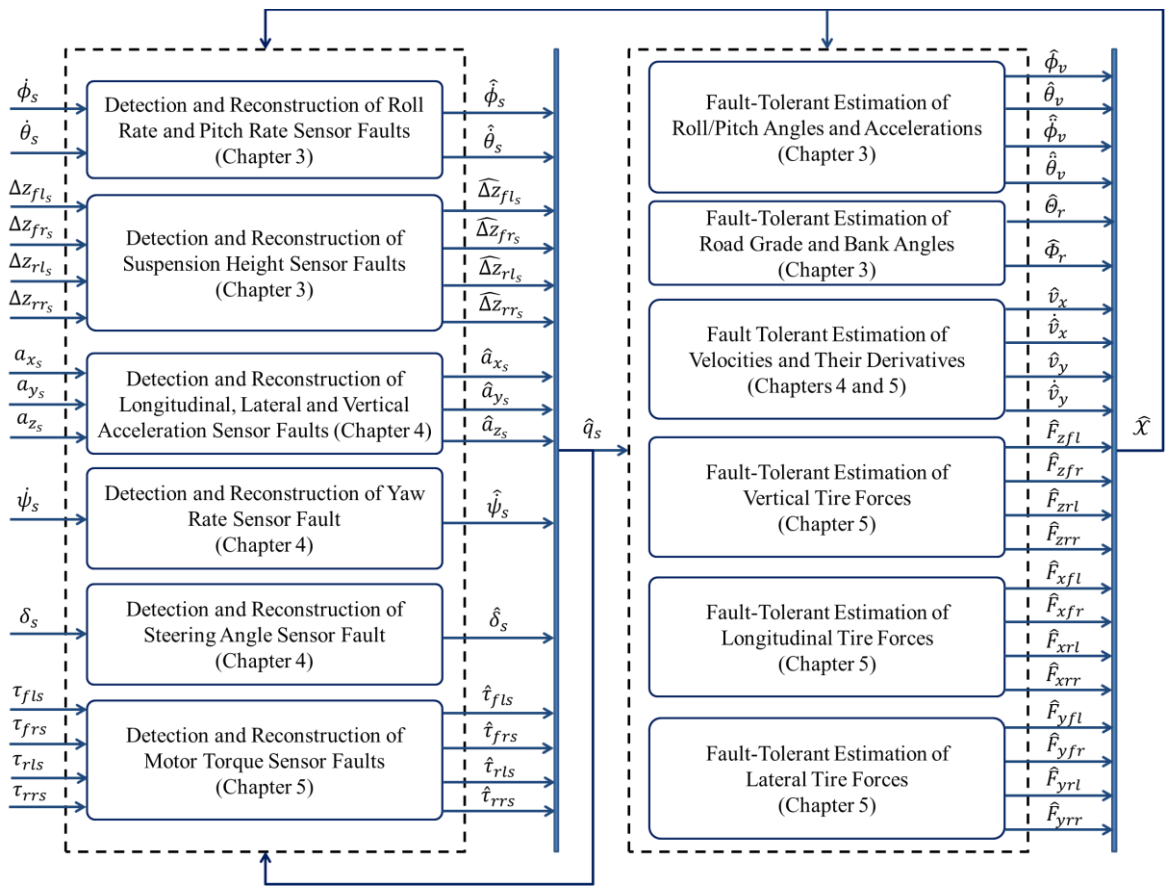

Figure 5.5. Unified structure for sensor fault detection, signal reconstruction and fault-tolerant estimation of vehicle states

In this structure, any sensor measurement q_s is first received by a single module ($q_s \in \left\{a_{x_s}, a_{y_s}, a_{z_s}, \dot{\psi}_s, \dot{\phi}_s, \dot{\theta}_s, \Delta z_{fl_s}, \Delta z_{fr_s}, \Delta z_{rl_s}, \Delta z_{rr_s}, \tau_{fls}, \tau_{frs}, \tau_{rls}, \tau_{rrs}, \delta_s\right\}$). The receiving module diagnoses the sensory signal and produces the corresponding $\hat{q}_s$ as the output ($\hat{q}_s \in \left\{\hat{a}_{x_s}, \hat{a}_{y_s}, \hat{a}_{z_s}, \hat{\dot{\psi}}_s, \hat{\dot{\phi}}_s, \hat{\dot{\theta}}_s, \widehat{\Delta z}_{fl_s}, \widehat{\Delta z}_{fr_s}, \widehat{\Delta z}_{rl_s}, \widehat{\Delta z}_{rr_s}, \hat{\tau}_{fls}, \hat{\tau}_{frs}, \hat{\tau}_{rls}, \hat{\tau}_{rrs}, \hat{\delta}_s\right\}$). As discussed before, each $\hat{q}_s$ contains the actual sensor measurement if there is no fault, and contains the reconstructed signal when the sensor is faulty.

Consequently, the fault-tolerant estimators in this thesis either receive the healthy sensory data or the reconstructed signal and deliver accurate estimation of states $(\hat{\mathcal{X}})$ even when a sensor is faulty ($\hat{\mathcal{X}} \in \{\hat{\phi}_v, \hat{\theta}_v, \hat{\dot{\phi}}_v, \hat{\dot{\theta}}_v, \hat{\Phi}_r, \hat{\Theta}_r, \hat{v}_x, \hat{\dot{v}}_x, \hat{v}_y, \hat{\dot{v}}_y, \hat{F}_{xfl}, \hat{F}_{xfr}, \hat{F}_{xrl}, \hat{F}_{xrr}, \hat{F}_{yfl}, \hat{F}_{yfr}, \hat{F}_{yrl}, \hat{F}_{yrr}, \hat{F}_{zfl}, \hat{F}_{zfr}, \hat{F}_{zrl}, \hat{F}_{zrr}\}$).

5.7 Experiment Results

Several experimental case studies are conducted to verify the effectiveness of the proposed fault-tolerant estimation structure. Figure 5.6 shows the complete test setup for these experiments.

Figure 5.6. Vehicle sensors, actuators and instrumentations for verification of the results

Four electric motors from the Amp Motors Company are installed to provide independent traction to the four wheels. Driver's accelerator pedal command is processed in the dSPACE Autobox controller and is commanded to the motors through the CAN communication channel. To verify the fault-tolerant tire force estimation results, wheel load measurement devices from the Michigan Scientific Corporation

are mounted on each wheel. These devices measure the longitudinal, lateral, and vertical forces and moments acting on the center of each wheel. Calibration and signal conditioning for the load wheel measurement sensors is performed using the load wheel interface system. Steering wheel angle of the vehicle is available from the vehicle's stock steering encoder. Steering angle of the front wheels is obtained from the stock steering wheel angle sensor and the reduction ratio of the steering mechanism. Angular velocity of each wheel is available from the stock encoders. The fault-tolerant estimation algorithm is compiled and run in the Autobox controller. Sampling rate for the sensor data and execution rate of the embedded code is set at 200 Hz.

Parameters of the UKF algorithm are summarized in Table 5.2. Definition of these parameters are provided in Appendix A. The parameters are tuned using the guidelines suggested in [107]. The rest of the fault-tolerant estimation parameters used in the experiments are summarized in Table 5.3.

Table 5.2. UKF parameters

Parameter	Value	Parameter	Value
n	2	X_0	$[0\ 0]^T$
α	0.8	$\mathcal{Q}$	$10^{-2}I_{2\times2}$
ϵ	0.5	$\mathcal{R}_0$	$10^{-4}I_{3\times3}$
β	2	$\mathcal{P}_0$	$10^{5}I_{2\times2}$

Table 5.3. Parameters for residual processing and fault-tolerant estimation

Parameter	Value	Parameter	Value
K_P	150	$B_{s_{Fx}}$	0.01
K_D	5	$B_{d_{Fx}}$	0.0015
K_I	0.001	N_{Fx}	100
Λ	50	W_{Fx}	500

5.7.1 Experiment Results when all Sensors are Functional

Performance of the proposed structure is first studied when all sensors are functioning properly. Tire force estimation results during the same step-steer with acceleration and braking maneuver as in Section 4.11.1 are presented here. Driver commands and the vehicle trajectory are shown in Figure 5.7.

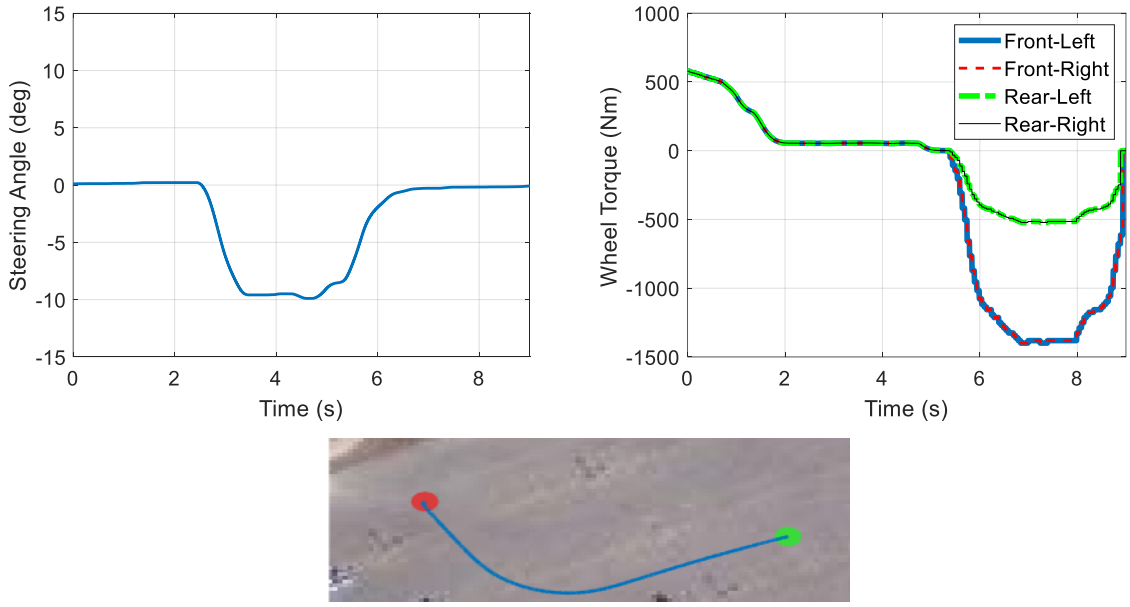

Figure 5.7. Driver commands and trajectory of the vehicle during the step-steer maneuver with no sensor fault

Figure 5.8, Figure 5.9 and Figure 5.10 show the results for estimation of longitudinal, lateral and vertical tire forces, respectively. The results confirm that estimated tire forces match the measurements from the wheel load sensors for all wheels. The estimation errors are summarized in Table 5.4. The maximum NRMSE is 10.98% for longitudinal tire forces, 12.02% for lateral tire forces and 4.48% for vertical tire forces. The results demonstrate that the tire forces are estimated successfully despite the aggressive steering and harsh acceleration/braking commands during the maneuver.

Table 5.4. Tire force estimation errors when there is no sensor fault

Estimated Force	NRMSE	Estimated Force	NRMSE	Estimated Force	NRMSE
$\hat{F}_{xfl}$	8.20 %	$\hat{F}_{yfl}$	6.40 %	$\hat{F}_{zfl}$	3.09 %
$\hat{F}_{xfr}$	4.85 %	$\hat{F}_{yfr}$	11.33 %	$\hat{F}_{zfr}$	4.48 %
$\hat{F}_{xrl}$	7.41 %	$\hat{F}_{yrl}$	7.95 %	$\hat{F}_{zrl}$	3.88 %
$\hat{F}_{xrr}$	10.98 %	$\hat{F}_{yrr}$	12.02 %	$\hat{F}_{zrr}$	4.39 %

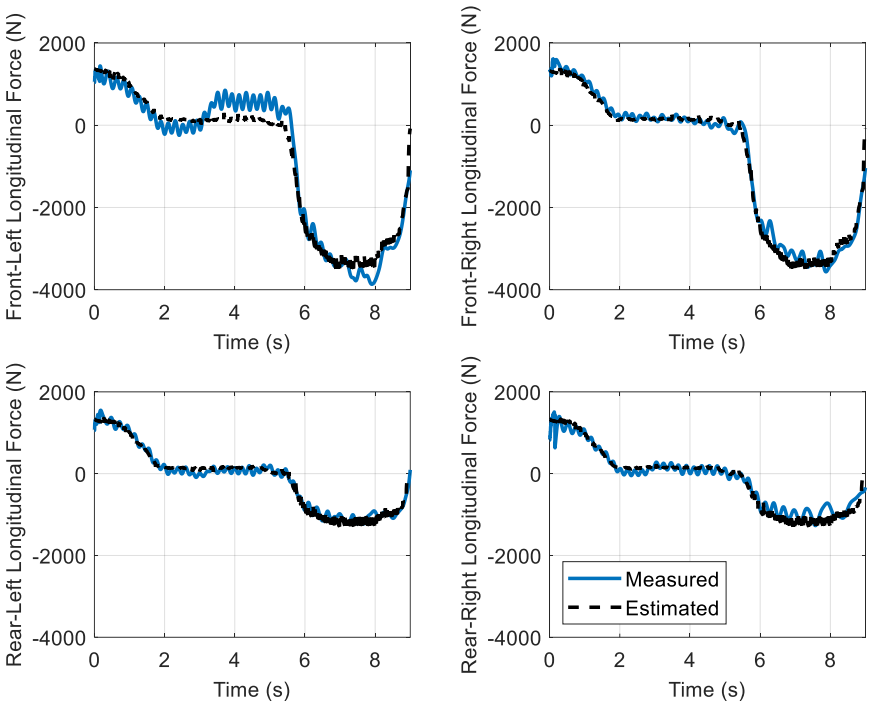

Figure 5.8. Estimation of longitudinal tire forces when there is no sensor fault

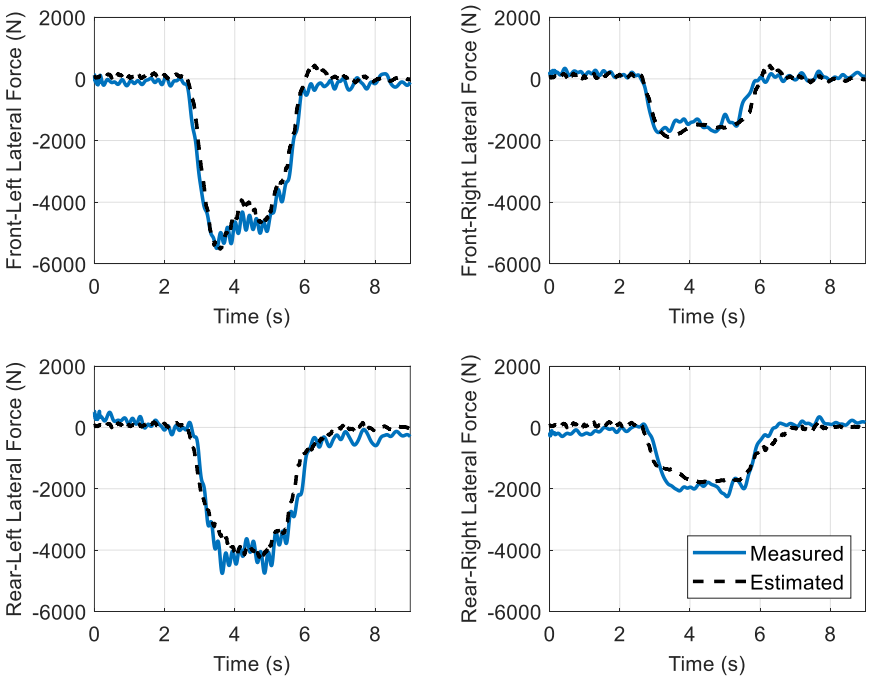

Figure 5.9. Estimation of lateral tire forces when there is no sensor fault

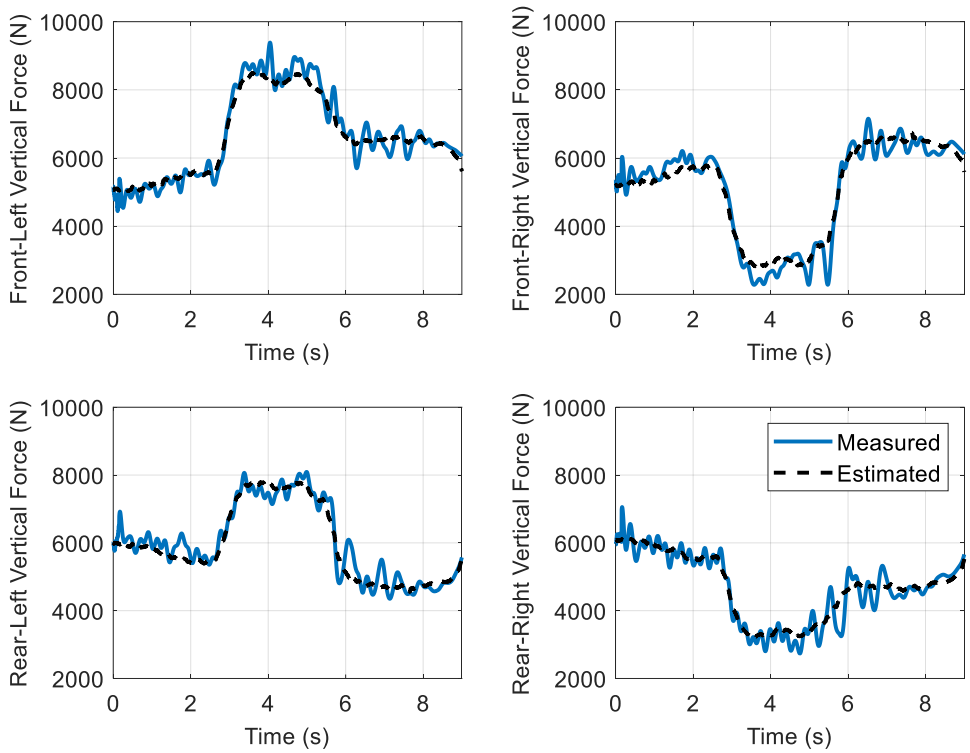

Figure 5.10. Estimation of vertical tire forces when there is no sensor fault

5.7.2 Fault-Tolerant Estimation of States When Lateral Acceleration Sensor is Faulty

Failure of the lateral acceleration sensor impacts the estimation of vertical tire forces, lateral tire forces and lateral velocity of the vehicle. For this case strudy, the vehicle performs a DLC maneuver which starts on a wet sealer ($\mu \approx 0.4$) and transitions to a dry pavement ($\mu \approx 0.9$). Driver's steering wheel command, wheel torque commands and trajectory of the vehicle are shown in Figure 5.11. The vehicle is first harshly accelerated to the speed of 55 kph and then the DLC maneuver is executed.

Lateral acceleration sensor fault is injected at $t = 2s$ by replacing the measured lateral acceleration with a zero signal for the rest of the maneuver. Figure 5.12. compares the reconstructed lateral acceleration signal with the actual lateral acceleration of vehicle and the faulty signal. The fault is detected by the algorithm at $t = 2.15s$ and is reconstructed for the rest of the maneuver. NRMSE of the reconstructed signal is 7.07% in this case study. The actual lateral acceleration is between -7.95 and $+6.86$ which verifies that the vehicle is operating in the nonlinear region. The result shows that the signal is successfully reconstructed despite the harsh lateral excitation and nonlinearities.

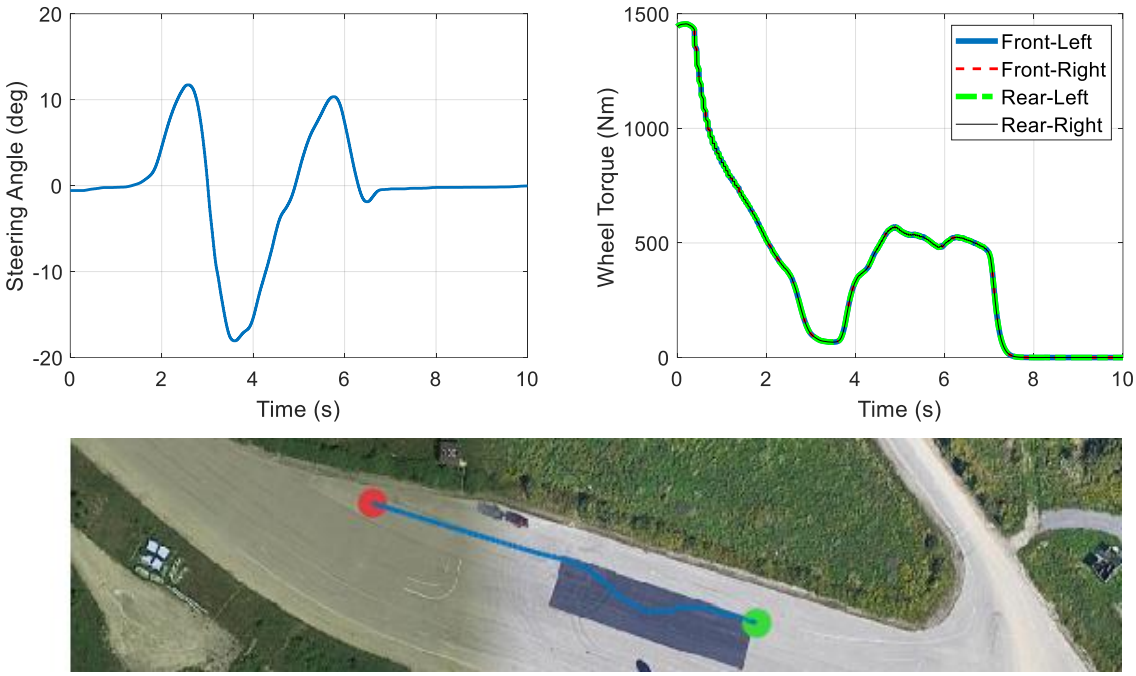

Figure 5.11. Driver commands and trajectory of the vehicle during the DLC maneuver with lateral acceleration sensor fault

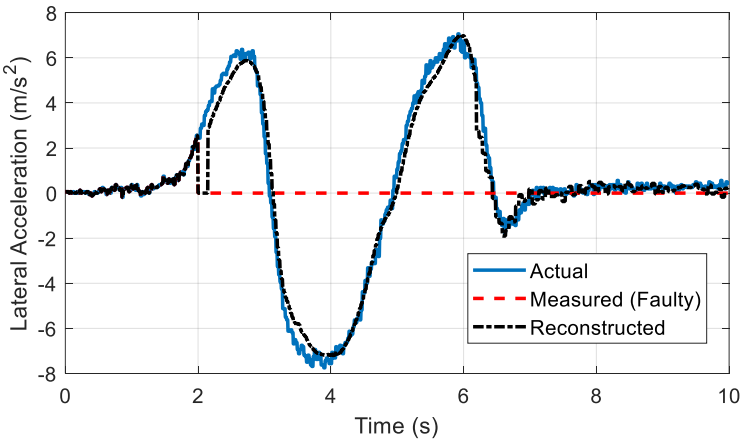

Figure 5.12. Reconstruction of the faulty lateral acceleration signal

Experiment results for fault-tolerant estimation of vertical tire forces are shown in Figure 5.13. For each wheel, the fault-tolerant estimated force is compared with the following signals:

- The measured vertical tire force from the wheel load measurement sensors

- The estimated vertical tire forces when the estimation algorithm uses the faulty lateral acceleration sensor instead of the reconstructed signal (i.e., no fault tolerance).

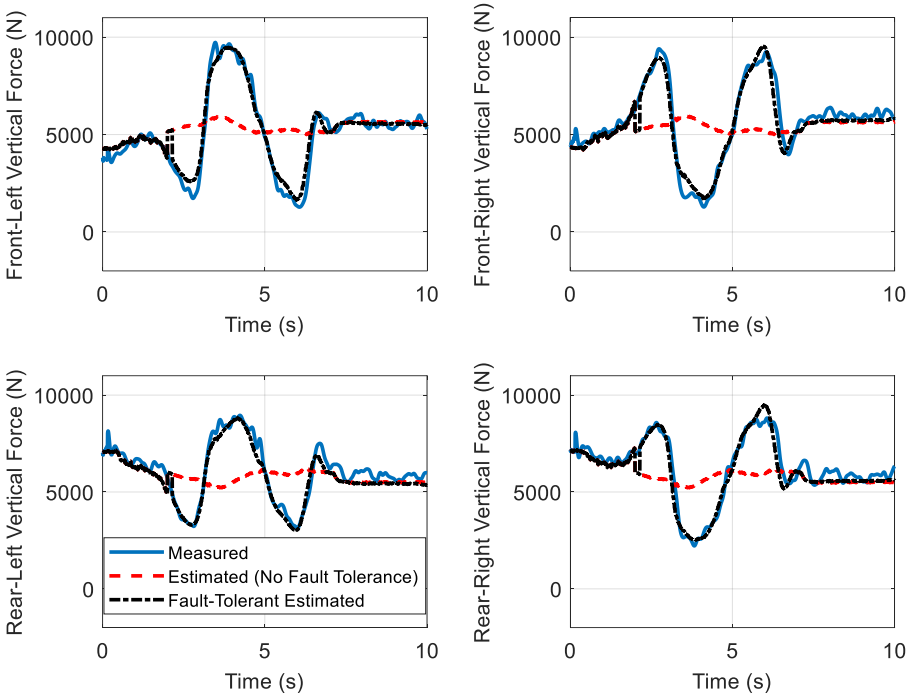

Figure 5.13. Fault-tolerant estimation of vertical tire forces when lateral acceleration sensor fails

Before the fault occurs, the estimation results are identical with and without fault tolerance, as expected. After the fault occurs, the estimator with no fault tolerance doesn't receive accurate information about the lateral acceleration of vehicle and therefore fails to comprehend the lateral load transfer between the left and right wheels. Consequently, its estimation results show large errors when the vehicle performs the lane change maneuver. On the other hand, the fault-tolerant estimator continues to deliver accurate estimations of the vertical tire forces as soon as the fault is detected and reconstructed.

Experiment results for fault-tolerant estimation of lateral tire forces are shown in Figure 5.14. The results illustrate that without fault-tolerance, failure considerably affects the estimation performance. This is expected since the lateral acceleration measurement plays a crucial role in estimation of lateral tire forces. Meanwhile, the proposed fault-tolerant UKF method continues to reliably estimate the lateral forces after the fault is detected.

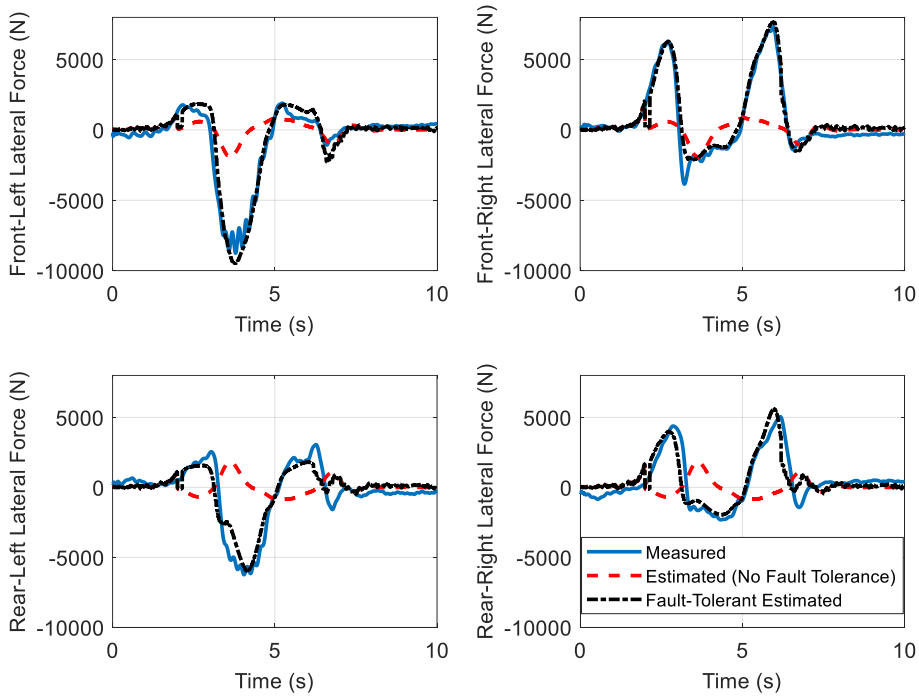

Figure 5.14. Fault-tolerant estimation of lateral tire forces when lateral acceleration sensor fails

Table 5.5 summarizes the performance of vertical and lateral tire force estimators with and without fault tolerance.

Table 5.5. Vertical and lateral tire force estimation errors when lateral acceleration sensor fails

Estimated Force	NRMSE Without Fault Tolerance	NRMSE With Fault Tolerance	Estimated Force	NRMSE Without Fault Tolerance	NRMSE With Fault Tolerance
$\hat{F}_{zfl}$	22.35 %	4.52 %	$\hat{F}_{yfl}$	29.13 %	8.12 %
$\hat{F}_{zfr}$	24.52 %	5.38 %	$\hat{F}_{yfr}$	35.27 %	8.44 %
$\hat{F}_{zrl}$	18.99 %	4.75 %	$\hat{F}_{yrl}$	45.73 %	14.95 %
$\hat{F}_{zrr}$	19.09 %	5.28 %	$\hat{F}_{yrr}$	47.82 %	17.49 %

Lateral acceleration sensor fault also impacts the estimation of the lateral velocity. Figure 5.15 shows the estimation results. Without fault tolerance, the kinematic estimator produces large errors due to the inaccurate lateral acceleration input. On the other hand, the fault-tolerant estimator mitigates this issue since it uses the reconstructed lateral acceleration signal.

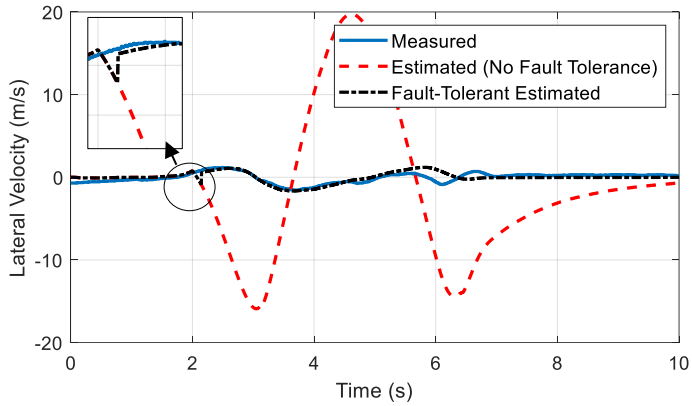

Figure 5.15. Fault-tolerant estimation of lateral velocity when lateral acceleration sensor fails

In this thesis, vehicle roll and pitch angles were estimated using the suspension height and roll/pitch rate sensors and are not impacted by the lateral acceleration sensor fault. For vehicles without active suspension and roll/pitch rate sensors, a common approach in the literature is to estimate the roll/pitch angles as a function of longitudinal/lateral accelerations, assuming roll/pitch rates are small [27]:

$$\hat{\phi}_v = \frac{m_s\, a_{y_s}\, H_{RC}}{K_\phi} \tag{5-37}$$

$$\hat{\theta}_v = -\frac{m_s a_{x_s}\, H_{PC}}{K_\theta} \tag{5-38}$$

Failure of lateral acceleration sensor impacts estimation of roll angle using (5-37). Figure 5.16 shows the results of this estimation approach with and without fault tolerance. The result confirms that the estimator can maintain a desirable performance using the reconstructed lateral acceleration signal.

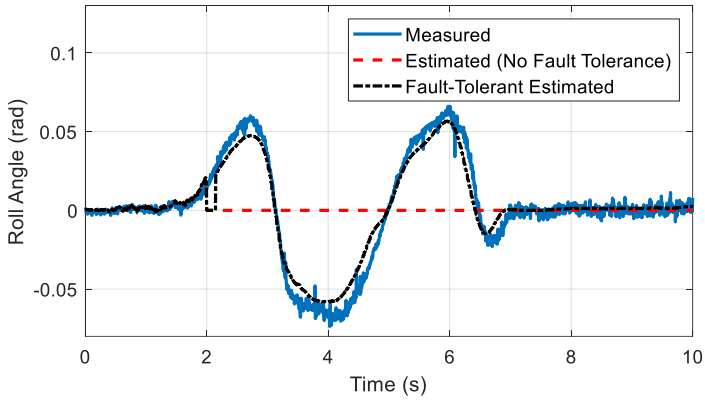

Figure 5.16. Fault-tolerant estimation of roll angle when lateral acceleration sensor fails

5.7.3 Fault-Tolerant Estimation of States When Longitudinal Acceleration Sensor is Faulty

Failure of the longitudinal acceleration sensor mainly impacts the estimation of vertical tire forces and longitudinal velocity of the vehicle. A stop-and-go maneuver on a dry pavement is considered here to evaluate the performance of the proposed method in terms of mitigating the longitudinal acceleration sensor faults. Driver commands for this maneuver are shown in Figure 5.17.

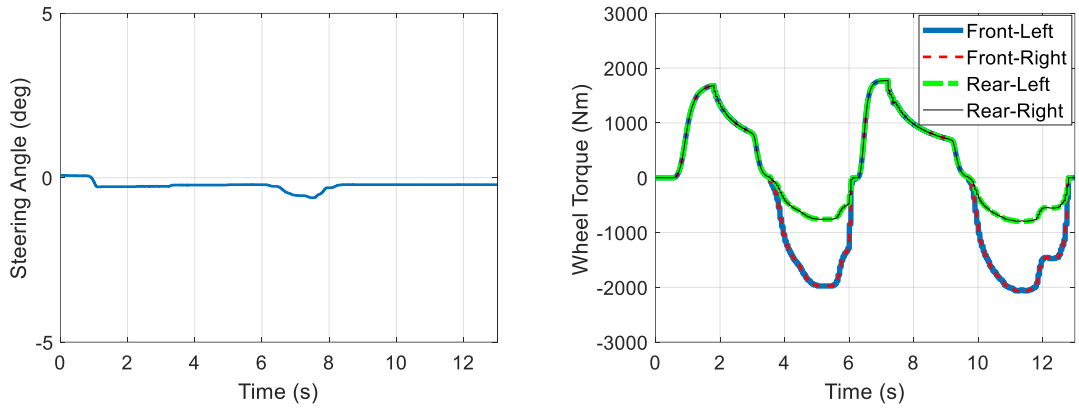

Figure 5.17. Driver commands during the stop-and-go maneuver with longitudinal acceleration sensor fault

A stuck-output sensor fault is injected in this case study such that when the longitudinal acceleration reaches 1 m/s^2, the sensor gets stuck in this value and continues to output this fixed measurement. The fault occurs at $t = 0.89$s in this maneuver. Figure 5.18 shows the reconstruction results. The fault is detected at $t = 1.025s$ and is reconstructed with a NRMSE of 4.43%.

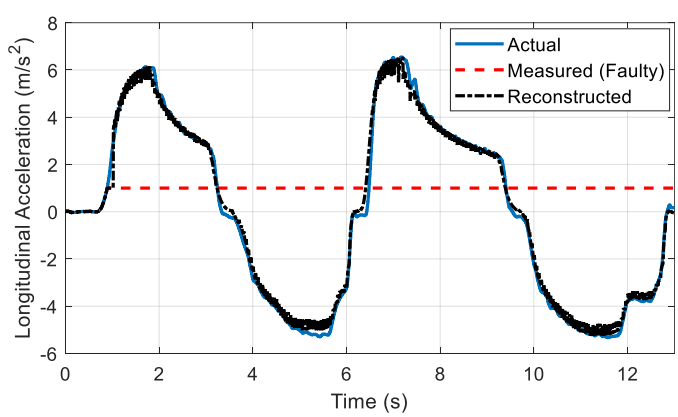

Figure 5.18. Reconstruction of the faulty longitudinal acceleration signal

Experiment results for estimation of vertical tire forces are shown in Figure 5.19. Without fault-tolerance, the estimator fails to comprehend effects of the longitudinal load transfer which leads to large estimation errors when the vehicle is excited in the longitudinal direction. On the other hand, the fault-tolerant estimator delivers a reliable estimation performance despite the sensor fault. Estimation errors are listed in Table 5.6.

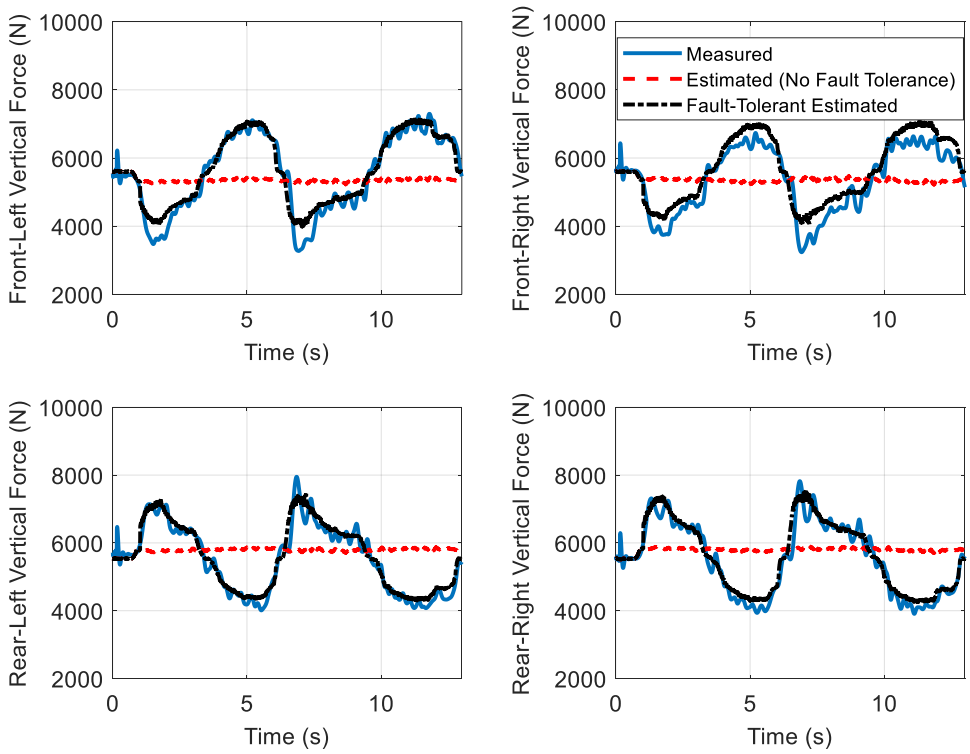

Figure 5.19. Fault-tolerant estimation of vertical tire forces when longitudinal acceleration sensor fails

Table 5.6. Vertical tire force estimation errors when longitudinal acceleration sensor fails

Estimated Force	NRMSE Without Fault Tolerance	NRMSE With Fault Tolerance	Estimated Force	NRMSE Without Fault Tolerance	NRMSE With Fault Tolerance
$\hat{F}_{zfl}$	16.09 %	4.33 %	$\hat{F}_{zrl}$	13.87 %	3.09 %
$\hat{F}_{zfr}$	15.26 %	6.31 %	$\hat{F}_{zrr}$	14.24 %	3.47 %

For vehicles with no suspension height and pitch rate sensors, Equation (5-38) can be used to estimate the pitch angle. Figure 5.20 shows the results of this estimation approach. The result shows that the fault-tolerant estimator can maintain a desirable estimation performance using the reconstructed signal.

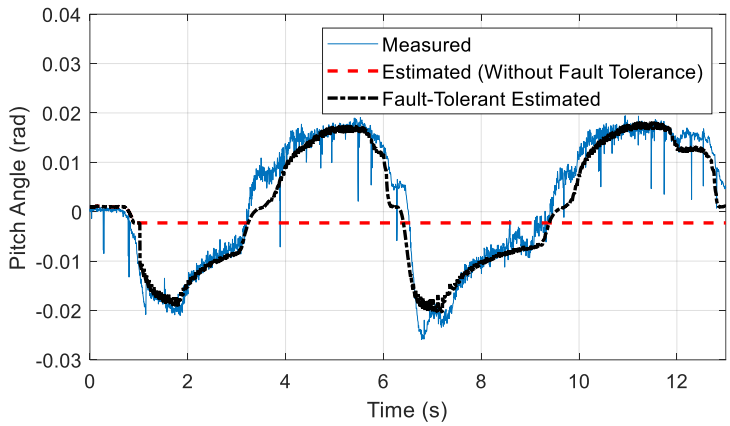

Figure 5.20. Fault-tolerant estimation of pitch angle when longitudinal acceleration sensor fails

For estimation of the longitudinal velocity, the estimator uses longitudinal acceleration of the vehicle as a measurement and therefore is impacted by the sensor fault if not mitigated. Figure 5.21 compares estimation of the longitudinal velocity with and without fault tolerance.

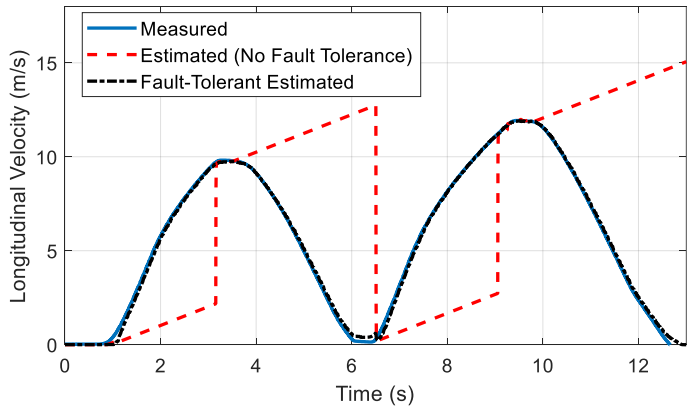

Figure 5.21. Fault-tolerant estimation of longitudinal velocity when longitudinal acceleration sensor fails

If the fault is not mitigated, the observer erroneously detects large wheel slips, excludes all wheel angular velocities from the estimation process and estimates the longitudinal velocity by integrating the failed longitudinal acceleration. Therefore, the estimation result is inaccurate except when the actual

longitudinal acceleration of the vehicle is $1\,m/s^2$ (i.e., when the actual longitudinal acceleration matches the value reported by the faulty sensor). The fault-tolerant estimate is however accurate for the entire maneuver. The NRMSE is 1.49% for the fault-tolerant estimation compared to 59.66% without fault-tolerance.

5.7.4 Fault-Tolerant Estimation of States When Vertical Acceleration Sensor is Faulty

Failure of the vertical acceleration signal impacts performance of the vertical and lateral tire force estimators. A DLC maneuver is performed in this section and a loss of sensitivity fault is injected on the vertical acceleration signal. The sensor reports 50% of the vertical acceleration after $t = 4s$. A torque vectoring controller is active during this maneuver which modifies the driver's torque command to keep the vehicle stable. Driver's steering command and the resultant torque commands (driver plus controller) are shown in Figure 5.21.

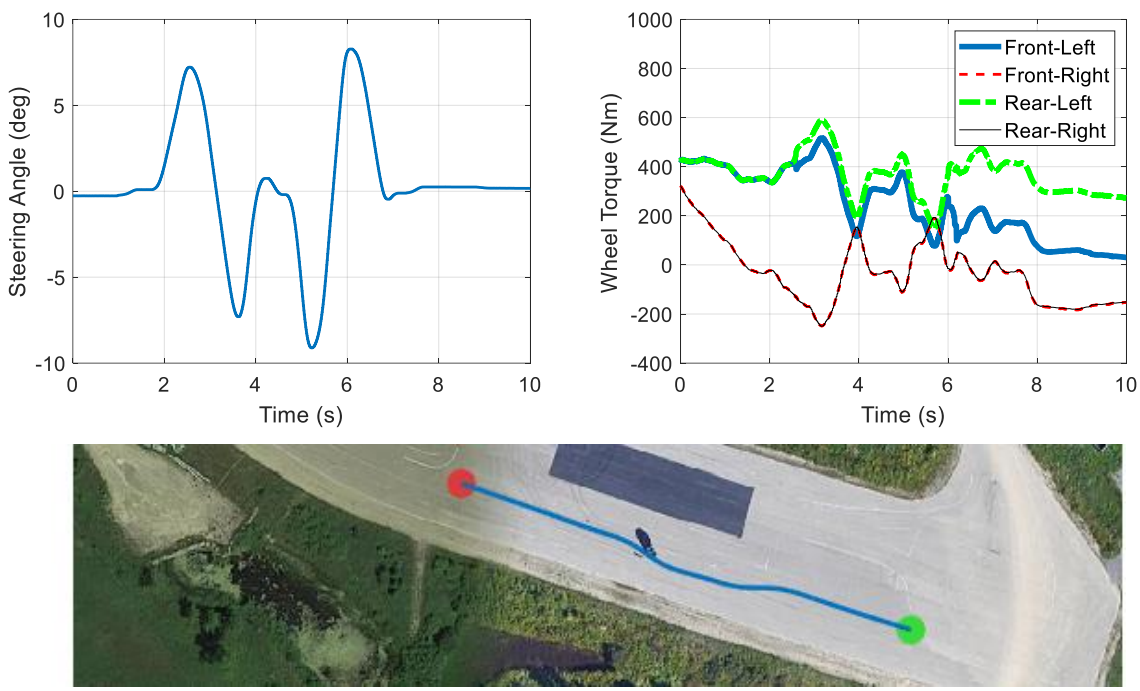

Figure 5.22. Driver and controller commands during the DLC maneuver with vertical acceleration sensor fault

Figure 5.23 shows reconstruction of the faulty vertical acceleration signal. The fault is detected at $t = 4.1s$ and the algorithm reconstructs the failed signal for the rest of the maneuver. The reconstruction NRMSE is 6.05% in this case study.

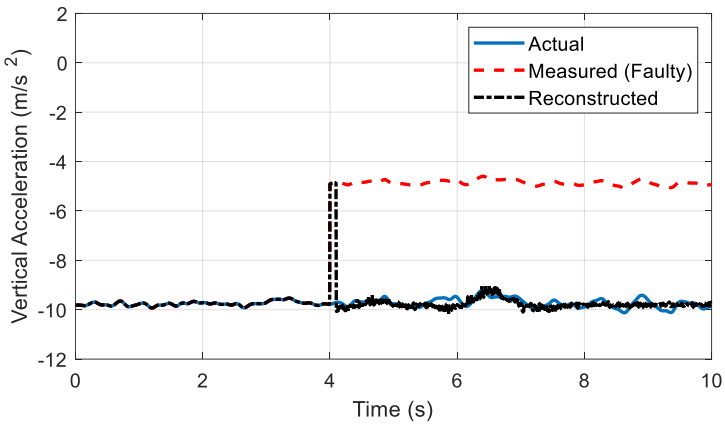

Figure 5.23. Reconstruction of the faulty vertical acceleration signal

The results for fault-tolerant estimation of vertical and lateral tire forces are shown in Figure 5.24 and Figure 5.25, respectively.

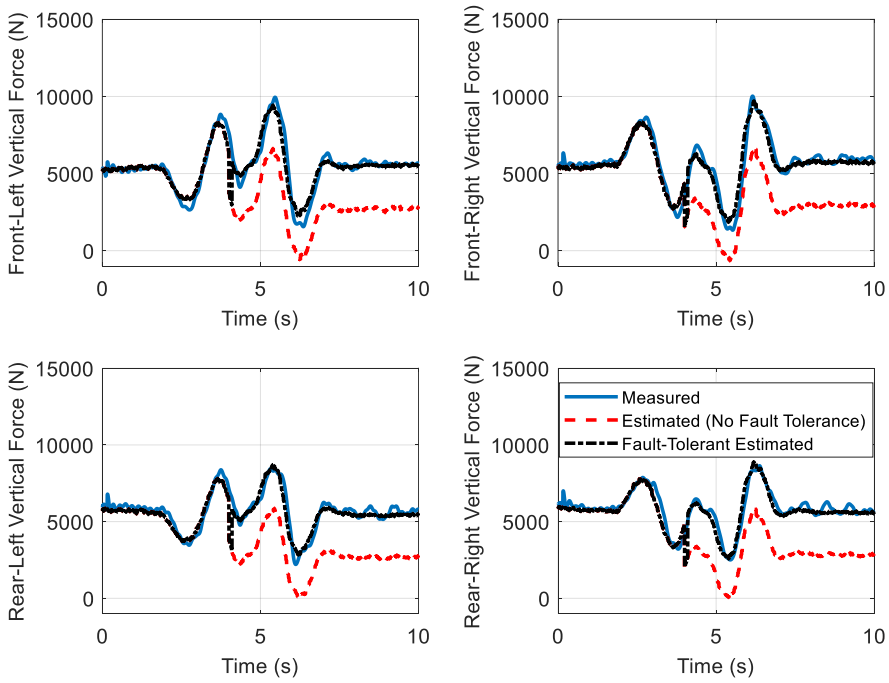

Figure 5.24. Fault-tolerant estimation of vertical tire forces when vertical acceleration sensor fails

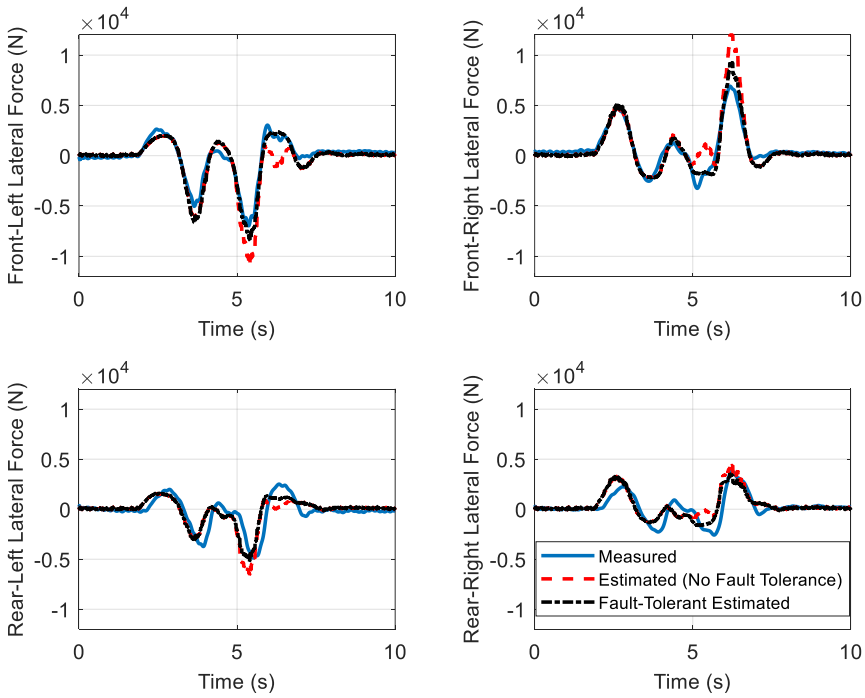

Figure 5.25. Fault-tolerant estimation of lateral tire forces when vertical acceleration sensor fails

Estimation errors are shown in Table 5.7. The results demonstrate that fault-tolerant estimators outperform the estimators with no fault tolerance. The higher lateral force estimation errors in this case study compared to the previous cases are due to the simultaneous occurrence of the fault, the aggressive maneuver and activation of the torque vectoring controller which makes the lateral tire force estimation more challenging.

Table 5.7. Vertical and lateral tire force estimation errors when vertical acceleration sensor fails

Estimated Force	NRMSE Without Fault Tolerance	NRMSE With Fault Tolerance	Estimated Force	NRMSE Without Fault Tolerance	NRMSE With Fault Tolerance
$\hat{F}_{zfl}$	28.96 %	5.42 %	$\hat{F}_{yfl}$	19.51 %	8.80 %
$\hat{F}_{zfr}$	29.38 %	5.41 %	$\hat{F}_{yfr}$	22.27 %	10.16 %
$\hat{F}_{zrl}$	34.52 %	5.12 %	$\hat{F}_{yrl}$	26.91 %	22.53 %
$\hat{F}_{zrr}$	33.92 %	4.59 %	$\hat{F}_{yrr}$	24.80 %	20.95 %

5.7.5 Fault-Tolerant Estimation of States When Yaw Rate Sensor is Faulty

This case study focuses on fault-tolerant estimation of longitudinal and lateral velocities in presence of a yaw rate sensor fault. Figure 5.26 shows the lane change maneuver performed on the wet sealer ($\mu = 0.4$) for this case.

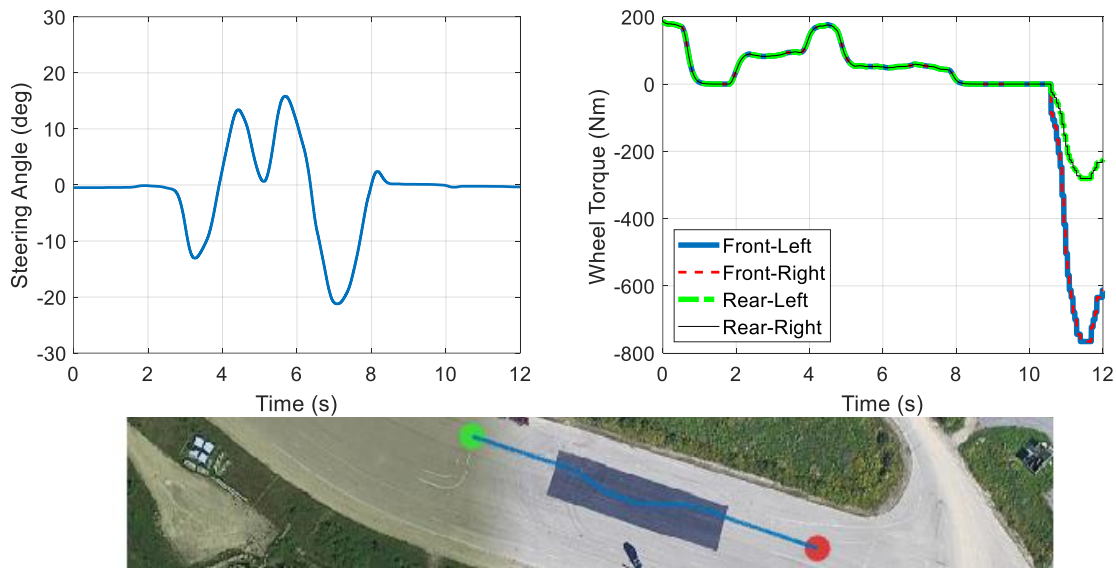

Figure 5.26. Driver commands and trajectory of the vehicle during the DLC maneuver with yaw rate sensor fault

A faulty zero yaw rate signal is injected at $t = 3s$. The algorithm detects the fault at $t = 3.225s$ and reconstructs the signal as shown in Figure 5.27. The NRMSE for reconstruction of the signal is 9.46%.

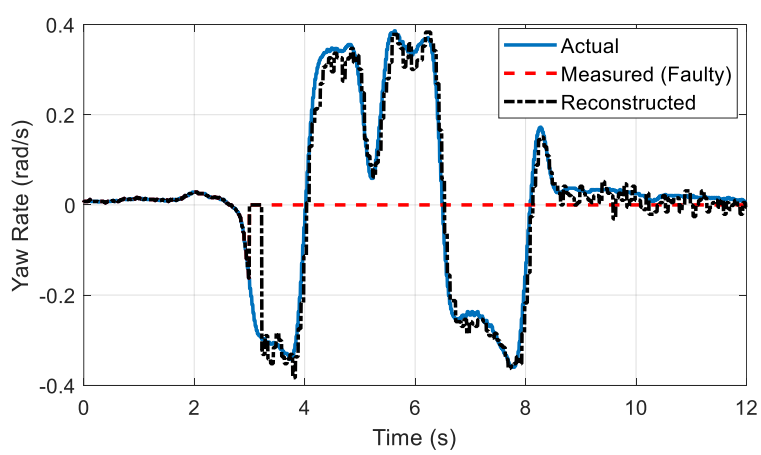

Figure 5.27. Reconstruction of the faulty yaw rate signal

The longitudinal velocity estimator uses the yaw rate to transfer the corner velocities to the CG. Therefore, it is impacted by the yaw rate fault. The experiment result in Figure 5.28 confirms this impact and shows that without fault tolerance the estimator faces difficulties when the vehicle is performing the lane change maneuver. On the other hand, the fault-tolerant estimator can reliably overcome such difficulties and accurately estimate the longitudinal velocity despite the sensor fault.

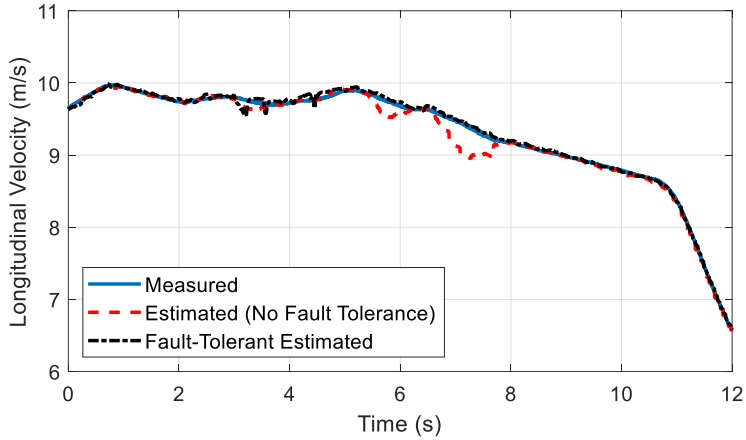

Figure 5.28. Fault-tolerant estimation of longitudinal velocity when yaw rate sensor fails

Similarly, the lateral velocity estimator relies on the yaw rate measurement and is impacted by the yaw rate sensor fault if not mitigated. Figure 5.29 shows the results of this estimator with and without fault tolerance.

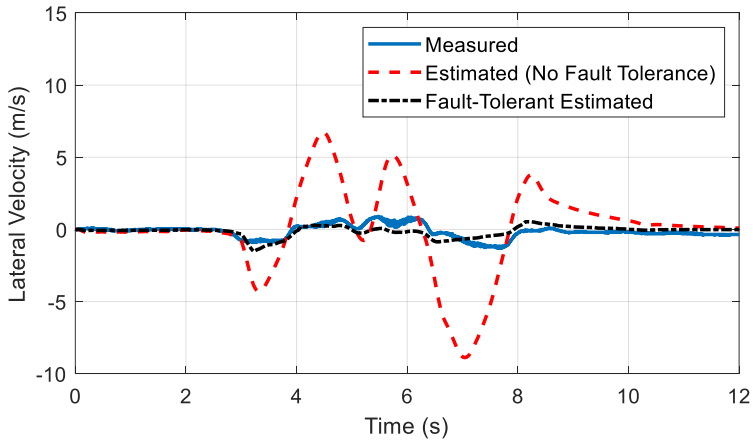

Figure 5.29. Fault-tolerant estimation of lateral velocity when yaw rate sensor fails

5.7.6 Fault-Tolerant Estimation of States When Motor Torque Sensor is Faulty

As the final case study, fault-tolerant estimation of longitudinal tire forces in presence of a motor torque sensor fault is discussed in this section. Driver commands, longitudinal velocity and trajectory of the vehicle for the acceleration and braking maneuver in this case study are shown in Figure 5.30.

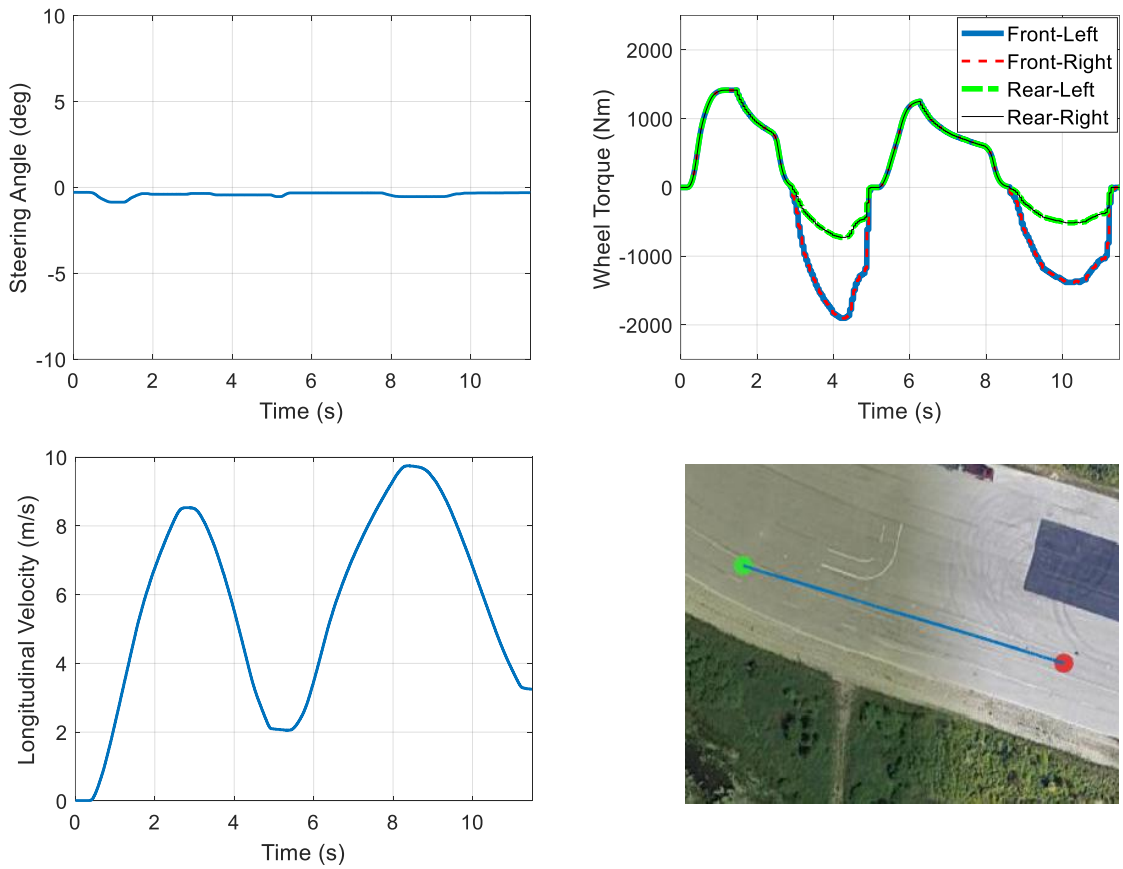

Figure 5.30. Driver commands and trajectory of the vehicle during the acceleration and braking maneuver with motor torque sensor fault

In this maneuver, the front-left torque sensor reports 25% of the actual feedback torque after $t = 1s$. The residual for the total longitudinal force is shown in Figure 5.31 and individual wheels torque residuals are shown in Figure 5.32. The total force residual and the front-left motor torque residual exceed their thresholds as soon as the fault occurs. This indicates failure of the front-left torque sensor according to the decision logic that was discussed in Table 5.1.

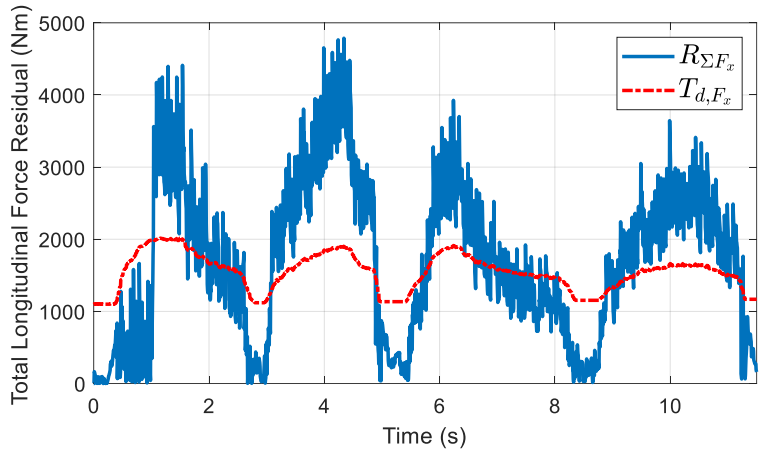

Figure 5.31. Total longitudinal force residual when front-left torque sensor fails

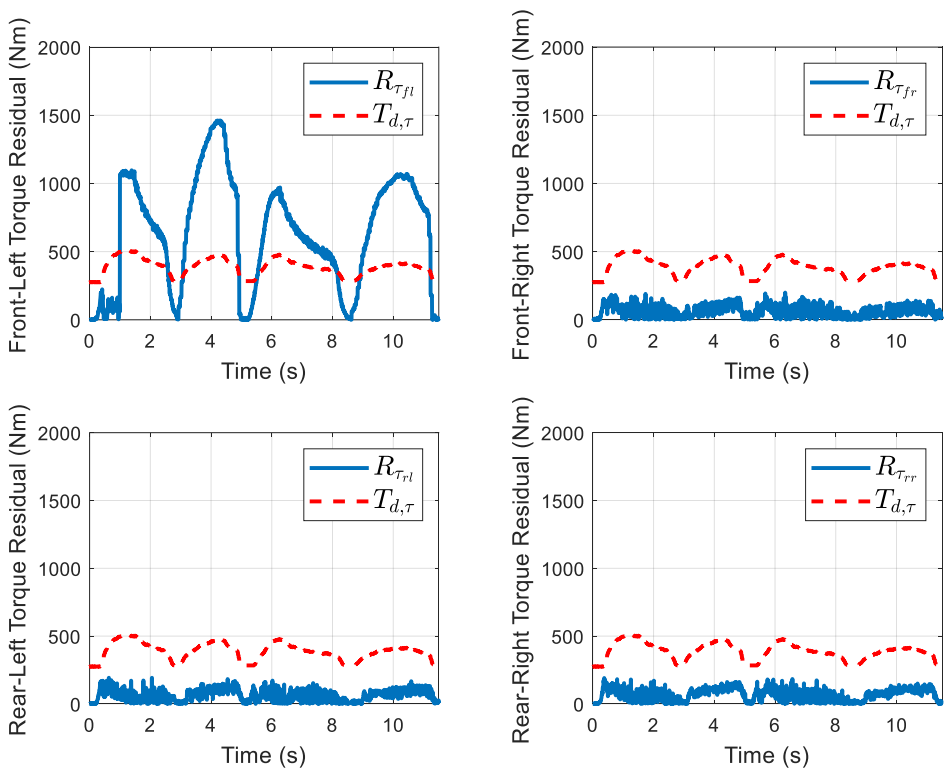

Figure 5.32. Wheel torque residuals when front-left torque sensor fails

Figure 5.33 shows that the proposed algorithm detects the fault at $t = 1.185s$ and correctly estimates the fault magnitude. Reconstruction of the front-left torque signal is shown in Figure 5.34. The faulty signal is successfully reconstructed and the NRMSE of the reconstructed signal is 9.28%.

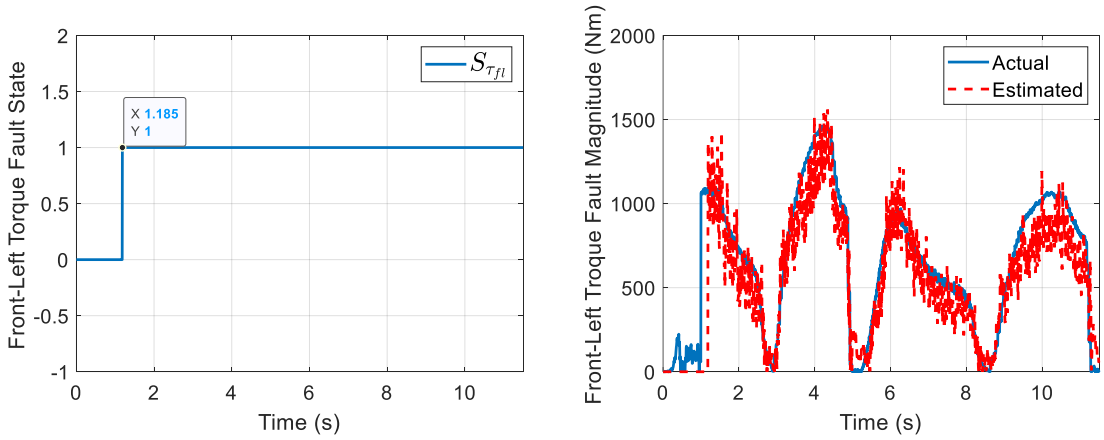

Figure 5.33. Detection of front-left torque sensor fault and estimation of the fault magnitude

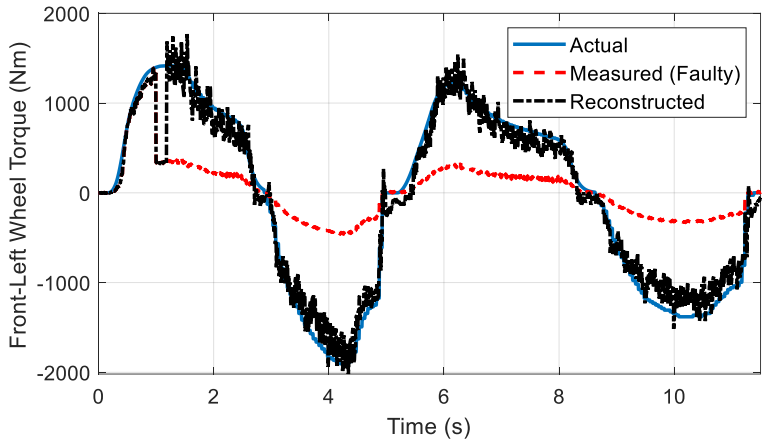

Figure 5.34. Reconstruction of the faulty front-left torque signal

The high frequency noise on the reconstructed signal is due to the unfiltered observer inputs (acceleration and wheel angular velocity signals). Filtering was avoided to prevent a phase shift in the reconstructed signal.

Experiment results for fault-tolerant estimation of the longitudinal tire forces is shown in Figure 5.35. Without fault tolerance, the front-left tire force estimator produces large errors due to the faulty input torque signal (NRMSE 38.25%). On the other hand, the proposed fault-tolerant estimation structure successfully estimates the front-left longitudinal force. The NRMSE for fault-tolerant estimation is 10.46%.

Since the other torque sensors are healthy, estimation results for the other tires are identical with and without fault tolerance. Estimation errors are 7.95% for the front-right tire, 4.54% for the rear-left tire and 5.64% for the rear-right tire.

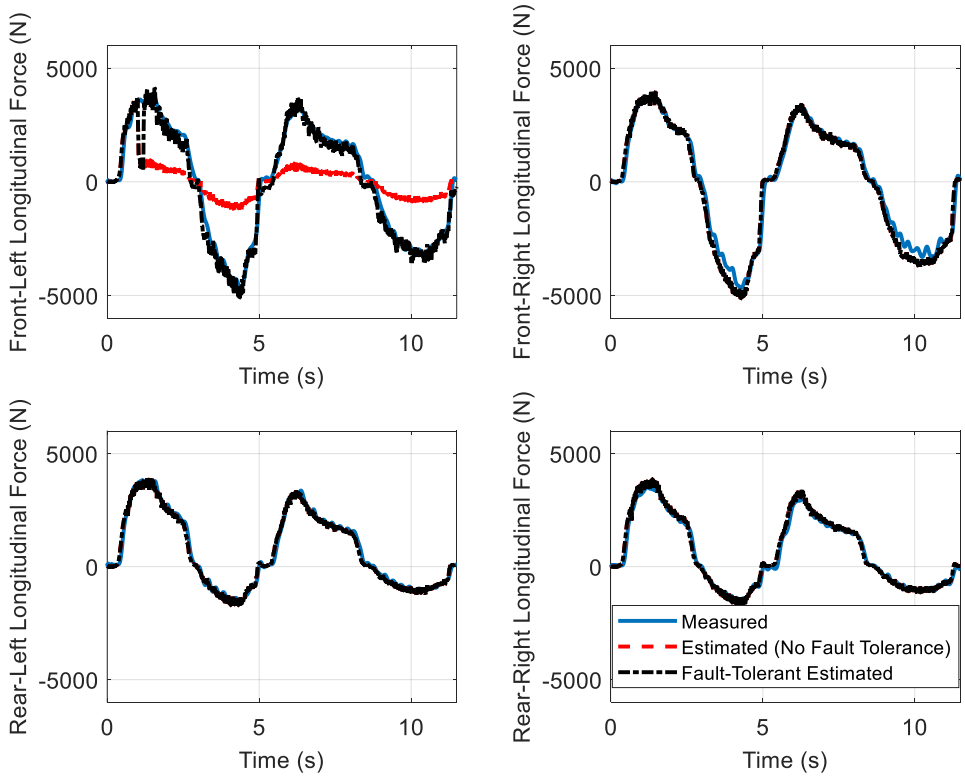

Figure 5.35. Fault-tolerant estimation of longitudinal tire forces when front-left torque sensor fails

5.8 Summary

This chapter presented a unified structure for fault-tolerant estimation of vehicle states including the longitudinal, lateral, and vertical tire forces, and longitudinal and lateral velocities. A set of disturbance observers were designed to detect the motor torque sensor faults and reconstruct the faulty signal. These observers delivered the fault-tolerant estimation of longitudinal tire forces. Fault-tolerant estimation of vertical tire forces was achieved by using the reconstructed signals and load transfer equations. For lateral tire forces, an adaptive UKF estimator was presented which receives the reconstructed inputs, adapts its measurement equation in response to faults, and delivers the fault-tolerant estimation of lateral forces for each tire. Fault-tolerant estimation of longitudinal and lateral velocities was achieved by using the kinematic observers which receive the reconstructed signals when a fault is present.

Moreover, this chapter combined the fault detection, signal reconstruction and fault-tolerant estimation modules that were developed in this thesis. The result is a unified structure that covers the full sensor set and delivers fault-tolerant estimation of the vehicle dynamic states.

Finally, several experimental case studies were conducted to verify the effectiveness of the proposed approach during different driving maneuvers. Various sensor failure scenarios were considered in these experiments including loss of signal, stuck-output, loss of sensitivity, etc. Desirable performance of the proposed structure in terms of reliable detection of sensor faults, precise reconstruction of the faulty signal and accurate/fault-tolerant estimation of the vehicle states was demonstrated through the experiment results.

Chapter 6
Conclusions and Future Work

6.1 Conclusions

This thesis presented a unified structure for detection of vehicle sensor faults, reconstruction of faulty sensory signals, and fault-tolerant estimation of vehicle states. The proposed structure can detect failures of the longitudinal, lateral and vertical acceleration sensors, roll rate, yaw rate and pitch rate sensors, steering angle sensor, suspension height sensors, and motor torque sensors.

To ensure a robust fault detection performance and avoid false positives, adaptive thresholds were integrated in the fault detection modules. The proposed method does not require prior knowledge of the sensor fault pattern and can detect various types of sensor faults including loss of signal, scaling, intermittency, bias, stuck-output, excessive noise, etc. Detectability and isolability of the faults using this approach were verified in this thesis. After detecting a fault, the proposed structure can reconstruct the faulty sensory signal and effectively arbitrate between the healthy and reconstructed signals.

Desirable performance of the proposed method in terms of timely detection of sensor faults and accurate reconstruction of the faulty signals was demonstrated through several experimental tests. The experiments covered various driving maneuvers, road conditions and sensor failure scenarios.

Additionally, the unified structure in this thesis can deliver fault-tolerant estimations of the vehicle states including the longitudinal, lateral and vertical tire forces, longitudinal and lateral velocities, roll angle, and pitch angle. Road grade and bank angles are also estimated in this method even in presence of sensor faults. The above objectives were achieved by using a common sensor set available in commercial vehicles. The proposed method did not presume availability of additional information such as prior knowledge of the road friction coefficient, road grade/bank angles, fault patterns, etc.

To detect and reconstruct failures of the roll rate, pitch rate and suspension height sensors, the proposed method combined a set of unknown input observers with the analytical redundancy relations derived from the roll, pitch and suspension dynamics. The interaction between the road angles and the vehicle states was considered in this design and the unknown road grade and bank disturbances were estimated in real-time. The outputs from the analytical redundancy relations and the unknown input observers generated unique residual patterns which were translated to unique fault signatures. Detectability and isolability of the faults were verified by using characteristics of the fault signature

matrix. After detecting a fault, reconstruction of the faulty sensory signal was accomplished by using the remaining healthy sensors and the estimated states from the observers. Several experimental case studies were presented to demonstrate the effectiveness of the proposed approach in various driving scenarios. Reliable and fast detection of faults, accurate reconstruction of the faulty signal and robustness against road disturbances were among the features of the proposed methodology.

To detect failures of the steering angle, yaw rate, and acceleration sensors, a set of virtual sensors were derived from the analytical redundancies and estimated vehicle states. The virtual sensors generated a sufficient set of residuals which guaranteed detectability and isolability of the faults. Reconstruction of the faulty signal was performed in a random walk observer with adaptive weights. These weights were designed to manage contribution of the virtual sensors in the reconstruction process, which enabled a reliable reconstruction performance in adverse driving conditions such as high wheel slips. Performance of this method was evaluated through experimental case studies during various driving maneuvers including step-steer, acceleration/braking, lane change, double-lane-change and slalom. These tests were performed on different road conditions. The experiment results verified the effectiveness of the proposed structure in terms of avoiding false positives, fast detection of sensor faults, and accurate reconstruction of the faulty signals.

Detection of motor torque sensor faults was accomplished by designing a set of disturbance observers combined with a residual processor logic. The faulty torque signal was reconstructed using the remaining healthy torque sensors and the estimated states from the observers. Experimental results verified that this method can reliably detect the fault, localize the faulty torque sensor and reconstruct its signal.

Fault-tolerant estimation of the vehicle states was another contribution of this thesis. The disturbance observers delivered the fault-tolerant estimation of longitudinal tire forces even in presence of a faulty torque sensor. Vertical tire forces were estimated by using the reconstructed acceleration signals, the estimated roll/pitch angles and the load transfer equations. For the lateral tire forces, an adaptive UKF estimator was presented which adapts its measurement equation when a sensor fails, and delivers the fault-free estimations for each tire. Fault-tolerant estimation of longitudinal and lateral velocities was achieved by using the kinematic observers which receive the reconstructed signals when a fault is present.

Several fault detections, signal reconstruction and fault-tolerant estimation modules were developed in this thesis. The unified structure which connected these modules was presented in Chapter 5. Subsequently, the unified structure was experimentally evaluated in several road tests. Performance of the estimators was studied in various sensor failure scenarios. The results showed that without fault tolerance, the estimation performance could significantly degrade when the faulty sensory signal is consumed by an estimator. On the other hand, the proposed fault-tolerant structure successfully detected the faults, reconstructed the faulty signals, and continued to provide reliable estimation results in all the attempted case studies.

The proposed method can be implemented on onboard vehicle electronic control units to ensure that vehicle control systems receive fault-free sensory measurements and fault-tolerant estimations of the vehicle states.

6.2 Future Work

The results of this thesis can be improved and extended to more applications. A few suggestions are mentioned in this section to continue this work:

- Real-time identification of vehicle parameters despite sensor faults: in this thesis, the nominal vehicle parameters were used to develop the proposed methods while the actual vehicle parameters might vary during the operation (e.g., vehicle mass and inertia variations due to the number of passengers, effective tire radius variations due to the tire pressure changes, etc.). To compensate for such parametric uncertainties, the static fault bounds were tuned conservatively to deliver larger fault thresholds and avoid false positives. Further extension of the concepts in this thesis can help identify the vehicle parameters during the operation, even in the presence of sensor faults. Availability of such real-time and robust parameters can help to lower the static fault thresholds, detect the sensor faults with smaller magnitudes, and improve the estimation performance.
- Higher fidelity vehicle models: throughout this thesis, several vehicle models were used which collectively cover the major states of vehicle dynamics. The lower-level vehicle dynamic states, such as tire camber angles and the precise kinematics of the steering system, were not incorporated due to their smaller effects. To compensate for such modeling uncertainties and avoid false positives during harsh excitations, dynamic fault thresholds with higher gains were

included in the residual processors. Incorporation of higher fidelity vehicle models into the proposed method can help lower the dynamic threshold gains, detect the smaller faults and achieve a more precise estimation performance.

- Higher fidelity estimation of vehicle lateral velocity: a simple kinematic model was used in this thesis for fault-tolerant estimation of lateral velocity. To compensate for the lower fidelity of the lateral velocity estimation, the rest of the estimators and fault detectors were designed to be less sensitive to, or independent of, the lateral velocity. More comprehensive methods for estimation of the lateral velocity can be integrated into the proposed structure to improve the performance.
- Integration with vehicle control systems: many advanced vehicle systems such as stability controllers and autonomous driving systems rely on information measured by the onboard sensors and the estimated vehicle states for their operation. The methods presented in this thesis can be integrated with vehicle control systems to detect the sensor faults, reconstruct the faulty signals, provide fault-tolerant estimation of the states, and enable a fault-tolerant control performance.
- Detection and mitigation of actuator faults: this thesis proposed methods for detection and mitigation of torque sensor and steering angle sensor faults. Similar methods can be developed to detect the actuator faults, localize the faulty actuator, and identify the actuator fault magnitude. Subsequently, fault-tolerant control strategies can be designed to reconfigure the control commands and effectively use the remaining healthy actuators to mitigate the fault and improve safety.
- Extension to the emerging sensors and autonomous driving applications: with the recent industry trend to offer higher levels of autonomy, more vehicles are being equipped with advanced sensors such as perception cameras, radars, LiDARs and high-precision GPS systems. Since information from these sensors is increasingly being used in safety-critical applications, effective mitigation of such sensor faults is a paramount objective. There is an opportunity to extend the methods presented in this thesis for detection of faults and reconstruction of faulty signals in the above sensors, which can help to ensure a more reliable operation of autonomous driving systems.

References

[1] Cho W, Choi J, Kim C, Choi S, Yi K. Unified Chassis Control for the Improvement of Agility, Maneuverability, and Lateral Stability. IEEE Transactions on Vehicular Technology 2012;61:1008–20.

[2] Li S, Li K, Rajamani R, Wang J. Model Predictive Multi-Objective Vehicular Adaptive Cruise Control. IEEE Transactions on Control Systems Technology 2011;19:556–66.

[3] Liu J, Jayakumar P, Stein JL, Ersal T. Combined Speed and Steering Control in High-Speed Autonomous Ground Vehicles for Obstacle Avoidance Using Model Predictive Control. IEEE Transactions on Vehicular Technology 2017;66:8746–63.

[4] Rajamani R, Piyabongkarn D. New Paradigms for the Integration of Yaw Stability and Rollover Prevention Functions in Vehicle Stability Control. IEEE Transactions on Intelligent Transportation Systems 2013;14:249–61.

[5] Xu L, Tseng HE. Robust Model-Based Fault Detection for a Roll Stability Control System. IEEE Transactions on Control Systems Technology 2007;15:519–28.

[6] Chamseddine A, Noura H. Control and Sensor Fault Tolerance of Vehicle Active Suspension. IEEE Transactions on Control Systems Technology 2008;16:416–33.

[7] Guvenc B, Guvenc L, Karaman S. Robust Yaw Stability Controller Design and Hardware-in-the-Loop Testing for a Road Vehicle. IEEE Transactions on Vehicular Technology 2009;58:555–71.

[8] Tjonnas J, Johansen TA. Stabilization of Automotive Vehicles Using Active Steering and Adaptive Brake Control Allocation. IEEE Transactions on Control Systems Technology 2010;18:545–58.

[9] Wu J, Wang Q, Wei X, Tang H. Studies on Improving Vehicle Handling and Lane Keeping Performance of Closed-Loop Driver-Vehicle System with Integrated Chassis Control. Mathematics and Computers in Simulation 2010;80:2297–308.

[10] Suh J, Chae H, Yi K. Stochastic Model-Predictive Control for Lane Change Decision of Automated Driving Vehicles. IEEE Transactions on Vehicular Technology 2018;67:4771–82.

[11] Ghike C, Shim T, Asgari J. Integrated Control of Wheel Drive-Brake Torque for Vehicle-Handling Enhancement. Proceedings of the Institution of Mechanical Engineers, Part D:

Journal of Automobile Engineering 2009;223:439–57.

[12] Cho W, Yoon J, Yim S. Estimation of Tire Forces for Application to Vehicle Stability Control. IEEE Transactions on Vehicular Technology 2010;59:638–49.

[13] Choi SB. Antilock Brake System With a Continuous Wheel Slip Control to Maximize the Braking Performance and the Ride Quality. IEEE Transactions on Control Systems Technology 2008;16:996–1003.

[14] Ghoneim YA, Lin WC, Chin Y-K, Sidlosky DM. Enhanced Traction Stability Control System. SAE Technical Paper 2005:2005-01–1591.

[15] Kim H, Lee H. Model-Based Fault-Tolerant Control for an Automotive Air Suspension Control System. Proceedings of the Institution of Mechanical Engineers, Part D: Journal of Automobile Engineering 2011;225:1462–80.

[16] Imine H, Benallegue A, Madani T, Srairi S. Rollover Risk Prediction of Heavy Vehicle Using High Order Sliding Mode Observer: Experimental Results. IEEE Transactions on Vehicular Technology 2014;63:2533–43.

[17] Pacejka HB. Tire and Vehicle Dynamics. 3rd ed. Butterworth-Heinemann; 2012.

[18] Fujimoto H, Hori Y. Lateral Stability Control of In-Wheel-Motor-Driven Electric Vehicles Based on Sideslip Angle Estimation Using Lateral Tire Force Sensors. IEEE Transactions on Vehicular Technology 2012;61:1972–85.

[19] Doumiati M, Victorino A, Lechner D, Baffet G, Charara A. Observers for Vehicle Tyre/Road Forces Estimation: Experimental Validation. Vehicle System Dynamics 2010;48:1345–78.

[20] Baffet G, Charara A, Lechner D, Thomas D. Experimental Evaluation of Observers for Tire-Road Forces, Sideslip Angle and Wheel Cornering Stiffness. Vehicle System Dynamics 2008;46:501–20.

[21] Doumiati M, Victorino AC, Charara A, Lechner D. Onboard Real-Time Estimation of Vehicle Lateral Tire–Road Forces and Sideslip Angle. IEEE/ASME Transactions on Mechatronics 2011;16:601–14.

[22] Jazar RN. Vehicle Dynamics: Theory and Application. Springer; 2008.

[23] Piyabongkarn D, Rajamani R, Grogg J a., Lew JY. Development and Experimental Evaluation

of a Slip Angle Estimator for Vehicle Stability Control. IEEE Transactions on Control Systems Technology 2009;17:78–88.

[24] Nam K, Oh S, Fujimoto H, Hori Y. Estimation of Sideslip and Roll Angles of Electric Vehicles Using Lateral Tire Force Sensors Through RLS and Kalman Filter Approaches. IEEE Transactions on Industrial Electronics 2013;60:988–1000.

[25] Park J-I, Yoon J-Y, Kim D-S, Yi K-S. Roll State Estimator for Rollover Mitigation Control. Proceedings of the Institution of Mechanical Engineers, Part D: Journal of Automobile Engineering 2008;222:1289–312.

[26] Oh J, Choi SB. Vehicle Roll and Pitch Angle Estimation Using a Cost-Effective Six-Dimensional Inertial Measurement Unit. Proceedings of the Institution of Mechanical Engineers, Part D: Journal of Automobile Engineering 2012;227:577–90.

[27] Dahmani H, Pagès O, El hajjaji A, Daraoui N. Observer-Based Robust Control of Vehicle Dynamics for Rollover Mitigation in Critical Situations. IEEE Transactions on Intelligent Transportation Systems 2013;15.

[28] Hashemi E, Khajepour A, Moshchuk N, Chen S-K. Real-Time Road Bank Estimation With Disturbance Observers for Vehicle Control Systems. IEEE Transactions on Control Systems Technology 2022;30:443–50.

[29] Patton RJ, Frank PM. Issues of Fault Diagnosis for Dynamic Systems. Springer; 2000.

[30] Guerrier S, Waegli A, Skaloud J, Victoria-Feser MP. Fault detection and isolation in multiple MEMS-IMUs configurations. IEEE Transactions on Aerospace and Electronic Systems 2012;48:2015–31.

[31] Isermann R. Fault-Diagnosis Applications: Model-Based Condition Monitoring: Actuators, Drives, Machinery, Plants, Sensors, and Fault-Tolerant Systems. Springer; 2011.

[32] Venkatasubramanian V, Rengaswamy R. A Review of Process Fault Detection and Diagnosis: Part I: Quantitative Model-Based Methods. Computers & Chemical Engineering 2003;27:293–311.

[33] Venkatasubramanian V. A Review of Process Fault Detection and Diagnosis: Part II: Qualitative Models and Search Strategies. Computers & Chemical Engineering 2003;27:313–

26.

[34] Venkatasubramanian V. A Review of Process Fault Detection and Diagnosis: Part III: Process History Based Methods. Computers & Chemical Engineering 2003;27:327–46.

[35] Ju Y, Tian X, Liu H, Ma L. Fault Detection of Networked Dynamical Systems: a Survey of Trends and Techniques. International Journal of Systems Science 2021;52:3390–409.

[36] Merzouki R, Samantaray AK, Pathak PM, Bouamama BO. Intelligent Mechatronic Systems: Modeling, Control and Diagnosis. vol. 2012. Springer Verlag; 2012.

[37] Rahim M a., Khalid HM, Akram M. Sensor Location Optimization for Fault Diagnosis with a Comparison to Linear Programming Approaches. International Journal of Advanced Manufacturing Technology 2012;65:1055–65.

[38] Magni J-F, Mouyon P. On residual Generation by Observer and Parity Space Approaches. IEEE Transactions on Automatic Control 1994;39:441–7.

[39] Isermann R. Fault-Diagnosis Systems: An Introduction From Fault Detection to Fault Tolerance. Springer Berlin Heidelberg; 2006.

[40] Jiang Y, Yin S, Kaynak O. Optimized Design of Parity Relation-Based Residual Generator for Fault Detection: Data-Driven Approaches. IEEE Transactions on Industrial Informatics 2021;17:1449–58.

[41] Lee J, Park CG. Cascade Filter Structure for Sensor/Actuator Fault Detection and Isolation of Satellite Attitude Control System. International Journal of Control, Automation and Systems 2012;10:506–16.

[42] Veluvolu KC, Defoort M, Soh YC. High-Gain Observer with Sliding Mode for Nonlinear State Estimation and Fault Reconstruction. Journal of the Franklin Institute 2013:1–20.

[43] Wei X, Liu L, Jia L. Fault Diagnosis for High Order Systems Based on Model Decomposition. International Journal of Control, Automation and Systems 2013;11:75–83.

[44] Zarringhalam R, Rezaeian A, Khajepour A, Melek W. Vehicle Sensor Failure Detection and Fault-Tolerant Estimation of States. Symposium on Advanced Intelligent Systems, 2012.

[45] Heredia G, Caballero F, Maza I, Merino L, Viguria A, Ollero A. Multi-Unmanned Aerial Vehicle (UAV) Cooperative Fault Detection Employing Differential Global Positioning

(DGPS), Inertial and Vision Sensors. Sensors (Basel, Switzerland) 2009;9:7566–79.

[46] Hwang I, Kim S, Kim Y, Seah CE. A Survey of Fault Detection, Isolation, and Reconfiguration Methods. IEEE Transactions on Control Systems Technology 2010;18:636–53.

[47] Mehra RK, Peschon J. An Innovations Approach to Fault Detection and Diagnosis in Dynamic Systems. Automatica 1971;7:637–40.

[48] Liu Y, Li S, Fu Q, Liu Z, Zhou Q. Analysis of Kalman Filter Innovation-Based GNSS Spoofing Detection Method for INS/GNSS Integrated Navigation System. IEEE Sensors Journal 2019;19:5167–78.

[49] Yang Q, Li S, Cao Y. A Strong Tracking Filter Based Multiple Model Approach for Gas Turbine Fault Diagnosis. Journal of Mechanical Science and Technology 2018;32:465–79.

[50] Bae J, Kim Y. Attitude Estimation for Satellite Fault Tolerant System Using Federated Unscented Kalman Filter. International Journal of Aeronautical and Space Sciences 2010;11:80–6.

[51] Hajiyev C, Soken HE. Robust Adaptive Unscented Kalman Filter for Attitude Estimation of Pico Satellites. International Journal of Adaptive Control and Signal Processing 2013.

[52] Balaban E, Saxena A, Bansal P, Goebel KF, Curran S. Modeling, Detection, and Disambiguation of Sensor Faults for Aerospace Applications. IEEE Sensors Journal 2009;9:1907–17.

[53] Zarringhalam R, Rezaeian A, Fallah S, Khajepour A, Melek W, Chen S-K, et al. Optimal Sensor Configuration and Fault-Tolerant Estimation of Vehicle States. SAE International Journal of Passenger Cars - Electronic and Electrical Systems 2013;6:83–92.

[54] Ding SX. Model-Based Fault Diagnosis Techniques. Springer London; 2013.

[55] Zhang X, Polycarpou MM, Parisini T. Fault Diagnosis of a Class of Nonlinear Uncertain Systems with Lipschitz Nonlinearities Using Adaptive Estimation. Automatica 2010;46:290–9.

[56] Arogeti S, Wang D. Fault Detection Isolation and Estimation in a Vehicle Steering System. Industrial Electronics on Industrial Electronics 2012;59:4810–20.

[57] Feng D, Wang J, Huang D. Hand-wheel Steering Signal Estimation and Diagnosis Approaches for Ground Vehicles. Control Engineering Practice 2012;20:654–62.

[58] Lee H. Analysis of Model-Based Sensor Fault Diagnosis with Application to a Motor-Driven Power Steering System. Proceedings of the Institution of Mechanical Engineers, Part D: Journal of Automobile Engineering 2011;225:1317–33.

[59] Anwar S, Chen L. An Analytical Redundancy-Based Fault Detection and Isolation Algorithm for a Road-Wheel Control Subsystem in a Steer-By-Wire System. IEEE Transactions on Vehicular Technology 2007;56:2859–69.

[60] Kim J, Lee H. Sensor Fault Detection and Isolation Algorithm for a Continuous Damping Control System. Proceedings of the Institution of Mechanical Engineers, Part D: Journal of Automobile Engineering 2011;225:1347–64.

[61] Metallidis P, Verros G, Natsiavas S, Papadimitriou C. Fault Detection and Optimal Sensor Location in Vehicle Suspensions. Journal of Vibration and Control 2003;9:337–59.

[62] Yan S, Sun W, Yu X, Gao H. Adaptive Sensor Fault Accommodation for Vehicle Active Suspensions via Partial Measurement Information. IEEE Transactions on Cybernetics 2021:1–12.

[63] Tabbache B, Benbouzid M, Kheloui A, Bourgeot J-M. DSP-Based Sensor Fault Detection and Post Fault-Tolerant Control of an Induction Motor-Based Electric Vehicle. International Journal of Vehicular Technology 2012;2012:1–7.

[64] Zhang C, Huang Y, Shao R. Robust Sensor Faults Detection for Induction Motor Using Observer. Journal of Control Theory and Applications 2012;10:528–32.

[65] Kim S, Song B, Song H. Integrated Fault Detection and Diagnosis System for Longitudinal Control of an Autonomous All-Terrain Vehicle (ATV). International Journal of Automotive Technology 2009;10:505–12.

[66] Hwang W, Han K, Huh K. Fault Detection and Diagnosis of the Electro-Mechanical Brake Based on Observer and Parity Space. International Journal of Automotive Technology 2012;13:845–51.

[67] Kim MH, Lee S, Lee KC. Kalman Predictive Redundancy System for Fault Tolerance of

Safety-Critical Systems. IEEE Transactions on Industrial Informatics 2010;6:46–53.

[68] Sankavaram C, Pattipati B, Pattipati K, Howell M, Salman M. Data-Driven Fault Diagnosis in A Hybrid Electric Vehicle Regenerative Braking System. 2012 IEEE Aerospace Conference, IEEE; 2012, p. 1–11.

[69] Zhang L, Wang Z, Ding X, Li S, Wang Z. Fault-Tolerant Control for Intelligent Electrified Vehicles Against Front Wheel Steering Angle Sensor Faults During Trajectory Tracking. IEEE Access 2021;9:65174–86.

[70] Fischer D, Börner M, Schmitt J, Isermann R. Fault Detection for Lateral and Vertical Vehicle Dynamics. Control Engineering Practice 2007;15:315–24.

[71] Arndt M, Ding EL, Massel T. Observer Based Diagnosis of Roll Rate Sensor. Proceedings of the 2004 American Control Conference, vol. 2, 2004.

[72] Jeppesen BP, Cebon D. Analytical Redundancy Techniques for Fault Detection in an Active Heavy Vehicle Suspension. Vehicle System Dynamics 2004;42:75–88.

[73] Jeppesen BP, Cebon D. Application of Observer-Based Fault Detection in Vehicle Roll Control. Vehicle System Dynamics 2009;47:465–95.

[74] Ha D, Kim H, Lee H. Height Sensor Fault Diagnosis for Electronic Air Suspension (EAS) System. IEEE International Symposium on Industrial Electronics, 2009, p. 211–6.

[75] Bouibed K, Aitouche A, Bayart M. Nonlinear Parity Space Applied to an Electric Autonomous Vehicle. 2009 International Conference on Mechatronics and Automation, IEEE; 2009, p. 198–203.

[76] Bouibed K, Aitouche A, Bayart M. Sensor and Actuator Fault Detection and Isolation Using Two Model Based Approaches: Application to an Autonomous Electric Vehicle. 18th Mediterranean Conference on Control and Automation, MED'10, vol. 33, IEEE; 2010, p. 1290–5.

[77] Bouibed K, Aitouche A, Bayart M. Sensor Fault Detection by Sliding Mode Observer Applied to an Autonomous Vehicle. 2009 International Conference on Advances in Computational Tools for Engineering Applications, IEEE; 2009, p. 621–6.

[78] Hok KN, Chen RH, Speyer JL. A Vehicle Health Monitoring System Evaluated

Experimentally on a Passenger Vehicle. IEEE Transactions on Control Systems Technology 2006;14:854–70.

[79] Rezaeian A, Zarringhalam R, Fallah S, Melek W, Khajepour A, Chen S-K, et al. Cascaded Dual Extended Kalman Filter for Combined Vehicle State Estimation and Parameter Identification. SAE 2013 World Congress & Exhibition, 2013.

[80] Wilkin M a., Manning WJ, Crolla D a., Levesley MC. Use of an Extended Kalman Filter as a Robust Tyre Force Estimator. Vehicle System Dynamics 2006;44:50–9.

[81] Liao Y-W, Borrelli F. An Adaptive Approach to Real-Time Estimation of Vehicle Sideslip, Road Bank Angles, and Sensor Bias. IEEE Transactions on Vehicular Technology 2019;68:7443–54.

[82] Wang Y, Xu L, Zhang F, Dong H, Liu Y, Yin G. An Adaptive Fault-Tolerant EKF for Vehicle State Estimation With Partial Missing Measurements. IEEE/ASME Transactions on Mechatronics 2021;26:1318–27.

[83] Rehm A. Centralized Monitoring for Vehicle Dynamics Sensor Networks. Proceedings of the 17th World Congress The International Federation of Automatic Control, 2008, p. 14987–91.

[84] Ding SX, Schneider S, Ding EL, Rehm A. Fault Tolerant Monitoring of Vehicle Lateral Dynamics Stabilization Systems. Proceedings of the 44th IEEE Conference on Decision and Control, vol. 4, IEEE; 2005, p. 2000–5.

[85] Unger I, Isermann R. Fault Tolerant Sensors for Vehicle Dynamics Control. 2006 American Control Conference, IEEE; 2006, p. 3948–53.

[86] Fekih A, Seelem S. A Fault Tolerant Control Design for Automatic Steering Control of Ground Vehicles. 2012 IEEE International Conference on Control Applications (CCA), 2012, p. 1491–6.

[87] Hashemi E, Zarringhalam R, Khajepour A, Melek W, Kasaiezadeh A, Chen SK. Real-Time Estimation of the Road Bank and Grade Angles with Unknown Input Observers. Vehicle System Dynamics 2017;55.

[88] Franklin GF, Powell JD, Workman ML. Digital Control of Dynamic Systems. 3rd ed. Addison Wesley Longman; 1998.

[89] Sundaram S, Hadjicostis CN. Partial State Observers for Linear Systems with Unknown Inputs. Automatica 2008;44:3126–32.

[90] Sundaram S, Hadjicostis CN. Delayed Observers for Linear Systems With Unknown Inputs. IEEE Transactions on Automatic Control 2007;52:334–9.

[91] Imsland L, Johansen TA, Fossen TI, Kalkkuhl JC, Suissa A. Vehicle Velocity Estimation using Modular Nonlinear Observers. Proceedings of the 44th IEEE Conference on Decision and Control, IEEE; 2005, p. 6728–33.

[92] ISO (International Organization for Standardization). Road vehicles - Vehicle Dynamics and Road-Holding Ability - Vocabulary. ISO 8855; 2011.

[93] Pisu P, Soliman A, Rizzoni G. Vehicle Chassis Monitoring System. Control Engineering Practice 2003;11:345–54.

[94] Varga A. Solving Fault Diagnosis Problems, Linear System Techniques. Berlin: Springer; 2017.

[95] Zarringhalam R, Rezaeian A, Melek W, Khajepour A, Chen S, Moshchuk N. A Comparative Study on Identification of Vehicle Inertial Parameters. 2012 American Control Conference (ACC), 2012, p. 3599–604.

[96] Rezaeian A, Zarringhalam R, Fallah S, Melek W, Khajepour A. Joint Unscented Kalman Filter for Combined Estimation of Vehicle States and Parameters. 11th International Symposium on Advanced Vehicle Control (AVEC ’12) 2012.

[97] Rezaeian A, Zarringhalam R, Fallah S, Melek W, Khajepour A, Chen S-K, et al. Novel Tire Force Estimation Strategy for Real-Time Implementation on Vehicle Applications. IEEE Transactions on Vehicular Technology 2015;64:2231–41.

[98] Kiencke U, Nielsen L. Automotive Control Systems: for Engine, Driveline, and Vehicle. Springer Berlin Heidelberg; 2005.

[99] Imsland L, Johansen TA, Fossen TI, Fjær Grip H, Kalkkuhl JC, Suissa A. Vehicle Velocity Estimation Using Nonlinear Observers. Automatica 2006;42:2091–103.

[100] Simon D. Optimal State Estimation: Kalman, H∞, and Nonlinear Approaches. Wiley-Interscience; 2006.

[101] Rajamani R. Vehicle Dynamics and Control. Springer US; 2012.

[102] Ding X, Wang Z, Zhang L, Liu J. A Comprehensive Vehicle Stability Assessment System Based on Enabling Tire Force Estimation. IEEE Transactions on Vehicular Technology 2022:1–17.

[103] Julier S, Uhlmann J, Durrant-Whyte HF. A New Method for the Nonlinear Transformation of Means and Covariances in Filters and Estimators. IEEE Transactions on Automatic Control 2000;45:477–82.

[104] Han J, Song Q, He Y. Adaptive Unscented Kalman Filter and Its Applications in Nonlinear Control. Kalman Filter Recent Advances and Applications, InTech; 2009, p. 1–25.

[105] Partovibakhsh M, Liu G. An Adaptive Unscented Kalman Filtering Approach for Online Estimation of Model Parameters and State-of-Charge of Lithium-Ion Batteries for Autonomous Mobile Robots. IEEE Transactions on Control Systems Technology 2014;23:1–1.

[106] Rezaeian A, Khajepour A, Melek W, Chen S-K, Moshchuk N. Simultaneous Vehicle Real-Time Longitudinal and Lateral Velocity Estimation. IEEE Transactions on Vehicular Technology 2017;66:1950–62.

[107] Merwe R Van Der. Sigma-Point Kalman Filters for Probabilistic Inference in Dynamic State-Space Models. PhD Thesis, Oregon Health and Science University, 2004.

Appendix A
UKF Estimation Approach

For a nonlinear system expressed in the state-space form as:

$$X_{k+1} = f\left(X_{k,}U_k\right) + w_k \tag{A-1}$$

$$Y_k = h(X_k\,) + v_k \tag{A-2}$$

the UKF algorithm can estimate the states as follows:

Initialization:

$$\bar{X}_0 = \mathrm{E}[X_0] \tag{A-3}$$

$$\mathcal{P}_0 = \mathrm{E}[(X_0 - \bar{X}_0)(X_0 - \bar{X}_0)^T] \tag{A-4}$$

where $\bar{X}_0$ is the initial state, $\mathcal{P}_0$ is the initial covariance and E is the expected value.

Calculation and propagation of sigma points:

$$\mathcal{X}_{i,k-1} = \left[\bar{X}_{0,k-1}, \bar{X}_{k-1} \pm \sqrt{(n+\lambda)\mathcal{P}_{k-1}}\right], \quad i = 0,1,\ldots,2n \tag{A-5}$$

$$\lambda = n(\alpha^2 - 1) + \alpha^2\epsilon \tag{A-6}$$

where $\mathcal{X}_{i,k-1}$ is the sigma point, $\bar{X}_{k-1}$ is the estimated state, $\mathcal{P}_{k-1}$ is the state covariance, n is the number of states and $i = 0,1,\ldots,2n$ indicates the $2n+1$ sigma points. The constants α and ϵ manage distribution of the sigma points around the mean value of the states.

Time update:

$$\mathcal{X}^*_{i,k|k-1} = f\left(\mathcal{X}_{i,k-1}, U_{k-1}\right) \tag{A-6}$$

$$\bar{X}_{k|k-1} = \sum_{i=0}^{2n} w_i^{(m)}\, \mathcal{X}^*_{i,k|k-1} \tag{A-7}$$

$$\mathcal{P}_{k|k-1} = \sum_{i=0}^{2n} w_i^{(c)} \left(\mathcal{X}^*_{i,k|k-1} - \bar{X}_{k|k-1}\right) \times \left(\mathcal{X}^*_{i,k|k-1} - \bar{X}_{k|k-1}\right)^T + \mathcal{Q} \tag{A-9}$$

$$\mathcal{X}_{i,k|k-1} = [\bar{X}_{k-1}, \bar{X}_{k-1} \pm \sqrt{(n+\lambda)\mathcal{P}_{k-1}}] \tag{A-10}$$

$$\gamma_{i,k|k-1} = h(\mathcal{X}_{i,k|k-1}) \tag{A-11}$$

$$\bar{Y}_{k|k-1} = \sum_{i=0}^{2n} w_i^{(m)}\, \gamma_{i,k|k-1} \tag{A-12}$$

where $w^{(m)}$ and $w^{(c)}$ are scaler weights for the mean and covariance of the sigma points, respectively, $\gamma_{i,k|k-1}$ is the predicted measurement, $\bar{Y}_{k|k-1}$ is the predicted output and Q is the process noise covariance. The weights are defined as:

$$w_0^{(m)} = \frac{\lambda}{n+\lambda} \tag{A-13}$$

$$w_0^{(c)} = \frac{\lambda}{n+\lambda} + (n - \alpha^2 + \beta) \tag{A-14}$$

$$w_i^{(m)} = w_i^{(c)} = \frac{1}{2(n+\lambda)} \tag{A-15}$$

where β is a constant to incorporate prior knowledge of the distribution of X.

Measurement update:

$$\mathcal{P}_{\bar{Y}_k\bar{Y}_k} = \sum_{i=0}^{2n} w_i^{(c)}\left(\gamma_{i,k|k-1} - \bar{Y}_{k|k-1}\right) \times \left(\gamma_{i,k|k-1} - \bar{Y}_{k|k-1}\right)^T + \mathcal{R} \tag{A-16}$$

$$\mathcal{P}_{\bar{X}_k\bar{Y}_k} = \sum_{i=0}^{2n} w_i^{(c)}\left(\mathcal{X}_{i,k|k-1} - \bar{X}_{k|k-1}\right) \times \left(\gamma_{i,k|k-1} - \bar{Y}_{k|k-1}\right)^T \tag{A-17}$$

$$\mathcal{K}_k = \mathcal{P}_{\bar{X}_k\bar{Y}_k}\mathcal{P}_{\bar{Y}_k\bar{Y}_k}^{-1} \tag{A-18}$$

$$\mathcal{P}_k = \mathcal{P}_{k|k-1} - \mathcal{K}_K\mathcal{P}_{\bar{Y}_k\bar{Y}_k}\mathcal{K}_k^T \tag{A-19}$$

$$\bar{X}_k = \bar{X}_{k|k-1} + \mathcal{K}_k(Y_k - \bar{Y}_{k|k-1}) \tag{A-20}$$

where $\mathcal{P}_{\bar{Y}_k\bar{Y}_k}$ is the innovation covariance, $\mathcal{P}_{\bar{X}_k\bar{Y}_k}$ is the cross covariance, $\mathcal{R}$ is the measurement noise covariance and $\mathcal{K}_k$is the filter gain.